Contents

List of Tables

List of Figures

Chapter 1

Introduction

1.1 Microfluidics and the Lab-on-a-Chip

Microfluidics deals with the behaviour, control and manipulation of fluids that are geometrically constrained to the submillimeter scale (Stone *et al.* (2004); Squires & Quake (2005)). The physics of fluids at this scale has been long of interest in colloids and life sciences. Currently, *Microfluidics* is a broader term that also includes all the technological research focused on the microfabrication techniques of *microfluidic circuits*, as part of a more general engineering field known as MEMS -microelectromechanical systems- (Malouf (2004); Hardt & Schönfeld (2008)). The development of techniques for fluid flow visualization at the microscale (Sinton (2004); Adrian (2005)) is also of current interest in the microfluidics research.

The reason for a fast increasing interest in this field is twofold: First, fabrication techniques developed by the microelectronics industry allow accurate design of microfluidic circuits. Secondly, advances in biology and biotechnology require manipulation of particles or living cells. Miniaturization of analytical processes in chemistry has also the advantage of low sample and reagent consumption. "Lab-on-a-chip" systems are the technological goal of the microfluidics research (Dittrich *et al.* (2006); Whitesides *et al.* (2006)). Despite the terms *Lab-on-a-chip* and *micro-Total Analysis Systems* (μTAS) are commonly used with the same meaning, the former generally indicates the scaling of single or multiple lab processes down to chip-format, whereas "μTAS" is dedicated to the integration of the total sequence of lab processes to perform chemical analysis. In any case, shrinking the lab is an appealing idea to engineers, chemists and biologists and, consequently, it is generating a growing interest in the study of the "physics of fluids at the microscale".

The dynamics of fluid flows generated by electric fields is the subject of Electrohydrodynamics (EHD). Electrodes integrated in microchannels represent an opportunity for actuation either on the liquid or suspended particles. Therefore, EHD in microsystems is of central interest in microfluidics research. In particular, arrays of microelectrodes subjected to AC potentials are used for pumping small amounts of liquid within the microchannels (see section 1.3). Here lies the motivation of the present PhD thesis: *Arrays of coplanar microelectrodes (typical width tens of microns) are a subject of current research for pumping purposes.* Experiments have proved the ability of such arrays to effectively pump electrolytes within microchannels. However, experimental observations show greater complexity than the behaviour predicted by the theoretical models.

Two kind of electrodes structures are considered: *arrays of asymmetric pairs of electrodes* subjected to an AC potential and *arrays of equal sized electrodes subjected to a travelling-wave potential.* The basic ideas behind them are shown in section 1.3. Despite the motivation for these electrode designs is their capability for generating net pumping within microchannels, the experimental observations rise new questions on the EHD of microsystems. We consider that the results of this work open some room for further research in the understanding of the *interaction of electric fields and electrolytes at the micrometer scale.*

1.2 AC electrokinetics in microsystems

In order to understand how to manipulate fluids and colloidal particles within microsystems, it is important to determine the scale and range of forces that govern the behaviour under different experimental conditions (Ramos *et al.* (1998); Castellanos *et al.* (2003)). In particular, the experimental methodology used in this work relies on the use of fluorescent latex particles (500 nm dia.) for the characterization of fluid flows. The fluid is seeded with the fluorescent beads and, using a suitable fluorescence microscopy set, the particle motion is tracked. In this section we analyze the dynamics of the particles, including a brief survey of forces that can act on particles and fluids after application of AC signals.

Let us consider a spherical particle suspended in the fluid. Assuming that the viscous drag on the particle is given by Stokes' law, the motion of the particle subjected to a force **F** is governed by:

$$m\frac{d\mathbf{u}}{dt} = -\gamma(\mathbf{u} - \mathbf{v}) + \mathbf{F} \tag{1.1}$$

where m is the particle mass, **u** the particle velocity, **v** the fluid velocity and γ the friction factor of the particle in the fluid ($\gamma = 6\pi\eta a$ for a spherical particle of radius a in a fluid of viscosity η). If the force F and fluid velocity are constant, the particle velocity is

$$\mathbf{u} = \left(\mathbf{u}_0 - \mathbf{v} - \frac{\mathbf{F}}{\gamma}\right) e^{-(\gamma/m)t} + \mathbf{v} + \frac{\mathbf{F}}{\gamma} \tag{1.2}$$

where $\mathbf{u}_0$ is the initial velocity of the particle. The characteristic time of acceleration, $\tau_a = m/\gamma$, for a spherical particle of mass density ρ_p is $\tau_a = (2/9)(\rho_p a^2/\eta)$. For submicrometre particles, τ_a is smaller than 10^{-6} s, while typical observations times are of 1 s. Therefore, the particle can be considered to move at its terminal velocity:

$$\mathbf{u} = \mathbf{v} + \frac{\mathbf{F}}{\gamma} \tag{1.3}$$

The real acceleration process may be more complicated than that described by eq. 1.2 (due to the surrounding liquid inertia). However, the result that particles have reached their terminal velocity at times much larger than τ_a is still valid. This result means that any measurement of particle velocity is a direct measure of the fluid velocity, $\mathbf{v}$, plus the velocity induced by the force acting on the particle, $\mathbf{F}/\gamma$.

It should be noted that Brownian motion was not considered in the particle dynamics. That would introduce in eq. 1.1 a random force field representing the effect of the thermal fluctuations of the fluid (Langevin equation). Despite the force and velocity due to Brownian motion have zero time-average, the random displacement of the particle follows a Gaussian profile with a root-mean-square displacement (in one dimension) given by:

$$\Delta x = \sqrt{2Dt} = \sqrt{\frac{k_B T}{3\pi a \eta} t} \tag{1.4}$$

For the case of a 500 nm diameter particle in water at $T \sim 20\,^{\circ}\mathrm{C}$ (as the beads used in this work), the root-mean-square displacement after 1 s is only $1\,\mu$m. This means that if we are measuring velocities around $10\,\mu\mathrm{m}/s$ and above (as typically occurs in our experiments), Brownian motion can be neglected in the particle motion.

1.2.1 Dielectrophoretic force

Particles in electric fields may undergo electrophoretic and dielectrophoretic motion. The electrophoretic motion in AC electric fields is oscillatory, with a maximum amplitude given by $\Delta x = u/\omega$, where ω is the angular frequency of the applied field and u the electrophoretic velocity (which can be estimated from the Smoluchowski formula). The amplitude of the electrophoretic motion decreases with frequency and may be neglected for sufficiently high frequencies (Castellanos *et al.* (2003)). For example, for a field amplitude of 10^5 V/m, a frequency of 1 kHz and a zeta potential of 50 mV, the displacement is $\Delta x \sim 0.5\,\mu$m.

In the case of nonuniform AC fields, particles are subjected to a net force as a consequence of the electric field acting on the induced dipole. This phenomenon is known as *Dielectrophoresis* (DEP, Pohl (1978)) and it is of utmost interest in current 'Lab-on-a-chip' research (Morgan &

Green (2003)).

Due to the difference in electrical properties between the particle and surrounding fluid, the action of the electric field induces a net dipolar moment. The net force on the particle is then given by $\mathbf{F}_{DEP} = \mathbf{p} \cdot \nabla \mathbf{E}$. The induced dipolar moment phasor of a particle with volume v can be written as $\tilde{\mathbf{p}}(\omega) = v\alpha(\omega)\tilde{\mathbf{E}}$, where α is the effective polarizability of the particle, ω is the angular frequency of the electric field and $\tilde{\mathbf{E}}$ is the electric phasor. The time-averaged force on the particle is given by (Green *et al.* (2000c)):

$$\mathbf{F}_{DEP} = \frac{1}{2}\mathrm{Re}[\mathbf{p} \cdot \nabla \tilde{\mathbf{E}}^*] = \\ = \frac{1}{4}v\mathrm{Re}[\alpha]\nabla|\tilde{\mathbf{E}}|^2 - \frac{1}{2}v\mathrm{Im}[\alpha](\nabla \times (\mathrm{Re}[\tilde{\mathbf{E}}] \times \mathrm{Im}[\tilde{\mathbf{E}}])) \quad (1.5)$$

The first term on the right-hand side of (1.5) is non-zero if there is a spatially varying field magnitude. The second term is non-zero if there is a spatially varying phase, as in the case of travelling-wave dielectrophoresis (twDEP)(Green *et al.* (2002b); Wang *et al.* (1994); Huang *et al.* (1993)).

For dielectrophoresis alone (only spatially varying field magnitude) and if we consider that the interfacial polarization of the particle is only due to the Maxwell-Wagner mechanism (Morgan & Green (2003)), the dielectrophoretic velocity of a particle with radius a is given by:

$$u_{DEP} = \frac{a^2\varepsilon}{2\eta}\mathrm{Re}\left[\frac{\tilde{\varepsilon}_p - \tilde{\varepsilon}}{\tilde{\varepsilon}_p + 2\tilde{\varepsilon}}\right]\nabla|\tilde{\mathbf{E}}|^2 \quad (1.6)$$

where $\tilde{\varepsilon}_p$ and $\tilde{\varepsilon}$ are the particle and medium complex permitivitty, respectively. The factor between brackets is known as the *Clausius-Mosotti* factor. The real part of this factor varies between +1 and -1/2, depending on the frequency. When the particle moves towards a region of higher field strength it is said to undergo *positive DEP*. Conversely, if it moves to a region of lower field strength, it undergoes *negative DEP*.

An analytical expression was derived in Morgan *et al.* (2001) for the dielectrophoretic force on a particle subjected to a four phase travelling-wave potential. The expression is valid at heights over the electrodes greater than the electrodes width (d). We include it here because it will be of interest when discussing the experiments on travelling-wave electroosmosis. Since we use fluorescent latex beads as fluid flow tracers, we should consider the possibility that this force is also acting on the particles. The time-averaged force components are:

$$< \mathbf{F}_x(t) >= -0.373\frac{vV_0{}^2}{d^3}\mathrm{Im}[\alpha]e^{-(\pi/2d)y} \tag{1.7}$$

$$< \mathbf{F}_y(t) >= -0.373\frac{vV_0{}^2}{d^3}\mathrm{Re}[\alpha]e^{-(\pi/2d)y} \tag{1.8}$$

where V_0 is the amplitude of the sinusoidal potentials applied at each electrode. The expression is valid at $y > 1.5d$ and in the absence of electrode polarization.

1.2.2 AC Electroosmosis

It has been demonstrated in several works that fluid motion can be generated over microelectrode structures by the influence of an AC field on the induced charge in the electrical double layer (Yeh *et al.* (1997); Green *et al.* (2000a); Ramos *et al.* (1998, 1999b)). This fluid motion has been termed *AC Electroosmosis* (ACEO) because of the analogy with the electroosmotic streaming at solid-liquid interfaces. Generation of fluid flow when an applied field acts on its own induced diffuse charge has been observed in many other situations (they have recently been reviewed in Squires & Bazant (2004)). The term "induced-charge electroosmosis" (ICEO) was suggested in Bazant *et al.* (2004) to include all these phenomena.

The simplest system for the study of AC electroosmosis is a couple of coplanar electrodes subjected to a harmonic potential difference of amplitude V_0 and frequency ω, i.e. $V = V_0 \cos(\omega t)$. Fig. 1.1 shows a sketch of the physical system at a given time of the AC signal cycle. The applied field attracts counterions at the solid-liquid interfaces and, since the electric field is non-uniform, there appears an electrical force $\mathbf{F} = q\mathbf{E}_t$ pulling the liquid outwards ($\mathbf{E}_t$ is the component of the electric field tangential to the electrode surfaces). Note that in the other half-cycle the tangential field and the induced charge change sign and, therefore, the force direction remains the same and the time-averaged force is nonzero.

The generated velocity by this mechanism is frequency dependent. At low frequencies the electrical charges have sufficient time to completely screen the electric field at the electrodes, the electric field in the electrolyte bulk vanishes and so does the induced velocity. In this view,

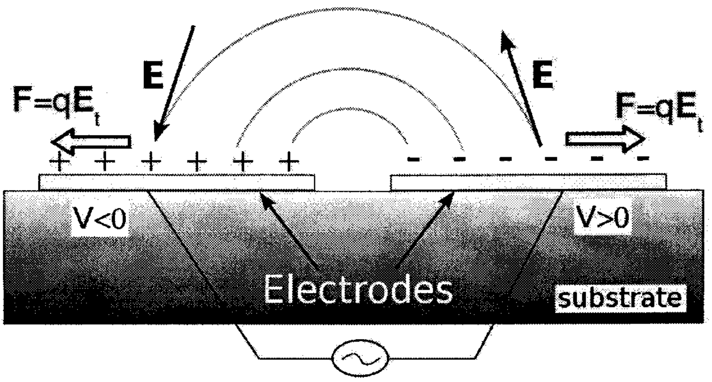

Figure 1.1: Basics of the ACEO mechanism. Electrical charge is induced at the electrode/electrolyte interface. The tangential component of the electric field acts on this charge giving rise to a surface fluid velocity.

the electrodes are supposed to be perfectly polarizable, i.e. no Faradaic currents occur. At high frequencies, the electrical charges have no time to follow the electric field, the induced charge at the electrodes tends to zero and, therefore, the electrical force is negligible. The theoretical expectation for the velocity versus frequency plot is a bell-shaped curve, in accordance with the experimental observations in Green *et al.* (2000a).

As mentioned above, counterions are attracted at the solid-liquid interfaces and net charge is induced in the electrical double layer. The typical distance in the system within net charge is induced corresponds with the Debye length, λ_D (Hunter (1993)). For typical conductivities in experiments, this length is of the order of 10 nm, much smaller than any other distance in the system and, therefore, the *thin double layer approximation* can be used (González *et al.* (2000)). This allows us to distinguish two typical length scales: one is the Debye length (where net electrical charge is induced) and the other is the typical system size corresponding to the characteristic dimension of the electrodes and the variations of the electric field. The electrolyte remains electroneutral at the length scale of the electrode dimensions. Thus, the electric potential obeys Laplace's equation in the bulk $\nabla^2\phi = 0$. For low voltages and frequencies much lower than the relaxation frequency of the liquid ($\omega << \sigma/\varepsilon$, as correspond with the typical frequency in ACEO experiments), the electrical double layer can be supposed to be in quasiequilibrium. In this case, and for perfectly polarizable electrodes, the charging of the electrical double layer can be modelled by means of a surface capacitance (Ramos *et al.* (1999a)). The charging of the capacitor through the current from the bulk yields the following boundary condition for the electric potential at the electrode surface:

$$-\mathbf{n} \cdot \nabla \Phi = \frac{i\omega C_{DL}}{\sigma}(V_0 - \Phi) \tag{1.9}$$

where $\mathbf{n}$ is a vector normal to the electrode surface, σ is the liquid conductivity, Φ is the electric potential phasor, C_{DL} is the double layer capacitance and V_0 is the potential amplitude applied to the electrode. The electroosmotic slip velocity generated on the electrodes is given by the Helmholtz-Smoluchowski formula $u_{slip} = (\varepsilon/\eta)\zeta E_t$, where ζ is the induced potential drop through the diffuse part of the electrical double layer and E_t is the tangential component of the electric field in the electrolyte bulk $(-\partial\phi/\partial x)$. In Levich (1962), the Helmholtz-Smoluchowski formula is shown to be also valid for perfectly polarizable metal surfaces in DC fields. Since ζ and E_t are both oscillating functions with the same frequency ω (the frequency of the applied voltage), the time-averaged electroosmotic velocity is non-zero. This velocity is the one measured in experiments. In González *et al.* (2000), these approximations to the problem are justified from first principles.

The ACEO model has successfully explained the experiments with pairs of coplanar electrodes (Green *et al.* (2000a, 2002a)). In Green *et al.* (2002a), experimental velocity measurements were fitted to the theoretical expectations. A model of the EDL consisting of a diffuse layer plus a compact or Stern layer was used. The surface capacitance of the diffuse layer can be estimated from the Debye-Hückel theory as ε/λ_D (Hunter (1993)). The compact layer capacitance is then adjusted to fit the experimental measurements. The voltage drop through the diffuse part of the double layer (which is the one supposed to be mobile) is reduced and, therefore, the ζ potential is not the total voltage drop through the EDL but a fraction of it, $\zeta = \Lambda(V - \phi)$.

Recent work on AC electroosmosis has been focused on extending the theory above in the following directions: modelling of the nonlinear charging of perfectly polarizable electrodes (Olesen *et al.* (2006); González *et al.* (2008a)), inclusion of Faradaic currents into the standard electrokinetic model (Olesen *et al.* (2006); Ramos *et al.* (2007)) and modelling of the effect of the finite size of ions (steric effects) at the electrode/electrolyte interface (Kilic *et al.* (2007a,b)).

In Ajdari (2000), net pumping of electrolytes with AC electroosmosis is theoretically predicted. Both the array of asymmetric pairs and the travelling-wave (TW) array try to exploit this phenomenon for that goal. In section 1.3, we apply the AC electroosmosis model to the case of a travelling-wave potential.

1.2.3 Electrothermally induced fluid motion

Changes in temperature through a liquid can induce gradients in its electrical properties (i.e. conductivity and permittivity). The action of an electric field on these inhomogeneities can give rise to a force in the liquid bulk and, as a consequence, generate fluid motion. That is the meaning of *Electrothermally induced motion.* It has been shown (Fuhr *et al.* (1992a); Green *et al.* (2001); González *et al.* (2006)) that this motion can be induced in electrolytes over microelectrode structures. A controlled heating by an external source (Felten *et al.* (2006)), Joule heating (Fuhr *et al.* (1992a)) or electrodes heated by microscope illumination (Green *et al.* (2000b)) are examples of heat sources that can induce gradients in the electrical properties of the liquid.

Electrical forces in the liquid bulk are given by the following expression (Stratton (1941)):

$$\mathbf{F}_E = \rho\mathbf{E} - \frac{1}{2}|\mathbf{E}|^2\nabla\varepsilon + \frac{1}{2}\left(\rho_m\left(\frac{\partial\varepsilon}{\partial\rho_m}\right)_T|\mathbf{E}|^2\right) \tag{1.10}$$

where ρ and ρ_m are the free electrical charge density and mass density, respectively. The last term in 1.10, the electrostriction, can be incorporated into the pressure for incompressible fluids (Stratton (1941)). The other two terms correspond, respectively, to the Coulomb and the dielectric forces.

Electrolytes are expected to be quasielectroneutral and, therefore, the Coulomb and the dielectric forces will be zero unless gradients in conductivity and permittivity are present. In effect, let us consider the conservation equation for the electrical current $\nabla\cdot\mathbf{J} = \nabla\cdot((\sigma+i\omega\varepsilon)\mathbf{E}) = 0$ (convection currents are neglected, Ramos *et al.* (1998)) and the Gauss' law $\rho = \nabla\cdot(\varepsilon\mathbf{E})$. For small gradients in permittivity and conductivity, the electric field can be expanded to give $\mathbf{E} = \mathbf{E}_0 + \mathbf{E}_1$, ($|\mathbf{E}_1| \ll |\mathbf{E}_0|$, $\mathbf{E}_0$ is the electric field in the absence of gradients), where the electric fields satisfy the equations:

$$\nabla \cdot \mathbf{E}_0 = 0 \tag{1.11}$$

$$\nabla \cdot \mathbf{E}_1 + \left(\frac{\nabla\sigma + i\omega\nabla\varepsilon}{\sigma + i\omega\varepsilon} \right) \cdot \mathbf{E}_0 = 0 \tag{1.12}$$

The charge density of each order correspond to

$$\rho_0 \;=\; \varepsilon\nabla \cdot \mathbf{E}_0 = 0 \tag{1.13}$$

$$\rho_1 \;=\; \varepsilon\nabla \cdot \mathbf{E}_1 + \nabla\varepsilon \cdot \mathbf{E}_0 = \left(\frac{\sigma\nabla\varepsilon - \varepsilon\nabla\sigma}{\sigma + i\omega\varepsilon} \right) \cdot \mathbf{E}_0 \tag{1.14}$$

If these gradients are generated by small changes in temperature, it can be shown that the time-averaged electrical force can be written as (Ramos *et al.* (1998)):

$$< \mathbf{F}_E >= \frac{1}{2}\mathrm{Re}\left[\frac{\sigma\varepsilon(\alpha - \beta)}{\sigma + i\omega\varepsilon}(\nabla T \cdot \tilde{\mathbf{E}}_0)\tilde{\mathbf{E}}_0^* - \frac{1}{2}\varepsilon\alpha|\tilde{\mathbf{E}}_0|^2\nabla T \right] \tag{1.15}$$

where $\tilde{\mathbf{E}}_0$ is the electric field phasor, * indicates the complex conjugate, $\alpha = (1/\varepsilon)(\partial\varepsilon/\partial T)$ and $\beta = (1/\sigma)(\partial\sigma/\partial T)$.

Expression 1.15 for the electrical forces is frequency dependent. If ω is much greater than σ/ε the dielectric force dominates. Likewise, if $\omega < \sigma/\varepsilon$ the Coulomb force dominates because relative variations in conductivity ($\nabla\sigma/\sigma$) are usually much greater than relative variations in permittivity ($\nabla\varepsilon/\varepsilon$).

The use of travelling-wave electric fields for pumping liquids with a given temperature gradient was proposed in Melcher (1966) and Melcher & Firebaugh (1967). This idea has been used for pumping electrolytes in microsystems with microelectrode arrays subjected to travelling-wave potentials (Fuhr *et al.* (1992b); Felten *et al.* (2006)). However, electrothermal effects can be discarded to have any effect on the velocity measurements performed during this thesis work. Typical voltages in our experiments are too low to generate conductivity gradients through Joule heating.

1.2.4 Electrohydrodynamic instabilities in microfluidics

Our experimental observations with platinum microelectrode arrays suggest that EHD instabilities may appear. For certain values of frequency and voltage amplitude of the applied signal, we have observed nonuniform fluid motion. Despite we do not treat fluid flow instabilities in this work, it is worth to mention the possibility that AC fields can induce instabilities within microchannels. Recent theoretical and experimental work on EHD instabilities has been done for microsystems where a conductivity gradient is imposed (Baygents & Baldessari (1998); Lin *et al.* (2004); Chen *et al.* (2005); Boy & Storey (2007)). Experiments on EHD instabilitites in microchannels are, typically, based on two coflowing fluids with different conductivities that are subjected to electric fields. Electric charge can be induced at the interface between them and the resulting electrical force drives the instability.

Another kind of instabilities in microsystems, as those studied by Rubinstein & Zaltzman (2000, 2007), may appear at high current densities. They are associated to depletion of electrolyte near a semipermeable membrane and electroconvection is generated (either in the bulk or in the double layer).

Fluid flow instabilitites are of general interest in microfluidic applications. They can be useful for achieving rapid mixing (Oddy *et al.* (2001); Nguyen & Wu (2005); Hardt & Schönfeld (2008)) or they may want to be avoided if they can cause undesirable dispersion in sample injection, separation and stacking. In the experiments here presented, conductivity gradients in the electrolyte may appear as a consequence of electrochemical reactions at the electrodes. This could explain our observations of non-uniform motion as EHD instabilities.

1.3 Electrokinetic Micropumps: Travelling-Wave Electroosmosis

As mentioned in the introduction, pumping in microsystems is one of the main concerns in microfluidics research. Fluids must typically be introduced into, and transported within, the microfluidic circuits. Reliable and cheap micropumps are still to be developed. Not only pumping but the generation and control of secondary flows could improve many microfluidic chips. Local actuaction on the main flow may render possible the realization of ports, valves and control of the flow direction.

In a recent review (Laser & Santiago (2004)), micropumps are classified into two groups: *displacement pumps and dynamic pumps. Displace-*

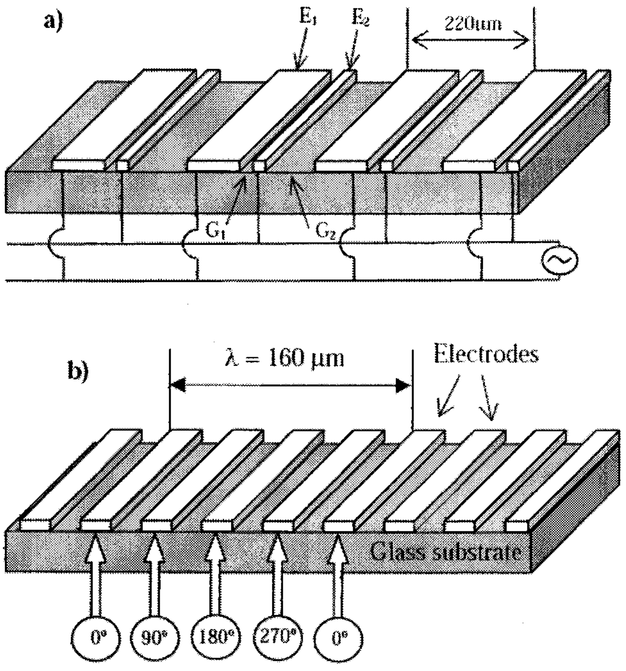

Figure 1.2: Schematic diagram of the two kinds of microelectrode arrays: (a) asymmetric electrodes array and (b) travelling-wave array.

ment pumps are those in which one or more moving boundaries establish pressure differences on the working liquid, on the other hand, in *dynamic pumps* the forces are applied directly on the liquid. Both electric and magnetic forces can be exploited for dynamic pump purposes. When electric fields are used we refer to electrohydrodynamic (EHD) pumps, while magnetohydrodynamic (MHD) pumps is the term in the case of magnetic fields. In Ramos (2007), EHD and MHD micropumps are further classified into the following:

- Micropumps where electrical forces act on the liquid bulk: *EHD injection* (Richter & Sandmaier (1990)), *conduction* (Atten & Seyed-Yagoobi (2003)) and *induction* (Fuhr *et al.* (1992a)) *pumps*.
- Those where electrical forces act in the diffuse part of the electrical

double layer -*Electrokinetic micropumps-*: *DC Electroosmotic* (Pretorius *et al.* (1974)) and *AC Electroosmotic* (Brown *et al.* (2000)) *micropumps.*

- When magnetic forces are applied in the liquid bulk: *DC* (Jang & Lee (2000)) and *AC* (Lemoff & Lee (2000)) *MHD micropumps.*

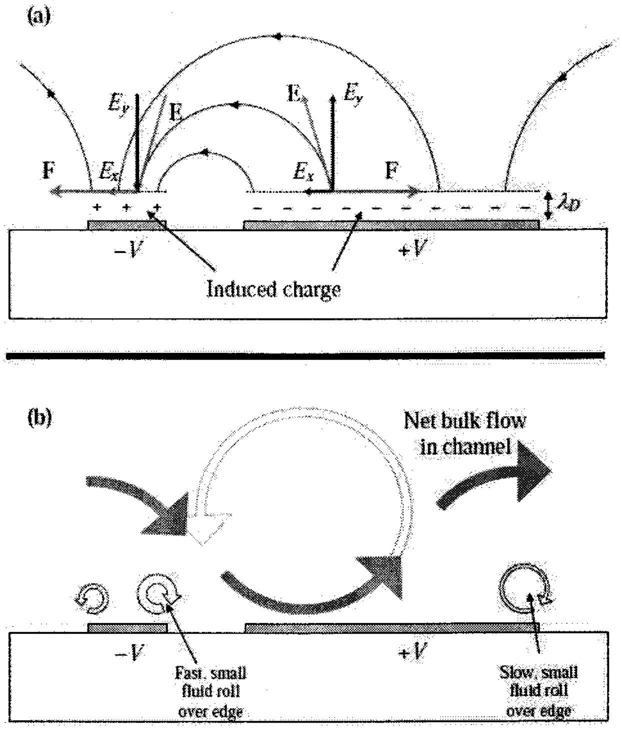

Figure 1.3: AC electroosmosis mechanism for a couple of asymmetric electrodes. Fluid flow rolls are formed over the electrodes and a net flow is generated.

In this work we deal with *electrokinetic micropumps* driven with AC signals. In general, these micropumps work with electrolytes of low conductivity and for low voltage and frequency signals. As mentioned in the introduction, two kinds of microelectrode structures are used with the aim of generating a net flow: *arrays of asymmetric pairs of electrodes* subjected to an AC potential (Brown *et al.* (2000); Studer *et al.* (2004)) and *arrays of equal sized electrodes subjected to a travelling-wave potential* (Cahill *et al.* (2004); Ramos *et al.* (2005)), see fig.1.2. Both designs are examples of how to exploit AC electroosmotic motion for generating a net pumping within a microchannel. As predicted by Ajdari (2000),

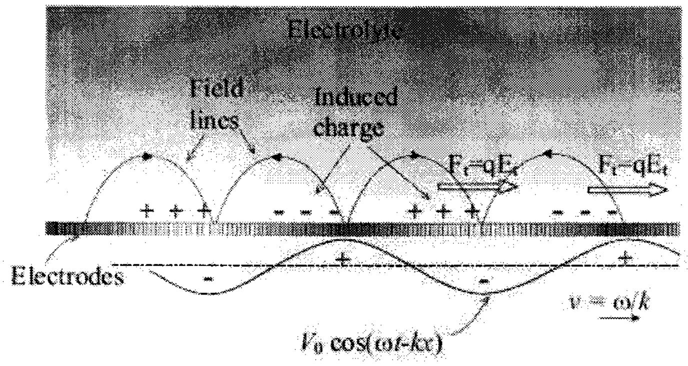

Figure 1.4: Physical mechanism of Traveling Wave Electroosmosis. A sinusoidal potential is travelling to the right. Electrical charge is induced at the electrode/electrolyte interface and a net force pulls the charges.

asymmetries in microelectrode structures can be used to rectify electroosmotic flows and, consequently, give rise to a net unidirectional flow over these electrodes.

Fig. 1.3 illustrates the ACEO basic mechanism for a couple of asymmetric electrodes. Two fluid rolls are formed over the electrodes as a consequence of the slip electroosmotic velocity on them. Since one electrode is larger than the other, the two rolls are of different sizes and one dominates over the other, giving rise to net flow in the direction indicated in the picture. Besides of the theoretical prediction by Ajdari, a rigorous mathematical treatment can be found in Ramos *et al.* (2003) (linear ACEO model is used) and Olesen *et al.* (2006) (weakly nonlinear theory for ACEO is applied and Faradaic currents are included in the model).

We focus primarily on the study of pumping of electrolytes with travelling-wave potentials. Experiments with asymmetric arrays are also included for the sake of comparison. Fig. 1.4 shows the physical mechanism of *Travelling-wave Electroosmosis.* Ions accumulate at the electrode/electrolyte interface in response to the applied potential. Due to the finite charging time of the electrical double layer, a delay exists between maximum electric field and maximum induced charge in that layer. The electric field pulls the charges generating fluid flow in the same direction of the travelling-wave.

In Ehrlich & Melcher (1982), the fluid motion induced by a travelling-wave field acting on the charge induced in the electrical double layer is studied for the first time. However, they analyzed the case of a semi-insulating bipolar liquid and a thick dielectric layer between the electrodes and the liquid. This is different from our system, which consists in an electrolyte in contact with the electrodes. The time-averaged slip velocity can be easily calculated for the case in Fig. 1.4, in which the electric potential at the level of the electrodes has the form $V(x,t) = V_0 \cos(\omega t - k_0 x)$, where ω is the angular frequency of the applied signal and k_0 is the wave-number that characterizes the spatial periodicity. Making the assumptions of thin electrical double layer and electrolyte in quasiequilibrium (as in section 1.2.2), the electric potential in the bulk is solution of Laplace's equation $\nabla^2\phi = 0$ and, making use of phasors $\phi = \mathrm{Re}[\Phi e^{i\omega t}]$, the boundary condition for the electric potential at the electrodes level ($y = 0$) is given by:

$$-\mathbf{n} \cdot \nabla\Phi = \frac{i\omega C_{DL}}{\sigma}(V_0 e^{-ik_0 x} - \Phi) \tag{1.16}$$

The solution of Laplace equation has the form $\phi = Ae^{-k_0 y}e^{i(\omega t - k_0 x)}$. After applying 1.16 it is obtained:

$$A = \frac{i\Omega V_0}{1 + i\Omega} \tag{1.17}$$

where $\Omega = \omega C_{DL}/(\sigma k_0)$.

Once the electric potential has been solved, the electroosmotic fluid velocity can be calculated from the Helmholtz-Smoluchowski formula $u_{slip} = (\varepsilon/\eta)\Delta\phi E_t$. The voltage drop through the diffuse layer $\Delta\phi$ can be written as $\Lambda(V - \phi)$, where Λ is defined as the ratio of the voltage drop through the diffuse layer to the total voltage drop through the double layer. When the EDL is modelled by two capacitors in series, this parameter can be written as $\Lambda = C_s/(C_s + C_d)$, where C_d is the surface capacitance of the diffuse layer and C_s is the surface capacitance of the compact or Stern layer. The time-averaged slip velocity is given by:

$$\langle u \rangle = -\frac{\varepsilon}{4\eta}\Lambda\frac{\partial}{\partial x}|\Phi - V_0|^2 \tag{1.18}$$

After introducing the solution for the potential, the generated electroosmotic slip velocity is (Ramos *et al.* (2005)):

$$U = \Lambda\frac{\varepsilon k_0 V_0{}^2}{2\eta}\frac{\Omega}{1 + \Omega^2} \tag{1.19}$$

Fig. 1.5 shows the slip electroosmotic velocity (in units of $\Lambda\varepsilon k_0 V_0{}^2/4\eta$) versus the nondimensional frequency Ω. A bell shape function is obtained

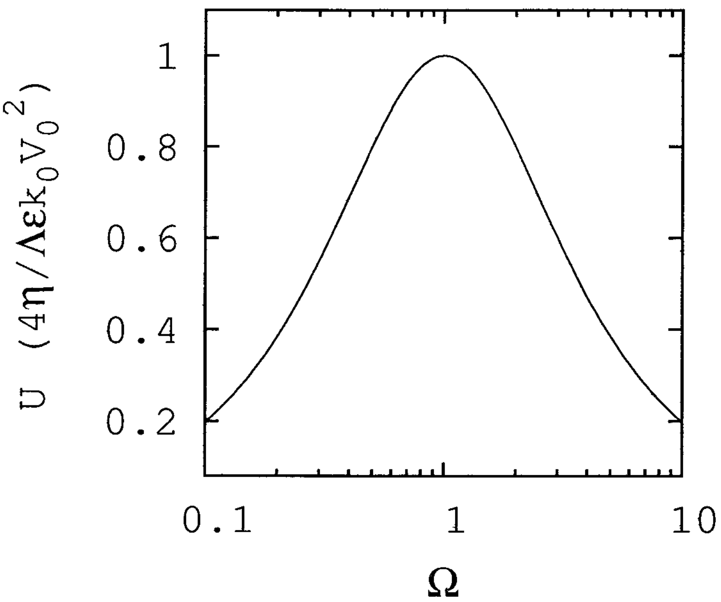

Figure 1.5: Electroosmotic slip velocity for a sinusoidal travelling-wave potential versus nondimensional frequency $\Omega = \omega C_{DL}/(\sigma k_0)$. Maximum velocity is obtained for $\Omega = 1$.

with peak velocity $U = \Lambda \varepsilon k_0 V_0{}^2/4\eta$ at $\Omega = 1$, the characteristic charging frequency. For frequencies much greater than this, the induced charge is negligible. On the other hand, for frequencies much smaller than $\Omega = 1$, the induced charge is maximum but there is no time delay between this and the AC signal.

The *pumping velocity* is defined as the average electroosmostic velocity at the level of the electrodes. In the case of a purely sinusoidal travelling-wave potential, all points are equivalent and the average velocity is just the electroosmostic velocity. If we consider the potential generated by the four-phase shifted configuration, the maximum pumping velocity is found to be $U = 0.052\Lambda\varepsilon k_0 V_0^2/\eta$ at a nondimensional frequency $\Omega = 1.4492$ (Ramos *et al.* (2005)). A theoretical analysis of travelling-wave electroosmosis considering the nonlinear charging of the electrical double layer is found in González *et al.* (2008a). In Ramos *et al.* (2007), the effect of Faradaic currents in the linear regime is included in the study of travelling-wave electroosmosis.

1.4 Thesis Outline

The main goal of this work is the description of electrolyte flows generated by arrays of microelectrodes subjected to travelling-wave potentials. The array of asymmetric pairs of electrodes has been studied by other groups (Brown *et al.* (2000); Ramos *et al.* (2003); Mpholo *et al.* (2003); Studer *et al.* (2004); Gregersen *et al.* (2007)) and we consider them here for the sake of comparison. A careful experimental study is pursued. This includes not only fluid flow observations but the measurement of other relevant physical quantities that we can access. Theoretical modelling and computations are performed in order to provide physical insight on the underlying mechanisms. We do not only aim at the characterization of the flow generated by the travelling-wave device but shed some light on electrokinetic phenomena at higher voltages. The work is organized as follows:

The flow generated by a couple of coplanar electrodes is studied in chapter 2. Earliest experiments and theories on AC electroosmosis (ACEO) are based on this geometry (Green *et al.* (2000a); Ramos *et al.* (1999a); González *et al.* (2000)). The ACEO theory was succesfully tested with this electrode structure subjected to AC signals of amplitude around 1-2 V_{pp}. However, voltage amplitudes applied to microelectrode arrays exceed those values, they typically reach 7-8 V_{pp}. Therefore, in chapter 2 we study the fluid flow generated by a couple of symmetric electrodes within a wider voltage range than in previous works.

Experiments with titanium arrays are presented in chapter 3. Two different kinds of microelectrode structures are used: an array of equal sized electrodes (subjected to a TW potential) and an array of asymmetric pairs of electrodes. A comparison between arrays is done. The predictions of the AC Electroosmosis theory are compared to experimental observations. At low voltages, the experiments are in qualitative agreement with the theoretical results. The experimental observations at higher voltages can not be explained by the theory, even the direction of the net flow is opposite to prediction (flow reversal).

Chapter 4 shows the experimental results obtained with platinum travelling-wave arrays. Fluid flow observations with arrays of two different electrode sizes (10 and 20 μm) are compared to titanium arrays. A thorough experimental study is performed: fluid velocities are measured, electrical impedance and currents measurements are taken, the influence of channel height and shape is explored, the effect of electrolyte conductivity is analyzed and the behaviour of molecular fluorescent dyes is studied. We draw conclusions from these experiments and justify the theoretical work performed in the next chapters. This work consists of the two following points:

(1) In chapter 5, the effect of Faradaic currents in travelling-wave electroosmosis is modelled in the linear regime. This model represents a more general approach to the polarization of the electrode/electrolyte interface at low applied voltages - electrochemical reactions are allowed to ocurr.

(2) From the experimental observations, we postulate that electrical charge in the electrolyte bulk may be induced as a consequence of gradients in ionic concentrations. In chapter 6, numerical computations are performed in order to show how the electrical forces due to the induced charge in the electrolyte bulk can lead to a net motion over a TW microelectrode array.

We also include a chapter where the influence of the electrode height on the performance of travelling-wave electroosmosis (TWEO) micropumps is studied theoretically (chapter 7). The linear ACEO including Faradaic currents theory is applied and an optimum electrode height is found. The results are compared to previous theoretical work with asymmetric arrays.

Finally, we present the general conclusions of the thesis and discuss future work.

In appendices, we included additional experimental work related to fluid manipulation with microelectrodes: *Control of two-phase flows by AC electric fields* (appendix A) and *Electrolyte Flow induced by AC Voltages in a Point-Plane Electrode Microsystem* (appendix B). Experimental fluid velocities in this thesis were obtained with a Particle Tracking Velocimetry software written in Matlab. Appendix C describes this software and includes an example of how to use it.

Chapter 2

Fluid flow over a pair of microelectrodes. Preliminary experiments

A pair of coplanar electrodes is the simplest electrode structure for the experimental study of AC electroosmosis. Fig. 2.1 shows a scheme for the general case of two electrodes of different width (W_1 and W_2). Pioneering experiments and theories on ACEO (Ramos *et al.* (1999a); Green *et al.* (2000a); González *et al.* (2000)) are based on this geometry - two coplanar metal electrodes of the same size, $W_1 = W_2$. Direct observation of fluorescent beads moving close to the electrodes allowed the experimental characterisation of the phenomenon at low voltages 1-2 V_{pp}. The theoretical framework in González *et al.* (2000) was successfully applied for predicting the fluid velocity over titanium electrodes for low voltage amplitudes 0.5 V, (Green *et al.* (2002a)) [1]. In that paper, side view of the electrodes allowed the visualisation of fluid velocity streamlines. Very good agreement with the theoretical streamlines was found.

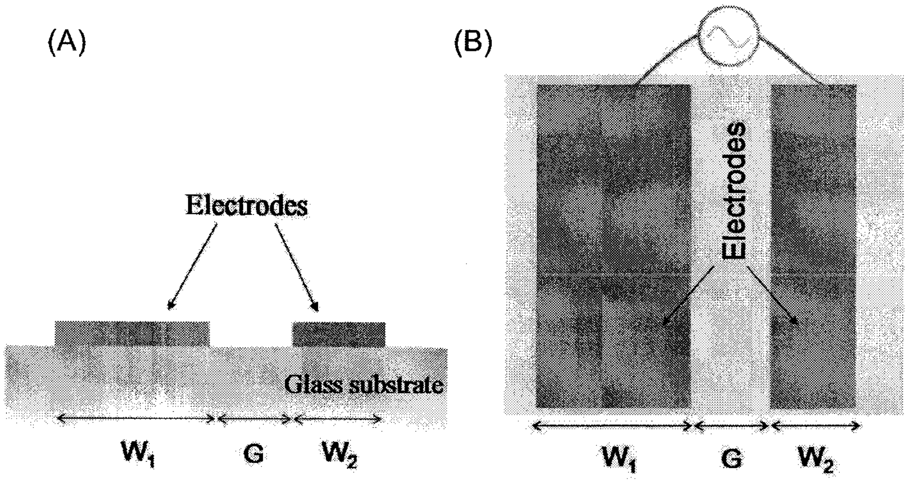

Figure 2.1: A couple of coplanar electrodes: (A) side view, (B) top view.

The voltage amplitudes used in the experiments with microelectrode arrays exceed the typical voltages in the previous experiments with pairs of electrodes. It is therefore convenient to inspect the fluid flow generated by pairs of electrodes subjected to AC signals of amplitude up to 7-8 V_{pp}, which are the maximum amplitudes used in the experiments with arrays in the present thesis. In this chapter, we present measurements of the

---

[1] The deviation of the experimental values from the theoretical prediction was ascribed to the presence of a compact layer of titanium oxide on top of the electrodes

fluid velocity on top of a couple of titanium electrodes of the same width. We also introduce the experimental procedure for fluid flow observation over microelectrode structures.

2.1 Experimental details

A pair of plate electrodes of the same width was used for the measurement of the AC electroosmotic velocity. The electrodes were fabricated on a planar glass substrate using photolithography, consisting of layers of 10 nm titanium, 100 nm gold and 20 nm titanium. The electrodes were 2 mm long and 500 μm wide ($W_1 = W_2$), the gap between electrodes (G) was 25 μm. The two electrodes were subjected to AC signals provided by a function generator (Thurlby Thandar Instruments TGA 1244). KCl aqueous solution was used as working fluid, the conductivity of this solution was 2.1 mS/m. A rectangular chamber made of PDMS (polydimethilsiloxane) was placed on top of the electrode structure (Fig. 2.2). The chamber was 5 mm long, 2 mm wide and 1 mm high. The PDMS sticks on the glass and the liquid was contained inside the chamber. A microscope coverslip was placed on top of the liquid and PDMS and the device was then ready to do experiments.

Fluorescent latex spheres (500 nm diameter) were suspended in the electrolyte and used as flow tracers. An Epi-fluorescence microscope (Nikon-Optiphot100) with a X20 objective was used for visualising the beads. The light source was a mercury lamp and a suitable filter set for FITC fluorescence was employed. In experiments where the beads were moving faster than 100 μm/s, we had to use a fast camera for tracking the beads. A regular camera is capturing 25 frames per seconds (fps). Framerates up to 250 fps were necessary in order to correctly track the beads.

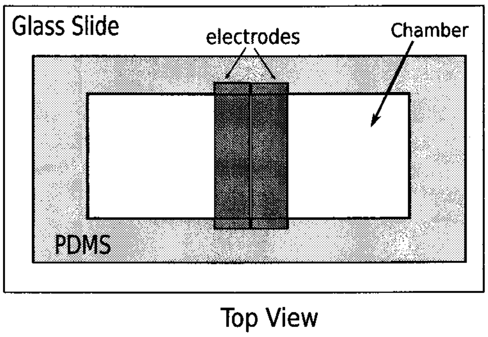

Figure 2.2: Top view of the pair of electrodes and the PDMS chamber.

The only drawback of using a fast camera is that it requires higher light intensity than a regular CCD camera. The fluorescence emitted by the beads was not enough to clearly distinguish them in the video recordings. Nevertheless, 500 nm beads can be resolved without fluorescence illumination. Therefore, the experiments with the fast camera were carried out with white illumination - no fluorescence filters.

Videos of the beads motion were captured and stored in a computer. The fluid velocity was later measured by tracking the motion of the beads through the video frames. Both manual tracking (finding the position of a given bead in every frame) and using the particle tracking program described in appendix C produced the same results.

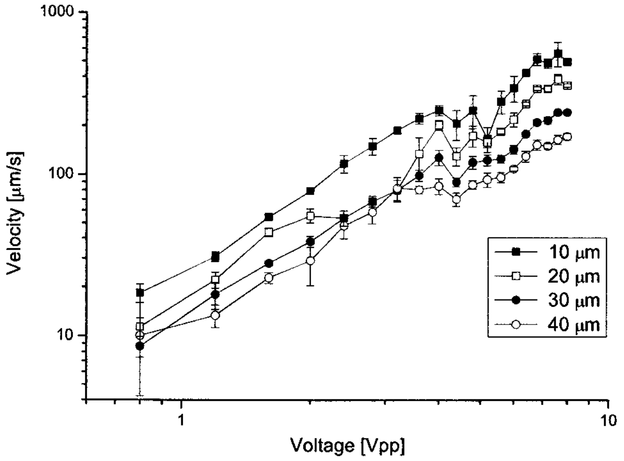

Figure 2.3: Fluid velocity versus voltage at different positions for a frequency of 200 Hz.

2.2 Results and discussion

After applying the AC signals to the electrodes, the flow tracers at the electrodes level move away from the interelectrode gap. Focusing a few tens of microns above the electrode, one can see beads moving in the opposite direction. This shows the fluid recirculation. Fluid rolls are formed on top of the two electrodes, as expected in AC electroosmosis. Fig. 2.3 shows the measurements of the fluid velocity versus applied voltage for a frequency of 200 Hz. The velocity is measured at four different distances from the electrode edge on the gap side: 10, 20, 30 and 40 μm. At a first glance, one can infer that the velocity shows a square-law dependence on the applied voltage, as expected from the AC electroosmosis theory. The trend is actually smaller, but velocity increases nearly as V^2.

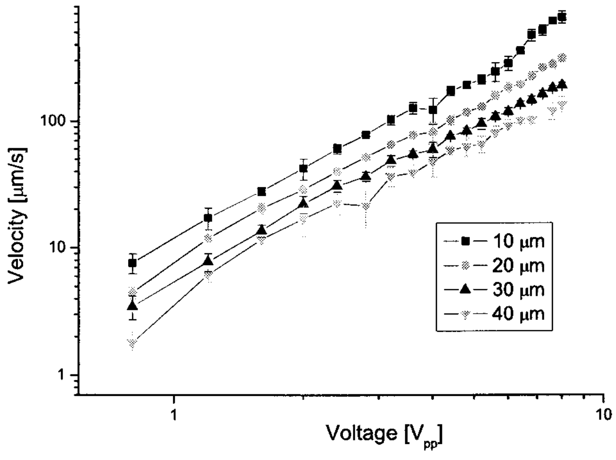

Figure 2.4: Fluid velocity versus voltage at different positions for a frequency of 400 Hz.

Fig. 2.4 and 2.5 show the measurements of the fluid velocity versus applied voltage for a frequency of 400 Hz and 1200 Hz, respectively. The velocity is measured again at four different distances from the electrode edge on the gap side: 10, 20, 30 and 40 μm. The velocity increases nearly as the square of the voltage. At voltages lower than 4 V_{pp} the velocities are higher at 200 Hz than at 400 Hz or 1200 Hz. This is in accordance with the results in Green *et al.* (2000a), where the frequency for maximum velocity was around 200 Hz. This is not the case at higher voltages at which the frequency for maximum velocity depends on the position. For example, the velocity at 10 μm from the electrode edge is maximum at 1200 Hz but at 40 μm the maximum velocity is found at 200 Hz.

The theoretical square-law dependence of ACEO on voltage arises from the assumption that the net electrical charge at the electrode-electrolyte interface is proportional to the applied voltage, the electrical force then scales with V^2 and so does the velocity. Some saturation of the EDL charging mechanism could be expected as the voltage increases (Olesen *et al.* (2006)), the velocity would then have a smaller dependence

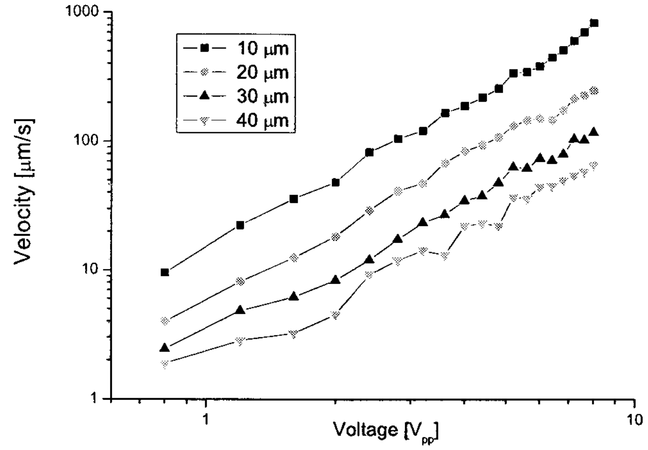

Figure 2.5: Fluid velocity versus voltage at different positions for a frequency of 1.2 kHz.

on voltage. This is not observed since velocities increase nearly as expected from the linear theory. If we fit the experimental measurements at low voltage to the theoretical prediction (as in Green *et al.* (2002a)), it is found $\Lambda = 0.095$ (Λ is defined as the ratio of the voltage drop through the diffuse layer to the total voltage drop through the double layer). As can be found from the nonlinear analysis by González *et al.* (2008a), higher applied voltages would be required for this value of Λ in order to see a saturation of the velocity. It should also be noted that, at the voltages we are reaching in these experiments, dielectrophoretic forces could be acting on the particles near the electrodes and, therefore, these particles do not accurately map the fluid flow.

As a general conclusion of these preliminary experiments, we obtain that velocity measurements do not deviate noticeably from the trends predicted by the linear theory of ACEO. If we perform experiments with arrays of electrodes subjected to AC signals, it then makes sense that the fluid flow behaviour could be predicted from this theoretical background. Nevertheless, this assumption fails as will be shown in the following chapters.

Chapter 3

Experiments with arrays of titanium: Flow observations and velocity measurements

This chapter includes the experimental results obtained with microelectrode arrays made of titanium. We make use of two different electrode arrays: A travelling-wave microelectrode array and an array of asymmetric pairs of electrodes. Pumping of electrolytes using an asymmetric electrode array has been characterised by other groups (Brown *et al.* (2000); Mpholo *et al.* (2003); Studer *et al.* (2004); Gregersen *et al.* (2007)). We pay particular attention to the travelling-wave array (which is the subject of this thesis) and we include the experiments with the array of asymmetric pairs for the sake of comparison.

3.1 Experimental Details

The array of asymmetric pairs consists of ten pairs of electrodes of different size, see Figure 1.2(a). The larger electrodes (E_1) are 100 μm wide while the smaller (E_2) are 10 μm. The electrodes of every couple are separated by a gap (G_1) 10 μm wide. The distance between pairs of electrodes is (G_2) 100 μm, so the spatial periodicity is 220 μm. The array has a total length of 2100 μm. The electrodes were fabricated on a planar glass slide using photolithography techniques and they consist of three metal layers of different thickness: 10 nm titanium, 100 nm gold and 10 nm titanium. The titanium layer is used because it sticks to the glass, the gold layer enhances the electrode conductivity and the top layer of titanium has the purpose of reducing corrosion for low frequency applied signals. An AC signal generator is used to subject each pair of electrode to a voltage difference of amplitude V_0 and frequency ω.

The microelectrode array used in the travelling-wave (TW) experiments consists of 20 electrodes fabricated on glass as in the case of the asymmetric array. The electrodes are 20 μm wide separated by 20 μm gaps. Each electrode is driven by an AC voltage of amplitude V_0 and frequency ω. The voltage on consecutive electrodes is phase shifted by 90^o, as shown in Figure 1.2(b). This produces a travelling-wave potential with a wavelength of 160 μm.

A long glass square chamber was built for each array. Small glass pieces are cut from microscope coverslips and glued onto the device. For the travelling-wave device the chamber height was 200 μm, whilst the asymmetric device had a chamber height of 260 μm. The channel has an inlet and an outlet at both ends and it could be filled by manual pipetting. KCl solutions 0.1 mM were used as working electrolyte. Fluorescent latex particles (500 nm diameter) were suspended in the electrolyte and

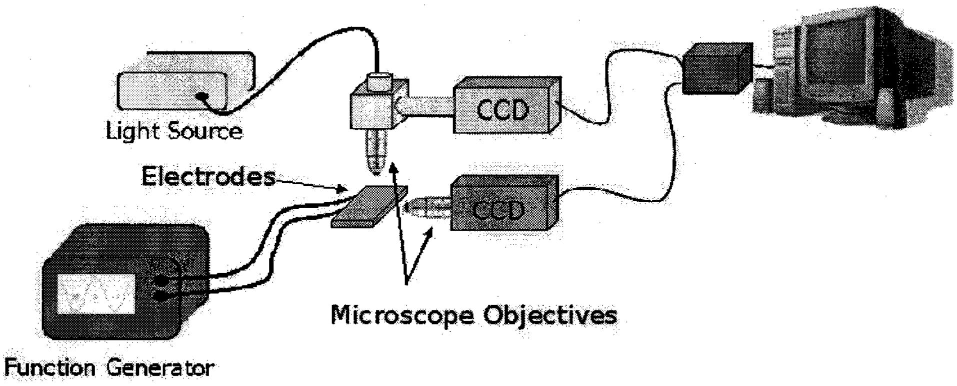

Figure 3.1: Scheme of the experimental setup for fluid flow visualisation. Top and side view can be performed.

used as flow tracers. Suitable excitation and emission fluorescence filters are used in order to visualise the fluorescence emission of the flow tracers.

Fig. 3.1 shows a scheme of the experimental setup for these experiments. Electrode pads allow to make the electrical connections on one side of the array. The other side is free and a microscope objective and camera were pointed horizontally along the electrodes, so that the electrodes could be imaged in cross section. Fluid flow was observed both from above and from the side. Observations of the fluid flow were recorded on video and transferred to a computer. The fluid velocity measurements were carried out with the use of a software for particle tracking velocimetry (PTV) written in *Matlab* (see Appendix C).

3.2 Travelling-Wave Array of Titanium

When the 4-phase AC signal is applied to the electrode array, fluid flow is driven at the electrode surface. An example of fluid flow above the electrodes for the travelling-wave pump is shown in Figure 3.2. This image is of fluid motion viewed from the side with the electrodes in the bottom of the image. The fluorescent tracer particles are used to plot the pathlines by superimposing successive video frames (50 in this case). The chamber is closed at both ends so that the fluid recirculates. This can be seen in the figure where the tracer particles at the top move in the opposite direction to those above the electrodes in the bottom half of the chamber.

A typical plot of the horizontal fluid velocity measured as a function

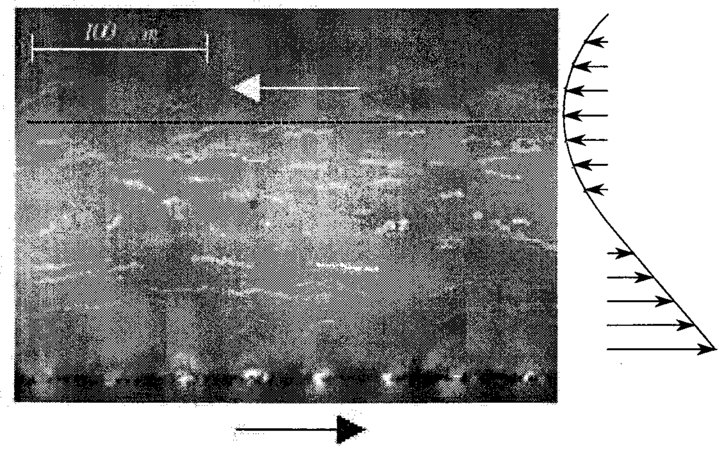

Figure 3.2: Particle paths for the travelling-wave array for an applied signal of 1 kHz and 5 V_{pp}. The black arrow indicates the direction of the fluid flow at the electrode level, and the white arrow the direction at the top of the chamber. The dashed line is placed at the height where the fluid velocity in Fig. 3.4 is measured.

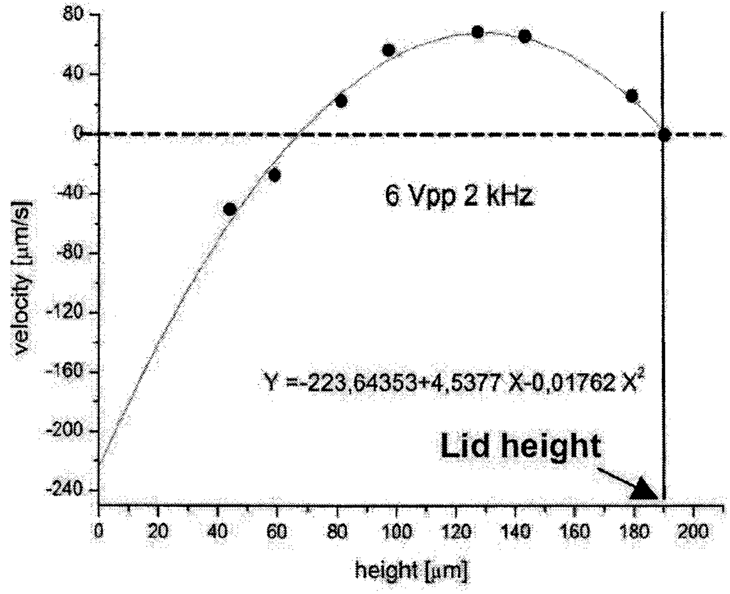

Figure 3.3: Horizontal velocity versus height for an applied signal of 2 kHz and 6 Vpp (travelling-wave array)

of height above the electrodes is shown in Figure 3.3. This was taken for a voltage of 6 V_{pp} at a frequency of 2 kHz. Similar profiles were obtained for other frequencies and voltages. The experimental velocity profile can be fitted to a parabola with the maximum speed at the electrodes (solid line in the figure). This velocity profile has zero net flux, as expected for a 2D flow when the chamber is closed at both ends. This profile corresponds to the theoretical prediction obtained from the Stokes equation with no volumetric force and non-slip velocity condition at the top boundary and slip condition at the bottom boundary. The experimental curve shows that the fluid is driven at the electrodes, and recirculates at the top of the chamber with a total flux equal to zero. The average velocity at the level of the electrodes can be estimated by extrapolating the velocity profile as shown in the figure.

The pump behaviour was characterised as a function of voltage and frequency by measuring the fluid velocity at a height of 140 μm above the electrodes (dashed line in Fig. 3.2). At this height the fluid is moving in the opposite direction to that at the electrode surface. Measurements at this height were considered to be representative of the global behaviour of the pump as indicated by the profile of Figure 3.3.

A 2-D map of these measurements plotted in the voltage versus frequency domain is shown in Figure 3.4. Values of velocity are negative when the fluid is dragged on the electrodes in the direction of the travelling electric field. At low voltages, the fluid is dragged in this direction, i.e. negative velocity values. We refer to this mode of behaviour as *Normal Pumping.* This is the mode of pumping that is predicted by the low voltage theory of AC electroosmosis (Cahill *et al.* (2004); Ramos *et al.* (2005)). At higher voltages, the fluid is driven in the opposite direction, a mode of behaviour we designate as *Reverse Pumping.* The physical mechanism responsible for this behaviour is not clear at present.

Four separate regions can be distinguished in Figure 3.4: *normal pumping, reverse pumping, no net pumping* and *electrolysis.* The latter corresponds to a region of very low frequencies and high voltages which is generally destructive owing to bubble formation because of electrolysis. There is a region of voltage where the pumping mechanism changes from normal to reverse pumping. No net flow was observed in this region. Fluid rolls occurred over the electrodes but these did not lead to unidirectional fluid flow. Therefore, we designate this region as *No Net Pumping.*

Figure 3.5 shows the recirculation magnitude of the velocity for the

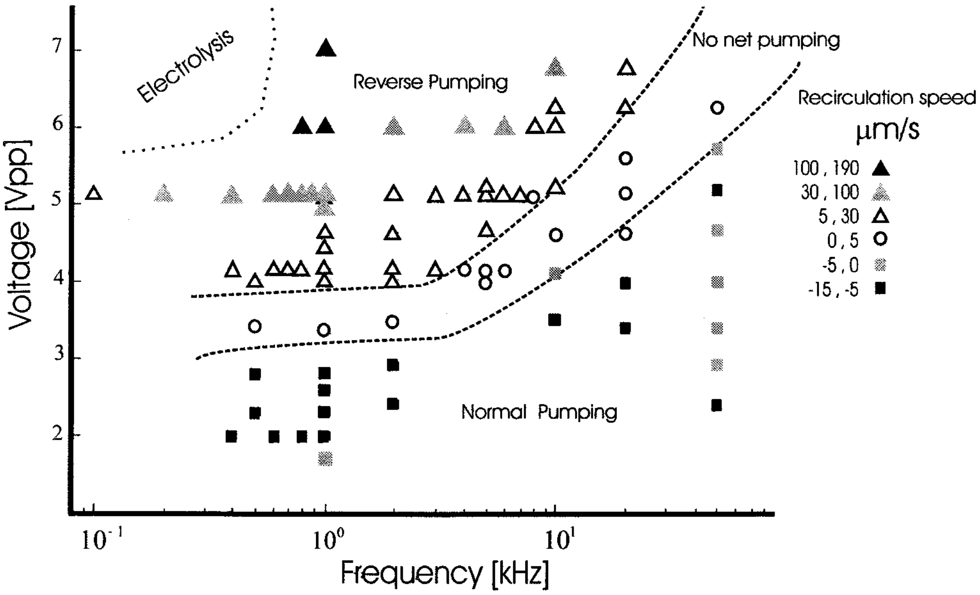

Figure 3.4: Velocity map for the travelling-wave array of microelectrodes in the plane voltage versus frequency. Velocities are measured at a height of 140 μm (dashed line in Figure 3.3)

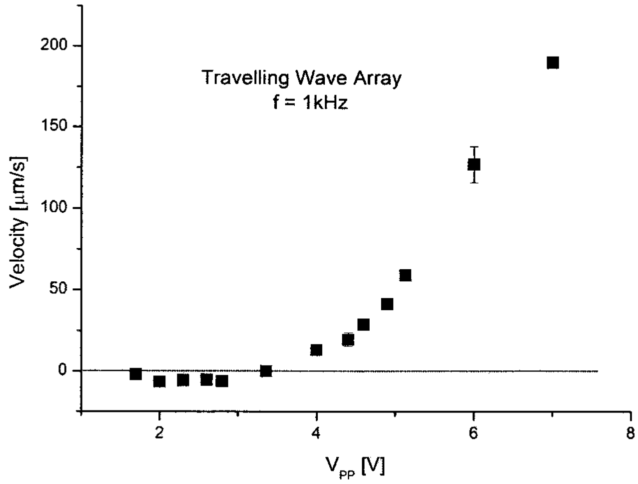

Figure 3.5: Horizontal velocity at a height of 140 μm versus voltage for a given frequency of 1 kHz (travelling-wave array).

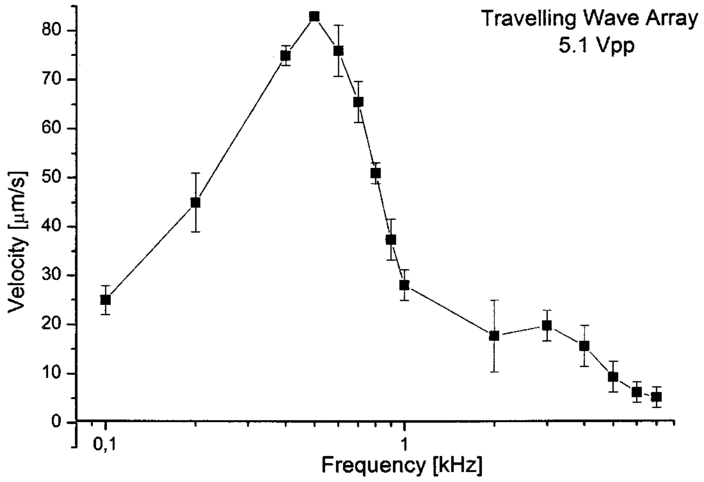

Figure 3.6: Horizontal velocity at a height of 140 μm versus frequency for a given voltage of 5.1 V_{pp} (travelling-wave array).

pump at a frequency of 1 kHz as a function of voltage. At low voltages normal pumping is observed. The velocity amplitude increases only slightly with voltage until saturation and then no net pumping is observed. At a voltage of 4 V_{pp}, the fluid velocity begins to increase again (in the opposite direction) as reverse pumping occurs. The velocity amplitude then increases rapidly with voltage as shown in the figure. At 7 V_{pp} the fluid speed is 200 μm/s, corresponding to an average velocity of 600 μm/s at the level of the electrodes.

Figure 3.6 shows a plot of the velocity against frequency at a constant voltage (5.1 Vpp). The liquid flow corresponds to the region of *Reverse Pumping* in Fig. 3.4. The velocity reaches a maximum at a frequency of approximately 500 Hz.

For a 4-phase travelling-wave signal the low voltage model predicts a maximum pumping velocity at the electrodes given by $U = 345\Lambda V_{pp}^2$ μm/s (section 1.3). The fluid velocity at the level of the electrodes can be determined by extrapolation of the experimental data. For the electrode array used in this work, and for a signal of amplitude 2 V_{pp} and frequency 600 Hz, the measured velocity was 38 μm/s. A comparison with theory shows that $\Lambda \sim 0.03$, a small value if compared to those obtained for a pair of electrodes: $\Lambda \sim 0.2$ in Green *et al.* (2002a) and $\Lambda \sim 0.1$ in chapter 2. This small value for Λ can be in part explained by the fact

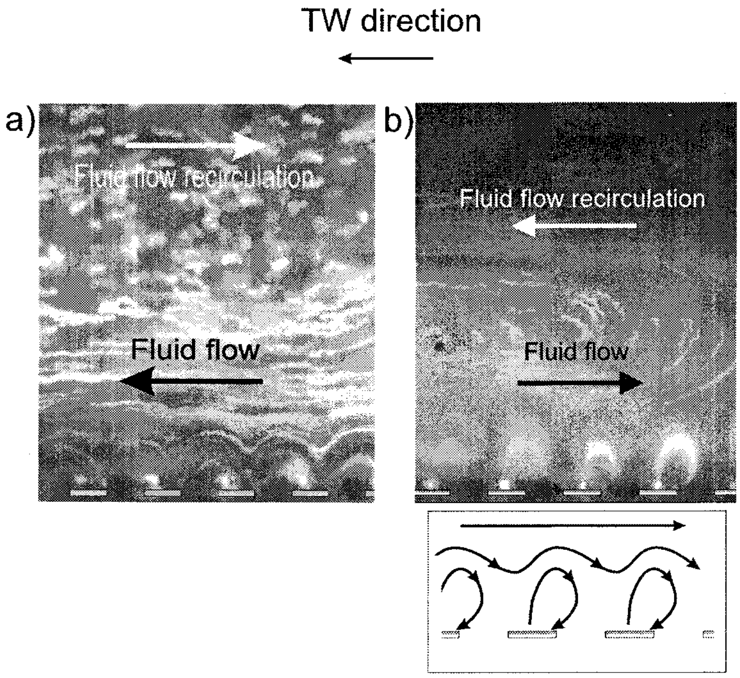

Figure 3.7: Pathlines over a travelling-wave array. (a) 2.4 V_{pp} and 1 kHz (Normal pumping). (b) 4.13 V_{pp} and 800 Hz (Reverse pumping), the drawing below shows the particle motion direction.

that the oxide layer which forms on top of the titanium electrode reduces the voltage across the diffuse layer.

Fig. 3.7 shows pathlines of the fluorescent beads over the travelling-wave array. Fig. 3.7(a) corresponds to an applied signal of 2.4 V_{pp} and 1 kHz (reprinted from Ramos *et al.* (2005)). In this case the net flow is in the direction predicted by the AC electroosmosis theory and the pathlines fit to the theoretical streamlines expected by that theory. Fig. 3.7(b) is for an applied signal of 4.13 V_{pp} and 800 Hz. The array is pumping the liquid in the reverse direction. No theory currently predicts the shape of these pathlines but they are clearly different from the pathlines at low voltage. These pathlines cannot be obtained just by changing the fluid velocity direction at the level of the electrodes of Fig. 3.7a). Fluorescent beads accumulate at the centre of the electrodes and some beads are strongly ejected in the vertical direction, forming clockwise rotating "flow rolls" on the right side of the electrodes (the potential travels from right to left). Particles are also subjected to electrical forces near the electrodes, these particles do not accurately map the fluid flow

3.3 Asymmetric Array of Titanium

Figure 3.8 shows the magnitude of the fluid velocity as a function of voltage, measured at a height of 210 μm above the electrodes at a frequency of 10 kHz. The velocity at this height is considered representative of the global behaviour of the pump since it is in the region above the fluid rolls where the fluid recirculates. At the frequency of 10 kHz the fluid flow was observed to be near the maximum for this design of electrode array.

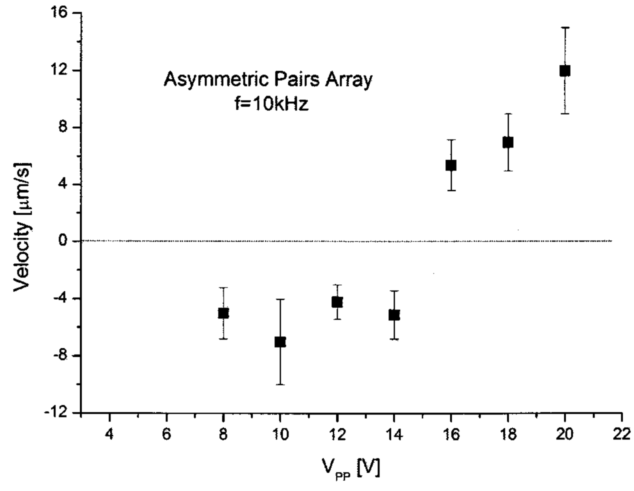

Figure 3.8: Horizontal velocity at a height of 210 μm as a function of voltage for a frequency of 10 kHz (asymmetric pairs array).

Similar to Figure 3.6, the electrolyte moves across the electrodes in one direction at low voltages and changes direction at a transition voltage of approximately 15 $\mathrm{V_{pp}}$. At low voltages the net fluid flow direction corresponds to that predicted by linear theory, i.e. from small to large electrode as shown in Figure 1.3b. This is termed normal pumping. At higher voltages the fluid reverses direction, as for the travelling-wave pump. Figure 3.9 shows the experimental fluid pathlines for normal pumping and reverse pumping in each case. The large fluid roll that extends into the bulk in each case has a typical size around 220 μm, that is the spatial periodicity of the array. When the pumping changes to

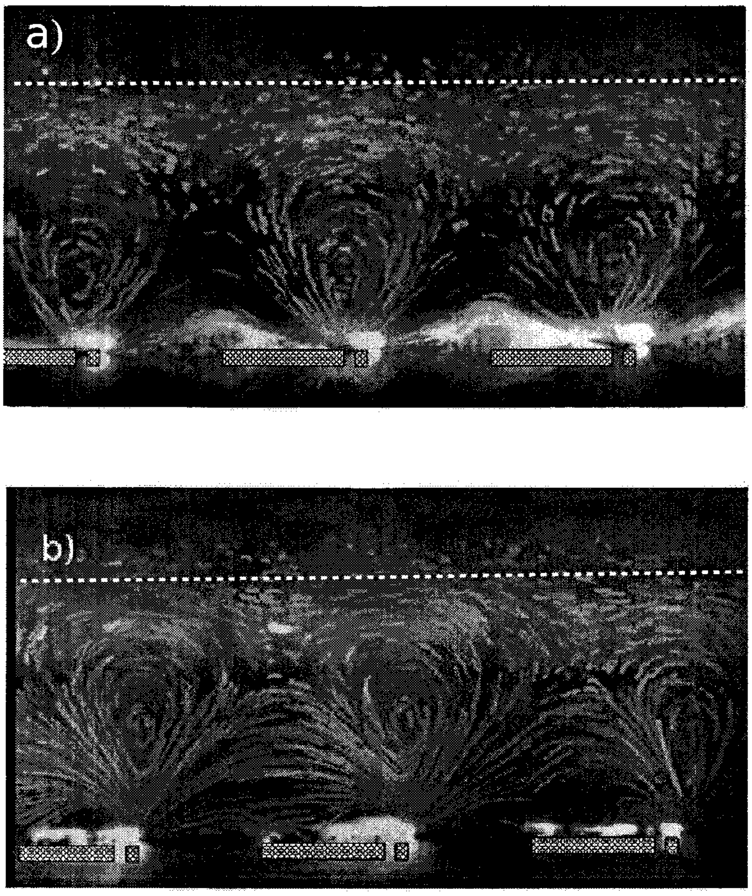

Figure 3.9: Pathlines for the asymmetric array. (a): 10 kHz and 8 $\mathrm{V_{pp}}$. (b): 10 kHz and 18 $\mathrm{V_{pp}}$. The electrodes are drawn in the images. Dashed lines are placed at the height where the fluid velocity was measured.

reverse mode, the rolls over the electrodes change, both in shape and position on the electrodes. The rolls in the reversal mode seem to be slightly shifted to the right.

3.4 Discussion

As mentioned in the introduction, the travelling-wave electrode array is generally employed to move particles using travelling-wave dielectrophoresis (twDEP). We can compare the particle motion due to fluid flow and that due to twDEP motion. Using the theoretical results for the dielectrophoretic force given in the introduction, the horizontal travelling-wave dielectrophoretic velocity at a height $y > 1.5d$ (in water) is given by:

$$v_{twDEP} = 4.35 \times 10^{-8}\mathrm{Im}[\tilde{f}]\frac{a^2V_{pp}^2}{d^3}e^{(\pi/2d)y} \ \ \mathrm{m/s} \tag{3.1}$$

where, a is the particle radius and d the electrode width (in meters). $\mathrm{Im}[\tilde{f}]$ the imaginary part of the Clausius-Mossotti factor. This equation shows that at large distances from the electrode ($y >> d$) the electric field is close to zero. Therefore at the point of observation (140 μm above the electrodes) the twDEP (and DEP) velocities are negligible (smaller than Brownian motion). The fluid velocity measurements are not affected by dielectrophoresis at this height. Even at heights around $1.5d$ the travelling-wave dielectrophoretic motion is negligible. For particles 10 times larger, at 6 $\mathrm{V_{pp}}$ and at a height around d, the dielectrophoretic velocity is less than 30 μm/s. Generally, travelling-wave DEP is observed when particles undergo negative DEP and have a non-zero imaginary component of the dipole. Practically, this occurs at frequencies much greater than 1 kHz. At high frequencies the AC electroosmotic fluid velocities are much lower, so that twDEP dominates.

Comparison of the asymmetric pump and the travelling-wave pump is not simple because the electric field and geometry are different in each case. However, since in this case the spatial periods of both arrays are close ($160\,\mu m$ for the TWEO and $220\,\mu m$ for the ACEO), a fair comparison can be made if the amplitude of the AC signal applied to each pair of the asymmetric array is divided by 2. In effect, each electrode in the TW array is subjected to a signal $V_0cos(\omega t + \varphi)$ while each pair of the asymmetric array has one electrode subjected to a signal $V_0cos(\omega t)$ and the other electrode is grounded. The case of the asymmetric array is equivalent to have one electrode subjected to $(V_0/2)cos(\omega t)$ and the other to $(V_0/2)cos(\omega t+\pi)$ and, therefore, we can consider that each electrode was subjected to a signal of amplitude half the amplitude applied to each pair. The comparison shows that much greater fluid velocities are achieved with the travelling-wave device than with the asymmetric electrode. The experimental pathlines can also be compared. The fluid flow for the travelling-wave device is more uniform, and this can be an advantage in circular chromatographic applications (Debesset *et al.* (2004)). Also, higher voltages are required in the asymmetric array to observe *Reverse Pumping.* The threshold voltage in TWEO was 4 $\mathrm{V_{pp}}$ (Fig. 3.4) while a signal of amplitude larger than 7 $\mathrm{V_{pp}}$ has to be applied to each electrode to observe *Reverse pumping* in the asymmetric array (Fig. 3.8).

Although the normal mode of pumping can be qualitatively explained by the linear (Ramos *et al.* (2005)) and weakly nonlinear (González *et al.*

(2008a)) theories, the reversal of pumping which is seen in both types of devices cannot. This reversal of fluid flow at higher voltages and frequencies has also been observed by Studer *et al.* (2004) and Urbanski *et al.* (2006), who studied the pumping of a platinum asymmetric electrode device. Lastochkin *et al.* (2004) also observed a reversal of flow at higher voltages and frequencies with a pair of planar orthogonal electrodes. Studer *et al.* (2004) found that the maximum velocity for the normal pumping was measured around 1 kHz, and the maximum speed in the reverse motion was found around 50 kHz. This frequency was higher than observed in the present work with titanium arrays. In Studer *et al.* (2004), the transition from normal to reverse pumping was observed increasing the frequency rather than increasing the voltage, as in our case. In recent experiments with platinum asymmetric arrays (Gregersen *et al.* (2007)), a more careful study of the low voltage ($< 1.5\,\mathrm{V_{rms}}$) and low frequency ($< 20\,\mathrm{kHz}$) regime showed unexpected reverse pumping but for ionic concentrations equal or greater to $400\,\mu\mathrm{M}$ and, therefore, different physical origins might be expected for both observations. An important difference between titanium and platinum electrodes is that the former possess an oxide layer that reduces the voltage accross the diffuse layer and prevents Faradaic currents. On the other hand, platinum electrodes are far from the ideal perfectly polarizable electrodes and Faradaic currents could be present even for low voltages (as those in the reverse pumping observed by Gregersen *et al.* (2007).

Chapter 4

Platinum arrays: Experimental characterization

This chapter presents the experimental work with travelling-wave arrays made from platinum. First, fluid velocity measurements on a 20 μm wide platinum electrode array are shown. KCl water solutions with conductivity 1.5 mS/m are used and a similar flow map to figure 3.4 (obtained with a titanium array) is found. Another platinum array with 10 μm wide electrodes is also studied for comparison.

We also show electrical impedance measurements of the system before and after the array has been pumping the electrolyte for a time of five minutes. After the travelling-wave potential was switched off, the impedance of the array was measured as a function of time. The measurements indicate a sharp decrease in the impedance of the system compared with the values prior to application of the signal. Continued monitoring of the impedance showed that the original values were recovered after around 100 s. The electrical current was measured whilst the array was pumping the liquid and transient behaviours in both electrical current and fluid velocity were observed.

The effect of the electrolyte conductivity is also studied. Three different KCl solutions were used with conductivities 1.5, 7.7 and 16.9 mS/m, respectively. As a general trend, it was found that electroosmotic velocity decreased with increasing conductivity. The threshold voltage for reverse pumping was studied and we observed that, for higher conductivities, higher voltages are required in order to observe flow reversal.

For a further characterization of the flow reversal, the influence of the array shape has also been explored. A circular TW array and a straight one within a microfluidic loop have been studied. Low channels ($\sim$ 50 μm high) were fabricated on the arrays in order to evaluate the influence of channel height on flow reversal.

Fluorescent dyes have been used to study the effect of ionic concentration gradients. *Rhodamine 6G* and *Bodipy* have been employed as tracers of positive and negative ions, respectively. *Flourescein* has been used as a pH indicator.

4.1 Experimental details

The microelectrode array consists of a row of 55 coplanar microelectrodes of equal size fabricated on a planar glass wafer using photolithography. Two arrays were studied - array A consisting of 20 μm wide electrodes

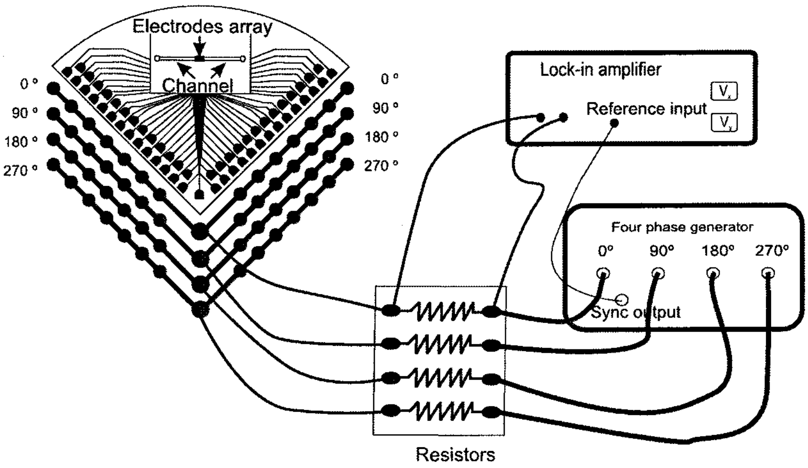

Figure 4.1: Connections for the electrical current measurement. The voltage drop across a resistor is measured by the Lock-in amplifier.

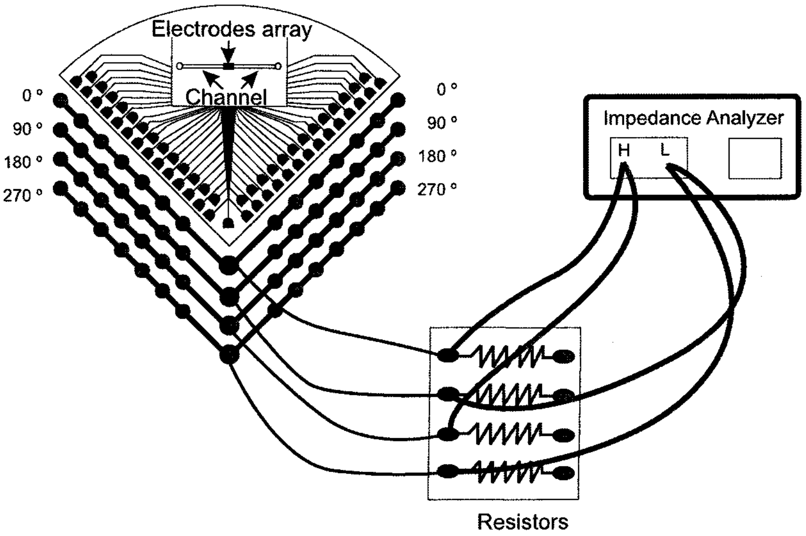

Figure 4.2: Connections for the impedance measurement. Electrodes corresponding to phases 0° and 180° are connected to one wire and those corresponding to 90° and 270° to another.

separated by 20 μm gaps, and array B consisting of 10 μm wide electrodes with 10 μm gaps. The total length of array A is 2.2 mm and of array B 1.1 mm. Microscope coverslips were used to fabricate a fluid channel (approximately 3 cm long) over the microelectrode array with dimension of 700 μm wide by 180 μm high. Ultraviolet adhesive was used to glue the coverslip pieces. The channel was probed to be free of leaks. A 10^{-4} M solution of KCl (conductivity is 1.5 mS/m) was used as the working electrolyte. The end points of the channel were connected to PTFE tubes and thence to a syringe. The electrolyte was renewed after every measurement. Fluorescent latex particles (500 nm diameter) were suspended in the electrolyte and used as flow tracers. An epifluorescence microscope (Nikon Optiphot-100) was used to observe the flow tracers, recorded using a digital camera and video. Fluid velocity measurements were carried out using the Particle Tracking Software (Appendix C).

Electrical current measurements were made by energizing the array with a four-output-signal generator. Current was measured from the voltage drop across four identical resistors (of low resistance - $10\,\Omega$) connected to the device, see Fig. 4.1. The voltage drop was measured using a lock-in amplifier, where the in-phase V_x and out-of-phase V_y signals were measured with respect to the driving signal. The impedance of the array was measured using an Impedance Analyzer, *Agilent (4294A)*. In addition, the impedance of the device was measured before and after application of the travelling-wave signals for pumping. Electrodes corresponding to phases 0^o and 180^o are connected together to the High Output of the Impedance Analyzer, similarly, electrodes corresponding to phases 90^o and 270^o are connected together to the Low Output, see Fig. 4.2. In this way the impedance is measured between neighbouring electrodes and provides a measure of the quasi-equilibrium properties of the liquid before and after the travelling-wave potential is applied.

4.2 Velocity measurements

When an AC voltage is applied to the electrode arrays, the fluid is driven into flow close to the electrode surface. Because the channel is closed with valves at both ends (input and output), the fluid re-circulates and the tracer particles at the top move in the opposite direction to those above the electrodes (see Fig. 4.3). The pump behaviour was characterized as a function of voltage and frequency by measuring the fluid velocity at a height of $120\,\mu$m above the electrodes, which is 2/3 of the channel height. At this point the fluid is moving in the opposite direction to that at the electrode surface and the velocity measurements can be considered representative of the global behaviour of the pump. Figure 4.3 shows the theoretical velocity profile obtained as a consequence of a slip boundary condition at the level of the electrodes and a non-slip at the top of the channel. It is important to point out that the observed velocity profiles could correspond to a fluid flow generated close to the electrodes but not necessarily at the electrode-electrolyte interface. Since the height of the

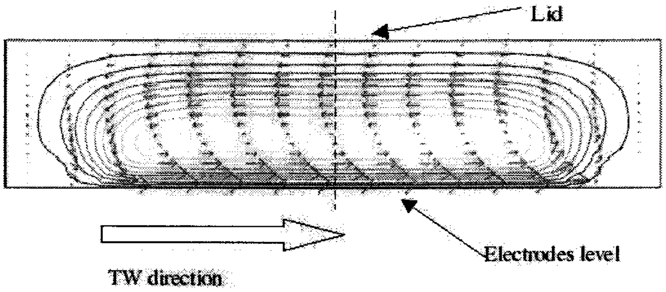

Figure 4.3: Vertical profile of the fluid velocity in a closed channel. The fluid is driven at the level of the electrodes and recirculates. Velocities are measured at a distance 2/3 of the channel height above the electrodes where the velocity has a local maximum.

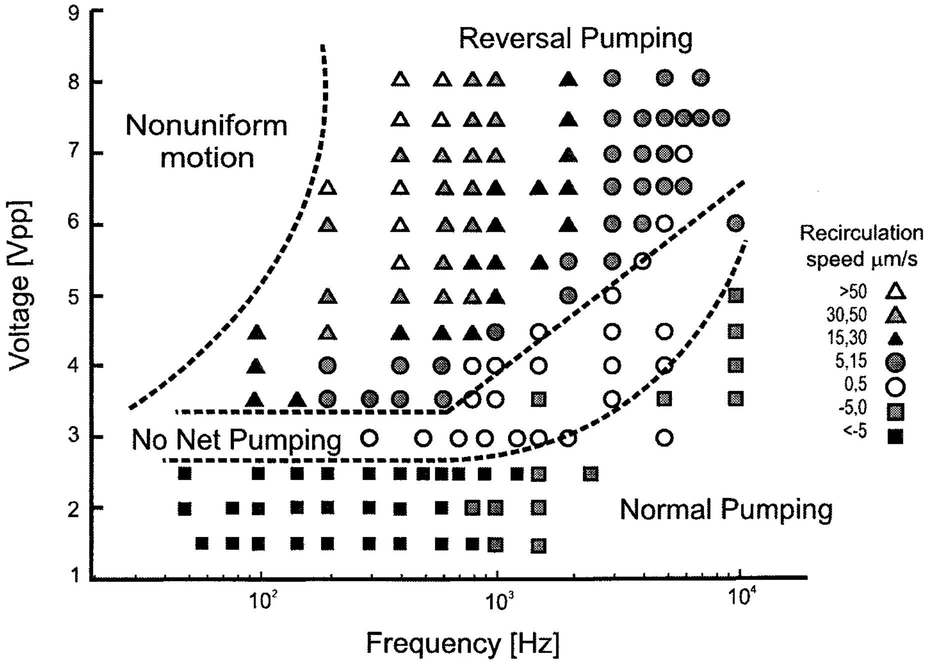

Figure 4.4: Velocity map for the travelling-wave array of 20 μm Pt microelectrodes in the plane voltage versus frequency. Velocities measured at a height of 120 μm above the electrodes (see Fig.4.3). Four different fluid flow behaviour regions can be distinguished.

channel is much greater than the electrode width, forces applied at the electrode surface or forces applied within a region the size of the electrode width would generate similar velocity profiles.

Figure 4.4 shows a 2-D map of the velocity measurements for travelling-wave array A ($20\,\mu$m wide electrodes). Every measurement was taken using the following protocol: new liquid was flushed through the microchannel, the signal generator was switched on and videos of the flow tracers were captured during the next 20 seconds. The measurements were plotted in the voltage versus frequency domain. A negative value of the velocity indicates that the fluid is driven on the electrodes in the direction of the travelling electric field. At low voltages, the fluid is driven in this direction, as expected by the low voltage theory of AC electroosmosis (Cahill *et al.* (2004); Ramos *et al.* (2005)). We refer to this mode of behaviour as *Normal Pumping.* At higher voltages, the fluid is driven in the opposite direction, a mode of behaviour we designate as *Reverse Pumping.* The physical mechanism responsible for this behaviour is not clear at present.

The figure shows four distinguishable regions corresponding to: *normal pumping*, *reverse pumping*, *no net pumping* and *non-uniform motion.* There is a region of voltage where the pumping mechanism changes from normal to reverse pumping. A distinct net flow was not clearly observed in this region, although strong fluid rolls occurred over the electrodes. We designate this region as *No Net Pumping.* At low frequencies and for voltages where the reverse pumping occurs, there appears a region where non-uniform fluid motion is observed. The fluid pattern is fully 3D and the profile of Figure 4.3 is not observed. This region is designated *Non-uniform motion.* Electrolytic bubble generation was observed inside this region for sufficiently high voltage and low frequency. A similar flow map was observed for the $20\,\mu$m wide electrode array of titanium in the previous chapter. However, we note that there are some qualitative differences because for the titanium array: (1) typical voltages for flow reversal were higher; (2) electrolysis occurred at low frequencies before the fluid flow became non-uniform; (3) there was a characteristic frequency of maximum velocity in the *Reverse Pumping* mode.

Figure 4.5 shows the fluid velocity as a function of frequency for array A at different voltages. The fluid flow behaviour strongly depends on frequency. In the *Reverse Pumping* region we do not see any local velocity maximum. As the frequency decreases, the velocity increases until we reach the region of nonuniform motion. In the region of normal motion a maximum absolute velocity seems to be present around 80 Hz. However, the size of the error bars make identification of the maximum rather difficult. In previous experiments using arrays of titanium electrodes (Ramos *et al.* (2005), chapter 3) a velocity maximum was clearly observed. We

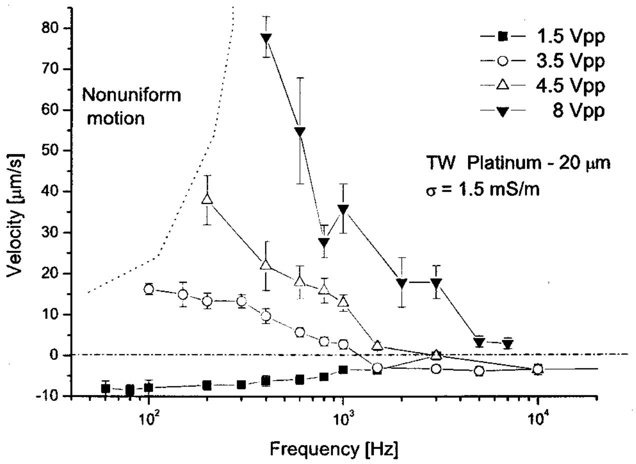

Figure 4.5: Velocity versus frequency for the 20 micron array.

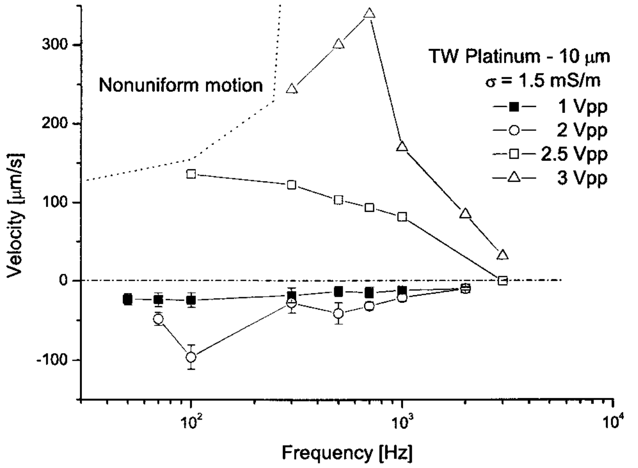

Figure 4.6: Velocity versus frequency for the 10 micron array.

propose two reasons for the different behaviour in normal pumping: (a) Titanium electrodes are known to posses an oxide layer. The effect of this layer is modelled as an extra capacitance in series with the diffuse layer capacitance, and therefore shifts the typical frequency for ACEO to high values. (b) Platinum electrodes are far from ideal perfectly polarizable electrodes, the converse of titanium electrodes. Electrochemical reactions easily occur when platinum electrodes are used and the typical frequency for ACEO is expected to be lower (Ramos *et al.* (2007); Olesen (2006)). In effect, the electrochemical reactions can short-circuit the double layer and, therefore, suppress the electroosmotic velocity. However, at lower frequencies, the diffusion of reactive species limit the Faradaic reactions and the double layer gets charged.

	Ti 20 μm	Pt 20 μm	Pt 10 μm
Threshold Voltage	4 V_{pp}	3.5 V_{pp}	2.5 V_{pp}

Table 4.1: Threshold voltages for reverse pumping for $f \leq 1\,\text{kHz}$. The threshold voltage is defined as the lowest value at which flow reversal is observed.

The same measurements were carried out with travelling-wave array B ($10\,\mu$m wide electrodes). The qualitative behaviour is similar to array A. Reverse pumping is observed at voltages at and above $2.5\,V_{pp}$. Non-uniform flow is observed in the reverse pumping region when the frequency is low. Figure 4.6 shows the fluid velocity as a function of frequency for array B at several voltages. A quantitative difference between array A and B is that the velocities observed for array B were much greater than those observed for array A at the same voltages. This indicates that the velocity is greater for smaller electrodes. In the normal pumping region a maximum in velocity appears at a frequency around 100 Hz. This is different for the reverse pumping where a maximum is found at higher frequencies. Error bars are not plotted; errors are large at velocities larger than $100\,\mu$m/s, and can obscure the maximum in velocity. Furthermore, since the apparent maximum appears close to the non-uniform motion region, the maximum might not be significant because the flow is not uniform at these frequencies.

The reproducibility of the velocity measurements is influenced by effects such as aging of the electrodes, see Gregersen *et al.* (2007). Nevertheless, the threshold voltage for the appearance of flow reversal is very reproducible. The threshold voltage was observed to be more or less independent of frequency below 1 kHz, and increased with frequency above. The threshold voltage, deemed to be the lowest value at which flow reversal is clearly observed, is shown in the following table for three cases: the titanium 20 μm wide electrode array and the two platinum electrode arrays. The values shown in table B.1 are for frequencies below 1 kHz.

4.3 Electrical measurements

4.3.1 Electrical impedance

Measurements of the impedance of the *electrode-electrolyte* system were carried out by connecting the electrodes corresponding to phases 0° and 180° to one wire and those corresponding to 90° and 270° to another, see Fig. 4.2. A frequency sweep is performed for every measurement. The excitation voltage is kept low enough ($100\,\mathrm{mV_{rms}}$) so that the liquid properties are not altered. Fig. 4.7(a) and 4.7(b) show impedance modulus and phase for array B before the travelling-wave potential is applied (full lines). This impedance represents a reference state for the electrical response of the electrode-electrolyte system. Each time the liquid was renewed these impedance values were reproduced. The impedance was also measured after the array was used with specific travelling-wave signals for five minutes: The impedance at low frequencies ($< 1\,\mathrm{kHz}$) was found to be much smaller than that of the reference state while at high frequencies ($>100\,\mathrm{kHz}$) it was only slightly smaller. Dotted lines in Fig. 4.7(a) and 4.7(b) show the impedance modulus and phase measured immediately after removing the travelling-wave potential ($3\,V_{pp}$ and $100\,\mathrm{Hz}$) after it had been applied for 5 min. Note that the time required for a frequency sweep is much shorter than the typical time of variation of the impedance (tens of seconds). This means that the quasi-equilibrium electrical properties of the system can be measured with time. It was observed that the fluid stopped immediately after the TW signal was switched off - the fluorescent particles did not move. Therefore, fluid flow does not occur during the impedance measurements and therefore the impedance changes can not be attributed to movement of the fluid.

There is the possibility that a temperature increase due to Joule heating could affect the impedance measurements. The total heat dissipation per unit time is given by the volume integral of $\sigma\mathbf{E}^2$. At steady state, the heat flux is the value of this integral per unit surface area $k \mid \nabla T \mid \sim \sigma\mathbf{E}^2 l$, where k is the electrolyte thermal conductivity, l is the typical length for the electric field - of the order of the electrode width. If the gradient of temperature is written as $\nabla T \sim \Delta T/H$, H being the height of the channel, an estimation of the temperature increment is given by $\Delta T \sim \sigma V^2 H/kl$ with $E \sim V/l$. For the parameters in the experiments ($\sigma = 1.5\,\mathrm{mS/m}$, $H = 200\,\mu\mathrm{m}$, $l = 10\,\mu\mathrm{m}$, k=0.56 W/m·K) and a typical voltage amplitude of 2 volts, we estimate $\Delta T \sim 0.2\,\mathrm{K}$. This small

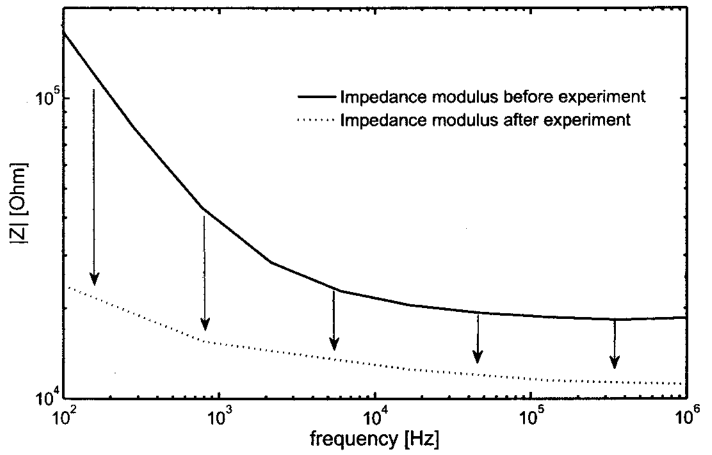

(a) Impedance modulus versus frequency. The measurements after the TW signal show a strong decrease at low frequencies.

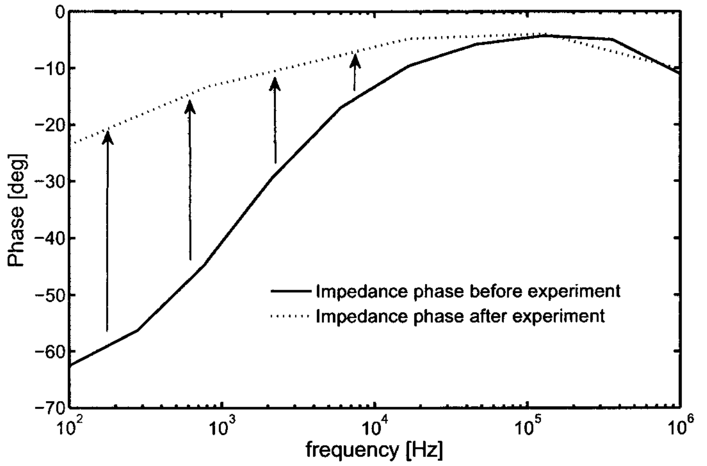

(b) Impedance phase versus frequency. The measurements after the TW signal show that the ratio of in-phase to out-of-phase currents increased at low frequencies.

Figure 4.7: Impedance measurements I: The impedance was measured before any signal was applied (full lines) and immediately after cessation of a TW signal of 3 V_{pp} and 100 Hz that had been applied for five minutes (dotted lines).

change in temperature can not account for the very significant changes in impedance that were observed.

Fig. 4.8 shows the impedance modulus and phase at discrete frequencies (100 Hz, 800 Hz, 17.6 kHz, 129.2 kHz, 1 MHz) versus time for array B

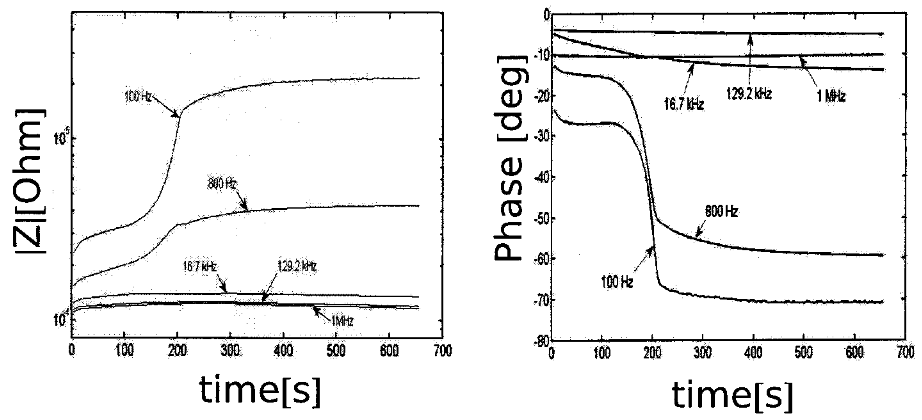

(a) Impedance modulus and phase versus time. The impedance recovers the reference value after ~200 s. All electrodes connected (55)

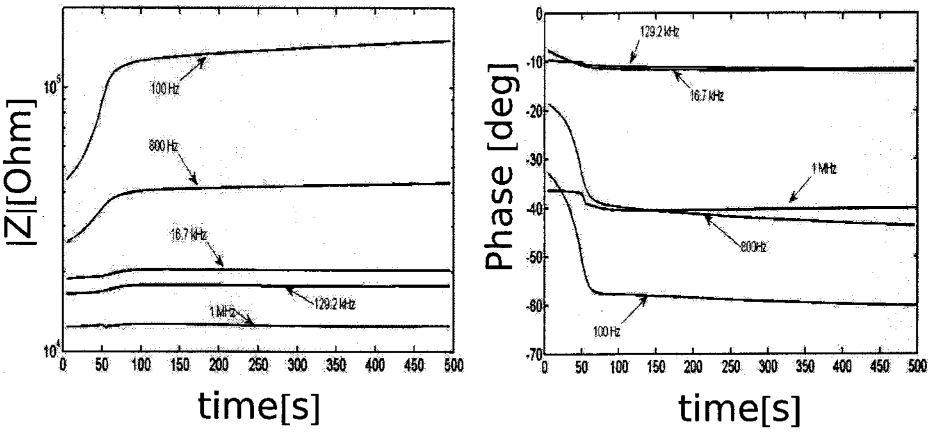

(b) Impedance modulus and phase versus time.The impedance recovers the reference value after ~ 50 s. Half of the electrodes connected (27)

Figure 4.8: Impedance measurements II: Impedance at several frequencies versus time for two different array lengths. The impedance was measured after cessation of a TW signal of 3 V_{pp} and 100 Hz that had been applied for five minutes.

after a TW signal (3 V_{pp} and 100 Hz) was applied for five minutes. Figs. 4.8(a) show measurements where all electrodes (55) were connected, and Figs. 4.8(b) show measurements where only half of the electrodes are connected (27). Note that, according to Fig. 4.6, a non-uniform fluid motion is expected with this signal. It is observed that the decrease in the impedance at 100 Hz is very large, and quickly increases during the first 200 s, then slowly approaches the reference values i.e. the impedance value before the TW signal was applied. At 800 Hz the initial impedance decrement is also very clear while at higher frequencies the decrease is not so strong (on a log-scale), although it is present. The impedance phase changes are also very clear. The phase decrease is large at low frequencies, indicating that the ratio of in-phase to out-of-phase currents increases. These impedance observations mean that changes in the liquid properties are occurring. They also indicate that these changes are greatest near the electrodes. In effect, the impedance at low frequencies depends mainly on the properties of the solid-liquid interface and at higher frequencies the bulk properties of the liquid dominate the impedance. For very high frequencies ($> 1\,\mathrm{MHz}$) the properties of the entire system (including wires, connections, glass...) governs for the impedance.

Fig. 4.8(b) show the impedance versus time when only half of the electrodes are connected (27 electrodes vs. 55), so that the array in this experiment is half the length of the previous measurements. There again appears a strong decrease in the impedance at low frequencies but the recovery to the reference value is faster. Because the time for recovery of the impedance is given by the time for the species to diffuse to produce an homogeneous liquid, a shorter array should recover more rapidly. The microfluidic channel is much longer than the electrode array, see Fig. 4.1. This means that on both sides of the array there is a "reservoir" of fresh liquid. After switching off the signal, we expect to have complete homogenisation when there is enough time for the liquid from the sides to reach the middle. Therefore a faster recovery is expected for the shorter array. The typical time for a given chemical species to diffuse a length L is $t \sim L^2/D$, where D is the diffusion coefficient of the species. The rapid increment of the impedance that was previously observed (within 200 s), is now observed during the first 50 s. This typical time for recovery is roughly four times shorter when the array is half the length. The diffusion coefficient can be estimated as $D \sim (1\,\mathrm{mm})^2/(200\,\mathrm{s}) = 5\times10^{-9}\,\mathrm{m}^2/\mathrm{s}$ which is typical of ionic species in water, supporting this assumption.

Fig. 4.9(a) shows the impedance modulus versus time after a signal of $3\,\mathrm{V_{pp}}$ and 1 kHz (*Reverse pumping* region) was applied for five minutes. The decrease in impedance is also very clear at low frequencies, but not as strong as found for $3\,\mathrm{V_{pp}}$ and 100 Hz, the region corresponding to *non-uniform motion.* Fig. 4.9(b) shows the impedance versus time after a signal of $1.5\,\mathrm{V_{pp}}$ and 100 Hz was applied for five minutes. The array is operating in the *normal pumping* region and changes in the impedance are still appreciable despite the fact that the voltage is substantially lower than the threshold voltage for this array. It could be inferred that changes in impedance are only observed for voltages at or

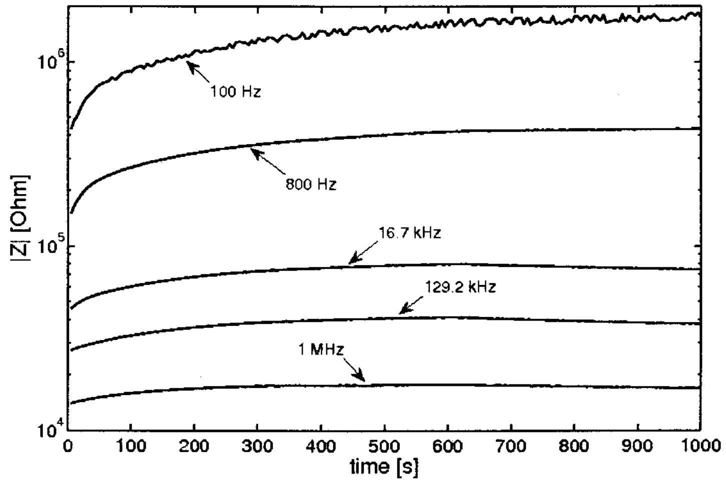

(a) Impedance modulus versus time after 3 V_{pp} 1 kHz

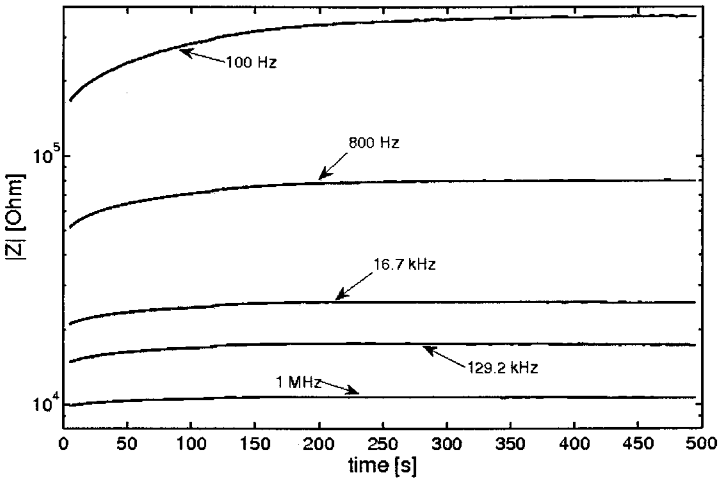

(b) Impedance modulus versus time after 1.5 V_{pp} 100 Hz

Figure 4.9: Impedance measurements III: Impedance at several frequencies versus time. The impedance was measured after cessation of two different TW signals: (a) 3 V_{pp} 1 kHz applied for five minutes and (b) 1.5 V_{pp} 100 Hz applied for five minutes.

above the threshold. This is not the case, and figure 4.9(b) shows that the impedance also changes at signals corresponding to the *Normal Pumping mode.* In general, the changes in impedance increase with increasing voltage and/or decreasing frequency. The decrement in the impedance at frequencies greater than 10 kHz indicates that the bulk conductivity is increasing. This increase means either an increase in ionic strength or an exchange of high- mobility species for lower mobility species or a combination of the two (most likely). We expect the conductivity increase to be stronger near the electrodes since electrochemical reactions occur there. The strong decrement of impedance modulus and the change in the impedance phase for lower frequencies seems to indicate that either the charge transfer resistance has strongly decreased or the surface capacitance has increased. These changes can be driven by an increase in ionic strength and/or an increment in reactive high mobility species such as H^+ or OH^-.

From the net change in liquid properties, we infer that electrochemical reactions at the electrodes are not symmetrical with time. The rectifying properties of electrode-electrolyte interfaces is a well known phenomenon (O'dea *et al.* (1994)) and could be related to this observation. In Geddes *et al.* (1984), current rectification was measured above a certain threshold current density - the threshold current increased with frequency. The estimated current densities in our experiments are of the same order of magnitude as these threshold current densities.

4.3.2 Current measurements. Transient measurements

The electrical current was measured when the travelling-wave signal was applied to array A as indicated in the experimental section - Fig. 4.2. The actual current was measured when the TW signal is applied, a completely different measurement to that described in the previous section. A linear behaviour in the current-voltage characteristics was found at low voltage (below $1.5\,V_{pp}$). At higher voltages, non-linearities appear and the current increase with voltage was faster than for the linear case. This is observed as a decrease in the apparent impedance. Other researchers working with high sinusoidal currents have observed that the apparent impedance decreases as the current amplitude increases (Geddes *et al.* (1984); Schwan (1992)). More remarkably, we measured a time-dependent electrical current amplitude, i.e. the current was oscillating at the driving frequency $I(t) = I_0 \cos(\omega t)$ with an amplitude I_0 that changed slowly with time. The characteristic time for this slow variation was of the order of minutes, very much greater than the period of the AC signal. It is worth to mention that we have also observed the current amplitude changing with time in array B. In Fig. 4.10(a), the current amplitudes are shown at several voltages versus time for array A at a frequency of 100 Hz. Fig 4.10(b) shows similar data at 1 kHz. These

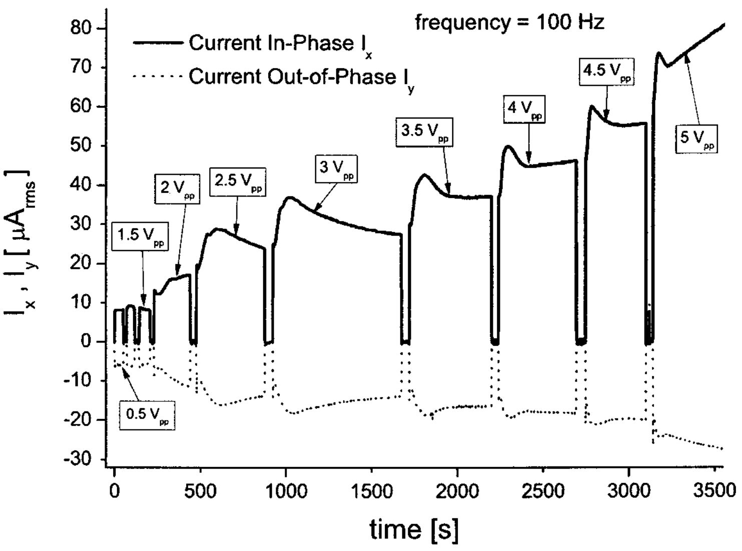

(a) Electrical current vs time at 100 Hz

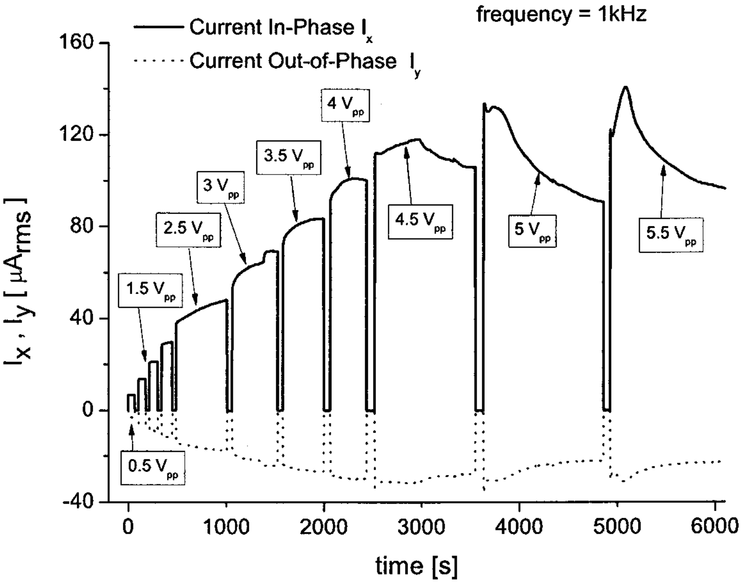

(b) Electrical current vs time at 1 kHz

Figure 4.10: Electrical current versus time during application of TW signals of different amplitudes.

measurements were performed as follows: starting from 0.5 V_{pp}, the current amplitude versus time is measured with a lock-in amplifier. The

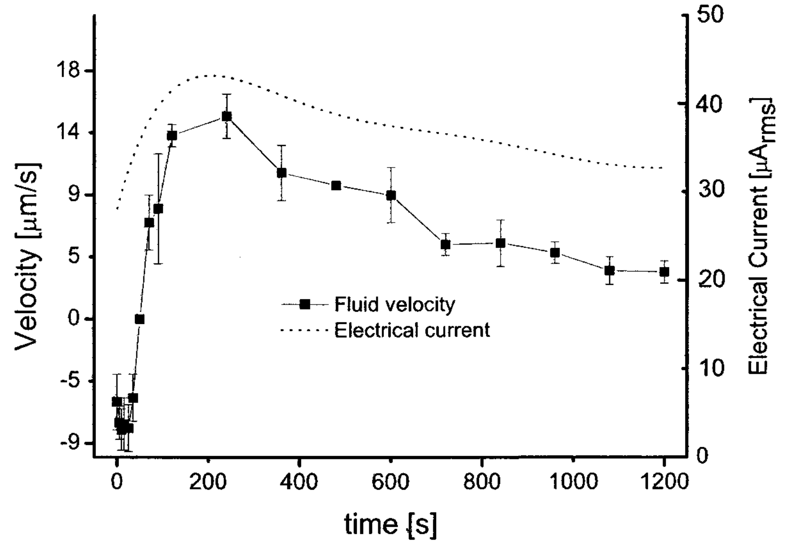

(a) Velocity and electrical current vs time at 3 V_{pp} and 400 Hz

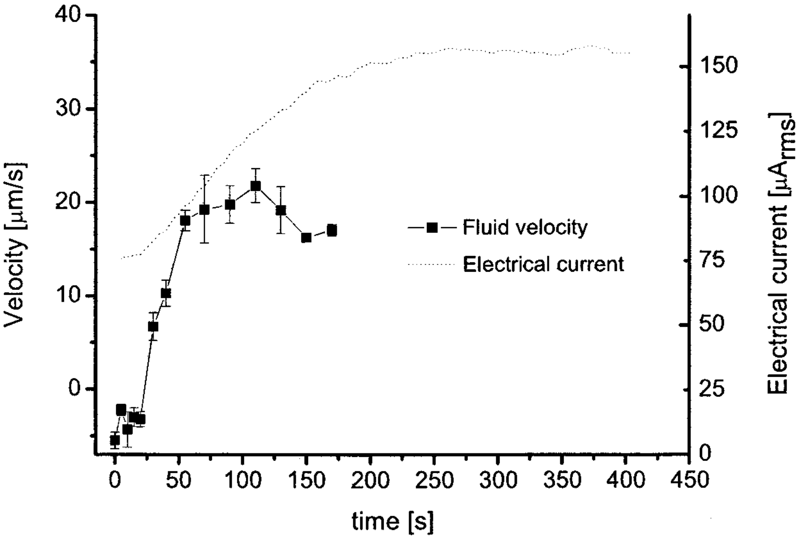

(b) Velocity and electrical current vs time at 3 V_{pp} and 700 Hz

Figure 4.11: Electrical current and fluid velocity versus time during application of a TW signal.

lock-in samples data until the current reaches a stationary value, then the signal is switched off and new liquid is flushed through the channel. The voltage is increased to a stationary value. Then, the signal is switched off and new liquid is flushed through the channel. The voltage is increased in 0.5 V_{pp} increments, the signal switched back on and the lock-in measures the current amplitude until a new stationary value is reached. Currents at 100 Hz show peaks that are typical of Faradaic currents. At 1 kHz these peaks were not clearly observed. Note that the capacitive current increases with frequency so the total current is expected to be greater at 1 kHz and any Faradaic currents could be masked by capacitive currents.

Observations of the flow behaviour for signals corresponding to the *no net pumping* region of Fig. 4.4 are shown in the next two figures. For array A at a voltage of 3 V_{pp} and at 400 Hz, we observed that the fluid started to move slowly in the *Normal pumping mode* and, after around two minutes, the direction was reversed, see Fig. 4.11(a). Measurements of the current amplitude are also plotted and both velocity and current are strongly correlated. Fig. 4.11(b) shows the same transient behaviour at 3 V_{pp} and 700 Hz. At this frequency the current amplitude is roughly the double than at 400 Hz and Faradaic currents are likely to be masked by capacitive currents. The inversion of the net fluid flow was reproducible if new liquid was flushed through the channels. If after applying any of these signals the liquid was not changed, the fluid started to move in the *Reverse Pumping mode*, indicating some hysteresis. Notice that this reversal of flow in time was not observed for signals outside the *no net pumping region.*

4.4 Effect of the electrolyte conductivity

Three different concentrations of KCl in water were used in order to study the effect of the conductivity on the pumping of electrolytes with travelling-wave arrays. For these experiments, a square PDMS chamber was constructed around the 20 μm wide platinum electrode array. The chamber was filled with the electrolyte and covered with a microscope coverslip. The height of the chamber was 360 μm. The measurements at low voltage were done at a constant signal amplitude and changing the frequency. For each voltage amplitude, the liquid was renewed. Note that this procedure is different from that in section 4.2, where new liquid was used for every single velocity measurement.[1]

---

[1] The experiments in this section were made in collaboration with H. Yang from Harbin Institute of Technology (P.R. China).

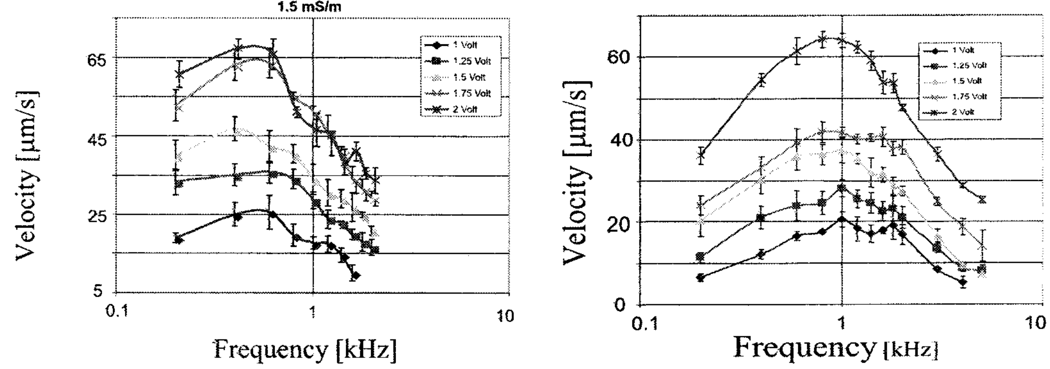

(a) Electrolyte conductivity 1.5 mS/m

(b) Electrolyte conductivity 7.7 mS/m

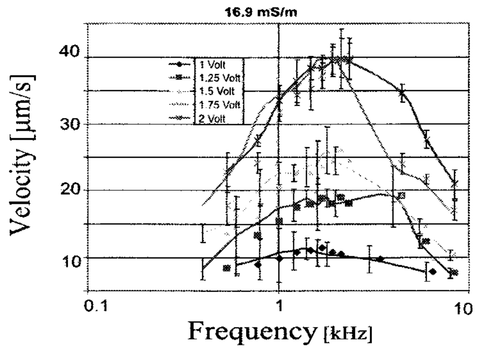

(c) Electrolyte conductivity 16.9 mS/m

Figure 4.12: Velocity versus frequency for different applied voltages at three different conductivities.

4.4.1 Low voltage measurements

Fluid velocities were measured for TW signals of low amplitude ($\leq 2\,\mathrm{V_{pp}}$). The measuring point was at 2/3 of the total height above the surface of the electrodes (240 μm). Figures 4.12(a), 4.12(b) and 4.12(c) show velocity versus frequency plots for different applied voltages, and correspond, respectively, to electrolyte with conductivity 1.5 mS/m, 7.7 mS/m and 16.9 mS/m. In these figures, we can see that the typical frequency increases with increasing conductivity. The velocity as a function of frequency has a bell shape with a maximum at a frequency that scales with the reciprocal of the double-layer charging time, $\omega_{max} = \sigma\lambda_D/\varepsilon l$. We have taken the electrode width as the typical system length l. The experiments follow the qualitative explanation given in section 1.3.

Figures 4.13(a)-4.13(d) show velocity-versus-frequency plots for the three different conductivities, and correspond, respectively, to applied

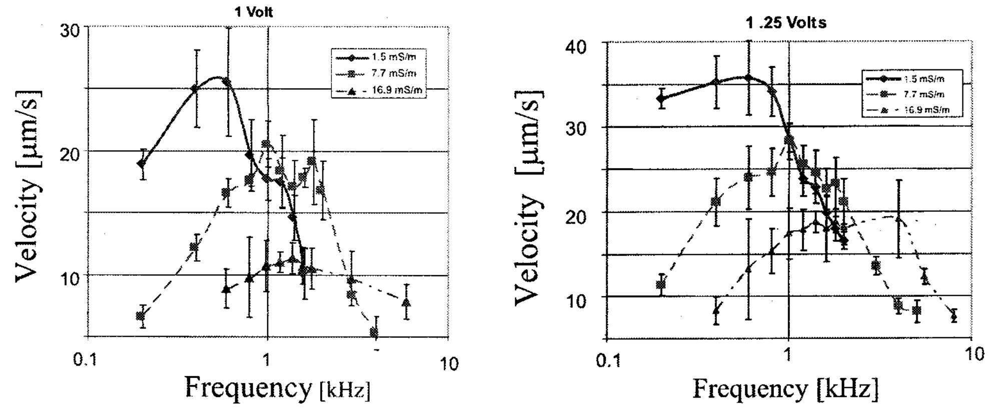

(a) Signal amplitude 1 V_{pp} (b) Signal amplitude 1.25 V_{pp}

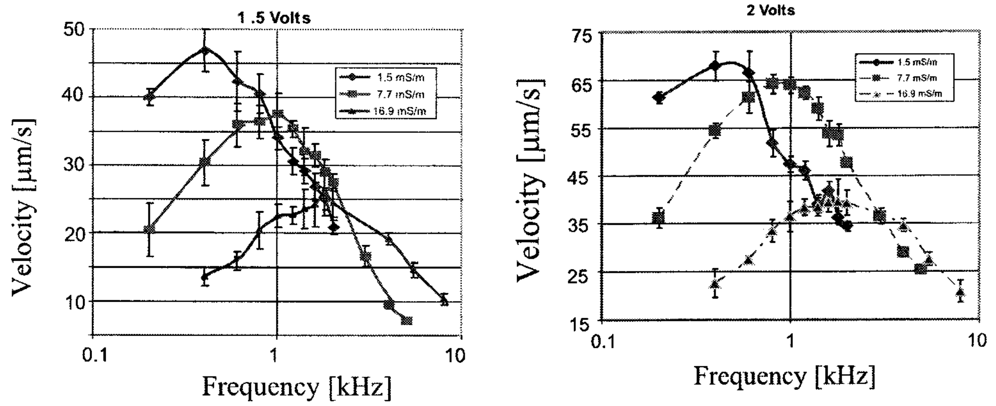

(c) Signal amplitude 1.5 V_{pp} (d) Signal amplitude 2 V_{pp}

Figure 4.13: Velocity versus frequency for different electrolyte conductivities.

voltages of 1, 1.25, 1.5 and 2 V_{pp}. It can be seen that the maximum velocity decreases with increasing conductivity. The AC electroosmosis experiments with a single pair of electrodes also showed this trend (Green *et al.* (2000a, 2002a)). The electrode behaviour is more similar to the case of perfectly polarizable than in the measurements of section 4.2, where the liquid was continuously renewed. Possibly, the difference in the experimental protocol influenced the velocity values.

4.4.2 Threshold voltage for flow reversal

For each electrolyte conductivity, the amplitude of the TW signal was increased in order to check for the apperance of flow reversal. The frequency was kept constant and around the value for maximum velocity for each conductivity. New liquid was used for every value of the signal amplitude. It was found that the fluid flow reversed for the three KCl conductivities and that the minimum threshold voltage increased with ionic strength: it is 3 Vpp for 1.5 mS/m, 4.5 Vpp for 7.7 mS/m and 5.5 Vpp for 16.9 mS/m.

4.5 Array geometry and channel height influence

In table B.1, we showed the threshold voltage for reverse pumping for three different travelling-wave arrays and a liquid conductivity of 1.5 mS/m. One device was made from titanium, with 20 μm wide electrodes, the other two were platinum with 10 μm and 20 μm wide electrodes. The threshold voltage was found to depend both on the size and the metal of the electrodes. The three electrode arrays were straight and in each case the height of the channel was 200 μm, much larger than the size of the electrodes. To investigate the influence of channel height, we fabricated two arrays made from platinum with 20 μm wide electrodes. One electrode array was straight (consisting of 50 electrodes) and the other was circular (consisting of 400 electrodes).

For pumping experiments, the electrode array was covered with a channel made from polymer as shown in figure 4.14. The width of the channel was 450 μm and the height is 50 μm. The channel formed a circular loop over the electrodes with inlet and outlet ports for loading. Two different input and output channels were used for injecting fluorescent beads used as tracer particles. The complete channel was filled with electrolyte while the fluorescent beads were introduced into a small region for observation of flow. A similar method was described by Studer *et al.* (2004). For voltages below 3.5 V_{pp} (the threshold previously found for this array) and frequencies of hundreds of Hertz, it was observed that the fluid was pumped in the normal direction, as expected from previous results. At larger voltages the fluid velocity was zero, even though flow reversal was expected. Bubbles appeared for a voltage amplitude of 8 V_{pp}. When the frequency was increased to 10 kHz, flow reversal was observed over an amplitude range of 6 V_{pp} up to 16 V_{pp} (the maximum we applied). In analogous experiments with asymmetric arrays of platinum electrodes the channel height was 22 μm (Studer *et al.* (2004)), very close to the size of the wider electrode and flow reversal was also found at higher frequencies than for normal flow. Flow reversal at higher frequen-

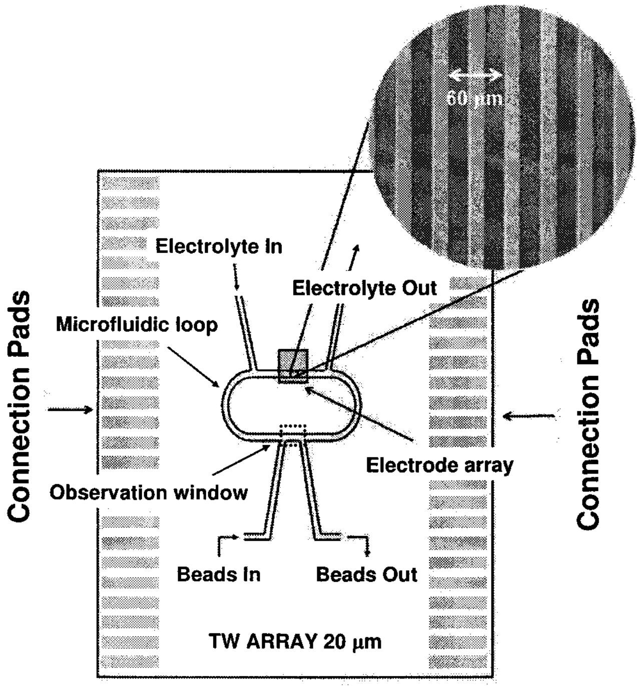

Figure 4.14: Microfluidic loop with a travelling-wave microelectrode array. A micrograph of the electrodes is included; the bright stripes there correspond to the electrodes.

cies for the asymmetric array may have a different physical origin than for the travelling-wave system; nevertheless we cannot discard the possible influence of the channel height for the asymmetric electrode structures. For example, in chapter 3 we found flow reversal with asymmetric arrays of titanium electrodes for increasing voltage rather than frequency for a channel height larger than the electrode size (260 μm channel height against 100 μm electrode width).

Fig. 4.15 shows the experimental layout for the circular travelling-wave array. Two circular channels 1 mm wide were fabricated with PDMS (polydimethilsiloxane): one channel was 1 mm height and the other was 45 μm. They were placed on top of the circular travelling-wave array and filled with the electrolyte containing fluorescent beads. In the case of the tall channel (1 mm), fluid behaviour was as expected for normal pumping for an applied signal of hundreds of Hertz and an amplitude below the threshold voltage (3.5 V_{pp}). *Reverse pumping* was observed at amplitudes above this threshold. In experiments with the shallow channel (45 μm) *normal pumping* was observed at voltages below the threshold but no net pumping was observed above. When higher frequencies were

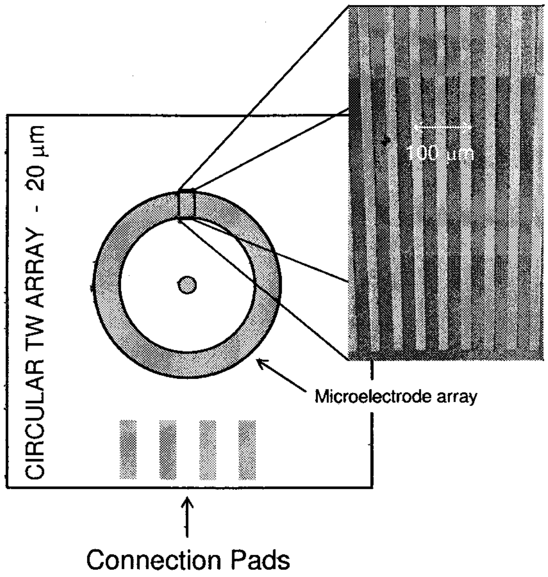

Figure 4.15: Circular travelling-wave microelectrode array. A micrograph of the electrodes is included.

applied (10 kHz), reverse pumping was clearly observed for a voltage amplitude of 10 V_{pp}. The results with the circular array are similar to those with the straight one.

End-effects due to the finite size of a TW array might have some influence on the fluid velocity; fresh liquid enters the array at one end. However, this effect is probably not significant, since for the circular array, *flow reversal* was observed for the same applied voltage and frequency as for the straight array. On the other hand, channel height was found to have a major influence on the flow reversal. *Flow reversal* was observed at higher frequencies and voltages for a channel height of 50 μm, much larger than the Debye length of the electrolyte ($\sim$ 30 nm). Therefore, if the forces generating the motion are confined to the diffuse layer, a 50 μm high channel should have no influence. This seems to indicate that forces beyond the Debye length are responsible for *flow reversal.*

4.6 Fluorescent dyes

Fluorescent dyes were used to study the electrolyte behaviour. We used three different dyes: *Rhodamine 6G* (Sigma-Aldrich), *Bodipy 492/515 disulfonate* (Invitrogen) and *Fluorescein* (Riedel de Häen). *Rhodamine*

6G dissociates completely in water to give a single positively charged ion. *Bodipy* is divalent and dissociates completely to give a negatively charged molecule in water with two charges. *Fluorescein* is weakly acidic: the molecule partially dissolves in water, giving a negatively charged molecule and a free proton. The equilibrium constant between the dissociated and non-dissociated forms of the molecule is pKa = 6.4. Because the dissociated form is fluorescent, changing the pH changes the degree of ionisation of the molecule and therefore the fluorescence intensity.

Fluorescein has been used for detecting and measuring pH gradients created by electrochemical reactions over microelectrode arrays (Fiedler *et al.* (1995)). *Bodipy* and *Rhodamine 6G* have been used as ion tracers for determining the polarization of the ionic concentration in porous glass beads (Leinweber & Tallarek (2004)). *Bodipy* is an anionic tracer and by monitoring changes in the fluorescence profile, changes in the concentration of negative ions can be deduced. *Rhodamine 6G* plays the same role but for positive ions. The fluorescence profile was measured at different electric field strengths - the concentration fields were then estimated. In another publication (Leinweber & Tallarek (2005)), the two dyes were used for tracing ionic concentrations and the observed fluid motion was described as *induced charge electroosmosis*. *Bodipy* and *Rhodamine 6G* have also been used to trace electrolyte concentration over floating electrodes within a microchannel (Leinweber *et al.* (2006)).

Dyes were prepared at a concentration of 10^{-5} M, maintaining the ion concentration at least 1 order of magnitude below the ionic strength of the electrolyte (KCl 10^{-4} M). The electrolyte conductivity is 1.5 mS/m and did not noticeably change after the addition of the fluorescent dyes.

We first analyzed the behaviour of the fluorescent dyes in a simple geometry: two parallel planar electrodes, Fig. 4.16. Two platinum plates were placed as shown in the figure. The plates are 100 μm thick, with a separation between the two of $G = 400\,\mu$m. The plates are stuck to glass slides with double-sided sticky tape. The gap between the plates was filled with the electrolyte (KCl 10^{-4} M) containing one of the fluorescent dyes. The device was placed under the microscope objective and connected to a signal generator.

Prior to the application of a signal a homogeneous fluorescence intensity was observed. When a DC voltage of a few volts was applied, the fluorescence intensity near both electrodes changed. When *Bodipy* and *Rhodamine* were used, the electrolyte near the positive electrode became

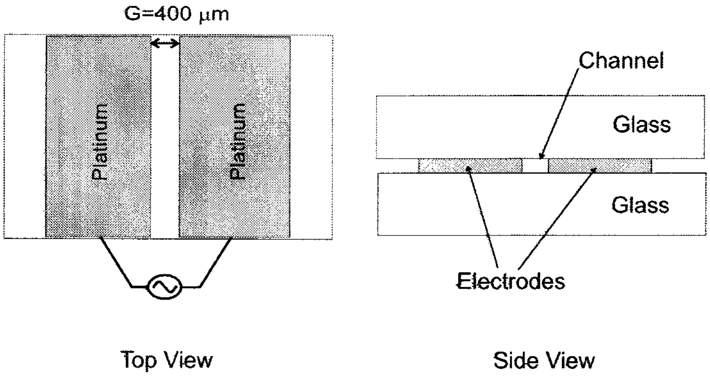

Figure 4.16: Platinum electrodes in a simple geometry for the study of the fluorescent dyes

brighter, while the electrolyte near the negative electrode became darker than the average brightness. On the other hand, *Fluorescein* was brighter near the positive electrode. For AC voltages, the fluorescence intensity oscillated from one electrode to the other at the same frequency as the applied voltage. Again, *Bodipy* and *Rhodamine* were brighter near the positive electrode, while *Fluorescein* became darker near that electrode. This behaviour for all three fluorescent dyes was confirmed for both DC and AC signals at frequencies low enough to allow the fluorescence intensity oscillations to be followed by eye ($f \leq 10\,\mathrm{Hz}$).

Fig. 4.17 shows the fluorescence emission from an electrolyte containing *Bodipy* at a certain instant when the pair of electrodes was subjected to an AC potential of 6 $\mathrm{V_{pp}}$ at a frequency of 0.5 Hz. The electrode in the figure was negative and a minimum of fluorescence intensity is observed near that electrode. The intensity profile for a given video-frame was obtained with the aid of *ImageJ* [2]. From the image sequence, a typical penetration length for the fluorescence oscillations was measured. This distance can be considered a measurement of the diffusion length, assuming that the fluorescent dye is a measure of the ion concentrations. Measurements were repeated for different frequencies and the data is shown in Fig. 4.18. The experiment was also carried out for a signal amplitude of 10 $\mathrm{V_{pp}}$, giving the same measurements of diffusion length. The diffusion length δ is expected to be proportional to the square root of the diffusion coefficient and decrease with the square root of frequency $\delta = \sqrt{D/\omega}$. The experimental data were fitted to a power law model $\delta = A \cdot f^p$. The fitting parameter p result is 0.56 ± 0.04, which matches the expected theoretical value of 0.5. The diffusion coefficient can be

---

[2] ImageJ - http://rsb.info.nih.gov/ij/

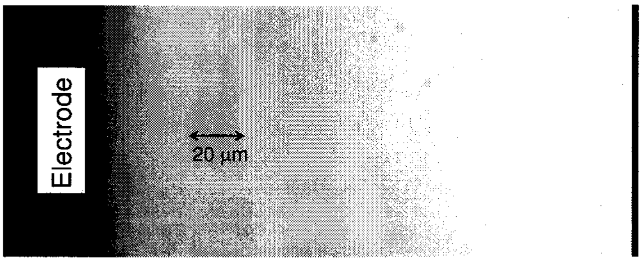

Figure 4.17: Fluorescence intensity of *Bodipy* for an applied signal of 6 V_{pp} and 0.5 Hz. The electrode in the figure was negative at that moment.

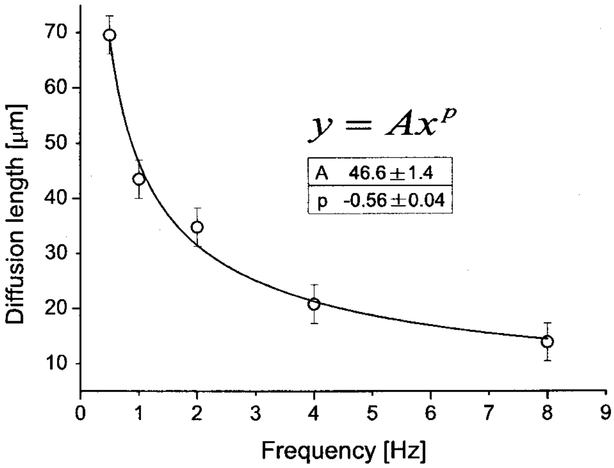

Figure 4.18: Diffusion length of *Bodipy* versus frequency. The amplitude of the signal was 6 V_{pp}.

calculated from the parameter A, giving $D = 1.36 \cdot 10^{-9}$ m^2/s, which is typical for the diffusion coefficient of ionic species, ranging between $0.6 \cdot 10^{-9}$ and $2 \cdot 10^{-9}\, m^2/s$ (Newman & Thomas-Alyea (2004)).

Lower voltages were required to allow observation of changes in the fluorescence emission of the *Fluorescein* compared with *Bodipy* or *Rhodamine.* For instance, when DC signals were applied, 1 volt was sufficient to observe changes in *Fluorescein* emission. On the other hand, 3 volts were required to observe changes with the others dyes. Since the intensity of the emission of the *Fluorescein* is dependent on the pH of the solution, it is probable that electrolysis of water is responsible for the changes in fluorescence intensity. Water reactions lead to changes in the the local pH value of the electrolyte.

Rhodamine 6G and *Bodipy* map concentrations of positive and negative ions, respectively. Since the two dyes were oscillating in phase, i.e. they both moved to the same electrode, the changes in the fluorescence emission of these two dyes are interpreted as an indication of the changes in the concentration of neutral salt (concentration polarization). This means that the electrolyte remains electroneutral but the ionic strength is higher where the fluorescence is brighter. Concentration polarization may appear as a consequence of Faradaic reactions (Newman & Thomas-Alyea (2004)) and/or the non-linear behaviour of the diffuse layer (Suh & Kang (2008); Bazant *et al.* (2004)). K^+ and Cl^- have almost equal diffusivities and, in this case, the frequency of the oscillation would be 2ω rather than ω for perfectly polarisable electrodes (Suh & Kang (2008); Bazant *et al.* (2004)). Observations with *Fluorescein* showed that Faradaic currents occurred even at lower voltages than those at which concentration polarization was noticeable. Therefore, electrolysis of water would seem to be responsible for changes in pH and changes in ionic concentration.

In summary, the experiments at low frequency in this simple geometry show that:

(1) the pH is lower near the positive electrode - the *Fluorescein* emission decreases there.

(2) the concentration of neutral salt is higher near the positive electrode - both *Bodipy* and *Rhodamine 6G* emission increases there.

Depending on the solution pH, electrolysis of water can occur under the two following scenarios (Trau *et al.* (1997)):

Acidic conditions,

$$3\mathrm{H_2O} \rightarrow 2\mathrm{H_3O^+} + \frac{1}{2}\mathrm{O_2} + 2\mathrm{e^-} \qquad \text{(anode)} \qquad (4.1)$$

$$2\mathrm{H_3O^+} + 2\mathrm{e^-} \rightarrow 2\mathrm{H_2O} + \mathrm{H_2} \qquad \text{(cathode)} \qquad (4.2)$$

while at basic conditions,

$$2\mathrm{OH}^- \rightarrow \mathrm{H_2O} + \frac{1}{2}\mathrm{O_2} + 2\mathrm{e}^- \qquad \text{(anode)} \qquad (4.3)$$

$$2\mathrm{H_2O} + 2\mathrm{e}^- \rightarrow 2\mathrm{OH}^- + \mathrm{H_2} \qquad \text{(cathode)} \qquad (4.4)$$

Electrochemical reactions in which ions are produced lead to an increase in salt concentration while ion consumption leads to salt depletion. This situation is equivalent to the case of an electrical current flowing through semi-permeable membranes (Rubinstein & Zaltzman (2000)). Experiments indicate that the total concentration of ions increases near the electrode where the electrolyte is acidified (anode). This leads to the conclusion that the dominant reaction is that under acidic conditions - the pH decreases due to production of H_3O^+ rather than consumption of OH^-.

Typical frequencies for pumping fluids with microelectrode arrays are higher ($\sim 10^2 - 10^3$ Hz) than those used in this geometry. Nevertheless, these experiments provide an indication of how the charged dyes behave and, by inference, how electrode geometries other than the parallel plates used in this work might behave. Experiments were also performed on travelling-wave electrode arrays. A long microchannel was constructed with glass lid on top of the TW electrode array. The channel dimensions were 200 μm high and 1 mm wide. The behaviour was measured at low frequencies ($<$ 10 Hz) and we found the same behaviour as for the two plates: *Fluorescein* becomes darker near the electrodes at positive potential while *Rhodamine 6 G* becomes brighter. To observe fluid motion, 500 nm diameter fluorescent beads were suspended in the fluid and the electrode array was studied in the reverse pumping mode. When the TW signal was applied, it was found that the *Fluorescein* became darker. The fluorescence intensity decreased first near the electrodes and after a few seconds it was very low in the entire channel. This was observed with platinum and titanium electrodes. This result indicates net production of H^+ with an applied AC signal, implying that Faradaic currents are not symmetric.

To verify that photobleaching was not responsible for this effect, observations were made without the electric field; photobleaching was only noticeable after several minutes. In contrast, the fluorescence diminished immediately after the electric field was applied. The reduction in light intensity indicates that the pH in the solution derceases. Fig. 4.19 shows the fluorescence emission from the edge of a TW array made from titanium (20 μm width and 20 μm spacing). *Fluorescein dye* was used and a

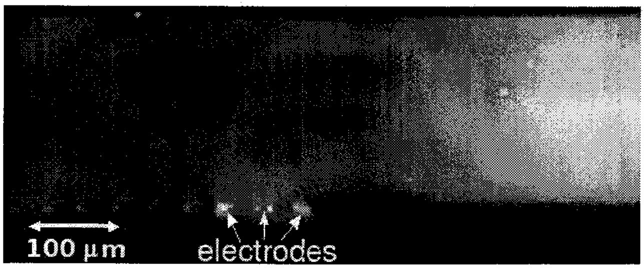

Figure 4.19: *Fluorescein* emission for a signal of 5 V_{pp} at 500 Hz applied to a titanium TW array. The fluorescence decreases along the length of the array indicating a decrement in pH

signal of 5 V_{pp} and 500 Hz was applied (reverse pumping mode). It can be seen that outside the array the fluorescence is unchanged but over the electrodes the electrolyte becomes dark. A sharp change in fluorescence intensity was observed between the electrolyte directly above the electrode array and the electrolyte outside this.

The decrement of pH due to H_3O^+ production is consistent with the impedance measurements, where gradients in concentration of different ionic species were inferred. These gradients can play an important role in fluid flow generation.

4.7 Discussion

The experimental work performed with travelling-wave arrays with electrodes of different metals and sizes seems to confirm that the fluid flow map of the previous chapter represents the general behaviour of these systems. Velocity data were obtained from videos recorded during the 20 seconds after the channel was filled with new liquid and the signal was switched on. We used this protocol to obtain the flow map in Fig. 4.4. The low voltage measurements are not expected to depend on this protocol but at higher voltages this may not be true. In particular, the region of no net pumping is most likely to be affected. As shown in Fig. 4.11, for signals of amplitude 3 V_{pp}, the fluid moves first in the normal direction and after 50-100 seconds, it moves in the reverse direction. The flow map of Fig. 4.4 is interpreted as the "early behaviour" of the micropump and it is a useful description of the phenomena, although not complete since transient behaviour is also present.

Under all experimental circumstances studied, the fluid velocity reverses if the voltage is sufficiently high and the frequency is optimal. However, new qualitative observations are found when platinum electrodes are used. At low frequencies, close to the region of reverse pumping, non-uniform fluid flow is found when the electrode array is observed from the top. Studer *et al.* (2004) also observed local recirculations transverse to the channel when the voltage was increased. The flow patterns indicate that electrohydrodynamic (EHD) instabilities are probably taking place. Gradients in the conductivity of the electrolyte can give rise to such instabilities (Baygents & Baldessari (1998); Chen *et al.* (2005); Lin *et al.* (2004)). EHD instabilities in microchannels with AC driving signals have been recently studied (Boy & Storey (2007)). These authors found a strong frequency dependence when the base state of the fluid electrical conductivity is considered steady. A steady conductivity gradient can appear by thermal or electrochemical effects, as could happen in the present case. Other instabilities such as those studied by Rubinstein and co-workers (Rubinstein & Zaltzman (2000)) may appear at high current densities. They are associated to depletion of electrolyte near the interfaces. The impedance measurements at low frequencies show a strong decrease, particularly strong after applying signals corresponding to the *non uniform motion* region. This supports the assumption that EHD instabilities can occur since, as stated above, the liquid properties are mainly changing near the electrodes and gradients in conductivity (i.e. ion concentration) should appear. Nevertheless, changes in the electrolyte impedance are clear after applying the travelling potential even for signals corresponding to the *normal pumping* region.

The observations with fluorescent dyes show that the solution becomes acidic due to electrochemical reactions in which ions are produced (increase of salt concentration). This is in accordance with the impedance measurements where we found that the conductivity near the electrodes increased. The changes in liquid properties are probably due to water reactions. Interestingly, fluid velocity observations with DI water as the working fluid were also carried out and reverse pumping was found at threshold voltages around those for KCl solutions with $\sigma = 1.5\,\mathrm{mS/m}$.

In Lastochkin *et al.* (2004), the authors demonstrated AC electroosmotic fluid flow and observed reversal of the movement as the voltage increased. They attributed the flow reversal to a "Faradaic charging" mechanism - Faradaic currents would generate net charge on the liquid side of the interface with the same sign as the electrode charge. A net electrical force on the fluid would appear which is opposite to that predicted by ACEO theory. This view of Faradaic charging is also present in recent work on DC-biased AC electroosmosis (Wu (2006)). We argue that this mechanism contradicts the assumption of the electroneutrality of electrolytes at frequencies below the *charge relaxation frequency*, because counterions are not considered in this view. Gauss' law shows that the liquid bulk is quasi-electroneutral on the micrometre length scale $\rho/e \ll \sum_i c_i$. In effect, the relative difference in ion number densities for a 1:1 electrolyte is given by $(c_+ - c_-)/(c_+ + c_-) = \nabla \cdot (\varepsilon \mathbf{E})/e(c_+ + c_-) \sim \varepsilon E/ecl$ and is very small for saline solutions on the micrometre length scale for typical applied electric fields (Saville (1997); Castellanos *et al.* (2003)). However, the changes in liquid properties generated by Faradaic currents, may be important in the explanation of the fluid flow observations. Gradients in conductivity under an applied field can yield net charge and, consequently they are a source of bulk forces in the liquid. Experiments indicate that the relative importance of these bulk forces compared to forces in the diffuse layer increases due to Faradaic currents. In effect, our measurements show that double layer impedance decreases with voltage amplitude, which means that the ratio of the voltage drop across the double layer to the total applied voltage is smaller.

From the continuity equation for the electrical current ($\nabla \cdot \mathbf{J} = 0$) and the quasi-electroneutrality assumption, the induced charge in the bulk is given by (Newman & Thomas-Alyea (2004)):

$$\frac{\rho}{\varepsilon} = \frac{\nabla\sigma \cdot \nabla\phi}{\sigma} + \frac{\sum_i z_i e D_i \nabla^2 c_i}{\sigma} \tag{4.5}$$

where e is the proton charge, z_i, D_i and c_i are, respectively, the ionic valence, diffusion coefficient and concentration of species i. With liquid bulk we mean the region beyond the Debye layer. In chapter 6, it is discussed in which situations this charge could generate net flow.

The velocity profile generated by a TW microelectrode arrays was found to correspond to Fig. 4.3. The net fluid flow is generated at the level of the electrodes, but this does not mean that the electrical forces are confined inside the EDL. If bulk forces exist and act within a distance of typically the size of the electrodes, a similar fluid flow profile would be obtained. Comparing the results for titanium and platinum electrodes indicates that the role of the metal seems important: The threshold voltage is higher for titanium electrodes. Titanium is a metal which readily forms a highly resistant oxide layer and this was accounted for in the linear ACEO calculations presented in Green *et al.* (2002a); Ramos *et al.* (2005). Since Faradaic reactions are responsible for the changes in the liquid properties, the chemical nature of the metal may be important. The thin oxide layer on titanium acts as passivation layer so higher voltages are required to generate Faradaic currents on titanium, consistent with the observed increase in threshold voltage.

4.7.1 Analysis of the conductivity effect

In our closed channel, the electroosmotic slip velocity generates a Couette flow that is counterbalanced by a Poiseuille flow, so that there is zero net flow along the channel (see Figure 4.3). In this situation, the velocity at a distance 2/3 of the channel height above the electrodes is equal to a third of the average velocity at the electrodes level. Therefore, the velocity measurements given in Figures 4.12(a)-4.13(d), that were obtained at this height, are readily translated to pumping velocities multiplying them by a factor of 3.

According to the linear theory, the frequency of maximum velocity for this array is $f = 9057\sigma/C_{DL}$ in S.I. units (Ramos *et al.* (2005)). If we take $C_{DL} = \varepsilon/\lambda_D$ (the capacitance of the double layer given by the Debye-Huckel theory), we can compare the theoretical predictions with the experimental values:

σ [mS/m]	1.5	7.7	16.9
f_{theo} [Hz]	590	1340	1985
f_{exp} [Hz]	~500	~1000	~ 1800

Table 4.2: Theoretical and experimental frequencies for peak velocities.

The experimental frequencies of maximum velocity are close to the theoretical values given by the Debye-Huckel model. According to the linear theory for perfectly polarizable electrodes, the value of the maximum pumping velocity is given by $U = \Lambda\ 0.00137V_0^2$ (in S.I. units) (Ramos *et al.* (2005)). The parameter Λ represents the ratio between the voltage drop across the diffuse layer and that across the total double layer. The qualitative explanation for the decrement of the slip velocity with conductivity is the following: As the ionic strength increases, the diffuse (mobile) part of the double layer gets thinner and more voltage is dropped across the compact part of the double layer. Therefore, the parameter Λ and the induced velocity decrease with increasing conductivity. Table 4.3 shows the values of the parameter Λ required to obtain the experimental velocities.

V_{pp} [volt]	1	1.25	1.5
Λ ($\sigma = 1.5$) mS/m	0.23	0.20	0.18
Λ ($\sigma = 7.7$) mS/m	0.18	0.16	0.14
Λ ($\sigma = 16.9$) mS/m	0.10	0.10	0.10

Table 4.3: Experimental values of the parameter Λ.

The small values for Λ cannot be explained easily. We could consider that there is an oxide layer that decreases the compact-layer capacitance and, therefore, reduces the voltage drop across the diffuse layer and the induced slip velocity. However, a smaller double-layer capacitance would predict a higher frequency for maximum velocity. Faradaic reactions can diminish the value of the maximum velocity without shifting the frequency of the peak velocity, as shown in section 5. This would imply that even for the smallest voltages, there are electro-chemical reactions at the electrodes that depolarize the interface. The non-linear Gouy-Chapman model for the diffuse layer can account for some reduction of the expected velocity (González *et al.* (2008b)), but it is difficult to get a reduction factor around 5 or more for $V_0 = 0.5\,\mathrm{V}$. Other possibilities that reduce the electroosmotic velocity could be important in order to account for the discrepancy. For instance: (a) viscous friction in the double layer could increase due to ion crowding at voltages much greater than $k_BT/e = 0.025\,\mathrm{V}$ (steric effects) (Bazant *et al.* (2008)); and (b) the position of the shear plane could be beyond the Outer Helmholtz Plane (OHP) due to the existence of a hydrodynamic stagnant layer (Delgado *et al.* (2005)), which reduces the zeta potential as compared to the diffuse-layer potential.

With respect to the problem of flow reversal, TW experiments show that the minimum threshold voltage increases with electrolyte conductivity. This suggests that concentration polarization effects could be important in the origin of this phenomenon. In effect, a given Faradaic current density determines the gradients in ion concentration and, consequently, the induced free charge would be inversely proportional to bulk conductivity, according to equation 4.5. Concentration polarization effects are reduced as the ionic concentration is increased, which seems to correlate with our observations on the onset of the flow reversal in TW microelectrode arrays.

4.8 Conclusions

The platinum microelectrode arrays with two different electrode width and spacings had similar flow characteristics in the voltage-frequency domain. Both showed four distinct regions: normal pumping, reverse pumping, no net pumping and non-uniform motion. In both arrays, at low voltages the liquid flow was in accordance with predictions given by AC electroosmotic theory (*Normal Pumping*). Typical frequencies were lower for array A (larger electrodes). Lower velocities were found with this array for the same signal amplitude. At voltages above a threshold, net fluid flow was reversed. Flow reversal occurred at lower voltages for the array with smaller electrodes (array B). There does not appear to be a local maximum velocity in the Reverse pumping mode - the velocity increases with decreasing frequency until the non-uniform region is reached. Comparison with data using titanium microelectrode arrays shows that the threshold voltage was greater for these electrodes. Typical frequencies for *Normal pumping* were lower for the platinum electrode array than for the titanium electrode array.

Impedance measurements show that liquid properties change after the application of the TW signals; these changes are greatest near the electrodes. As a result of this, gradients in conductivity appear, which would give rise to bulk forces in the liquid. Measurements of the electrical current during pumping showed transient behaviour. At specific voltages - around the threshold voltage - simultaneous measurements of fluid velocity and electrical current showed a strong correlation. Faradaic currents are responsible for this transient behaviour and for the gradients in conductivity. The observation of non-uniform motion could be due to EHD instabilities caused by these conductivity gradients. When DI water was used the results were similar, indicating that electrochemical reactions of water could be responsible for the observations. This was confirmed with experiments with fluorescent dyes that indicated electrochemical reactions at the electrodes, leading to a pH decrement as well as concentration polarization oscillating with the frequency of the applied signal. These results lead us to explore in chapter 6 how the action of the travelling-wave field on the ionic concentration gradients in the electrolyte bulk can generate net flow over the microelectrode array.

The same behaviour was found for a linear array and a circular one. In addition, the height of the microfluidic channel had an influence on the pumping performance. Flow reversal requires higher voltages and frequencies for shallow channels. The study of the conductivity effect showed that, in experiments with a higher electrolyte conductivity, higher voltages were required for the observation of flow reversal. These observations are in accordance with the hypothesis that ionic concentration gradients generated by electrochemical reactions are responsible for flow reversal.

Chapter 5

Faradaic currents effect on Travelling-Wave Electroosmosis (Equal ionic diffusivities).

Most of the theoretical studies on AC electroosmosis have been performed for perfectly blocking electrodes, i.e., with no Faradaic currents. Experimental results in chapter 4 show that electrochemical reactions are not an exception but a rule when a few volts are applied to the microelectrode arrays. Olesen *et al.* (2006) included the effect of Faradaic currents in the analysis of the AC electroosmotic pumping produced by an array of asymmetric pairs of electrodes. In their study, the effect of the mass transfer on the reaction kinetics was not included. However, more recently, Olesen included this effect in his thesis dissertation (Olesen (2006)). Their study was also restricted to the case of frequencies much smaller than σ/ε (or equivalently, $\omega << D/{\lambda_D}^2$) in order to analyse nonlinearities using asymptotic expansions.

In this chapter we study the effect of Faradaic currents taking into account mass transfer effects (i.e. including the Warburg impedance) for a binary electrolyte with equal ionic diffusivities and for any frequency in the TW array. The electrokinetic equations are integrated using the linear and thin-layer approximations. A mixed boundary condition for the electric potential is obtained and, from this, the time-averaged electroosmotic slip velocity generated on the surface of the electrodes. The model is then applied to obtain the electroosmotic slip velocity induced by a single mode TW potential. Finally, the average slip velocity over a wavelength generated by a four-phase TW microelectrode array is computed using finite elements.

5.1 Governing Equations

We consider the case of an anion that reacts at the electrodes to produce a neutral molecule according to the reaction:

$$X^0 + e^- \rightleftarrows X^- \tag{5.1}$$

in the presence of a cation, which aids in charge conservation. We assume that the electrolyte is 1-1 symmetric. The conservation equations of the species are written as

$$\begin{aligned}
\frac{\partial C_+}{\partial t} &= D_+\nabla^2 C_+ + \mu_+\nabla\cdot(C_+\nabla\phi) &(5.2)\\
\frac{\partial C_-}{\partial t} &= D_-\nabla^2 C_- - \mu_-\nabla\cdot(C_-\nabla\phi) &(5.3)\\
\frac{\partial C_0}{\partial t} &= D_0\nabla^2 C_0 &(5.4)
\end{aligned}$$

where C_+, C_-, C_0 are the cation, anion and neutral molecule concentrations. The convective terms, of the form $\nabla \cdot (\mathbf{u}C_i)$, have not been included here because the fluid velocity is caused by the applied TW potential and, therefore, they are negligibly small under the linear approximation. We are going to assume that the diffusion coefficients and electrical mobilities of all species are equal to D and $\mu = eD/k_BT$ (where e is the charge of a proton, k_B is the Boltzmann constant and T is the absolute temperature). Poisson's equation relates the electric potential to the ion concentrations,

$$-\nabla^2\phi = e\frac{C_+ - C_-}{\varepsilon} \tag{5.5}$$

where ε is the permittivity of the solution. The boundary conditions at the electrodes (placed at $z = 0$) are

$$\begin{aligned} -D\frac{\partial C_+}{\partial z} - \mu C_+\frac{\partial \phi}{\partial z} &= 0 && (5.6)\\ -D\frac{\partial C_-}{\partial z} + \mu C_-\frac{\partial \phi}{\partial z} &= -\frac{J_F}{e} && (5.7)\\ -D\frac{\partial C_0}{\partial z} &= \frac{J_F}{e} && (5.8) \end{aligned}$$

where J_F is the Faradaic current density ($J_F > 0$ if the electron jumps from the ion to the metal). The Butler-Volmer kinetic equation relates the Faradaic current to the local concentrations of reacting species and the potential drop across the compact layer,

$$\frac{J_F}{e} = K_-C_-\exp\left((1-\alpha)e\Delta\phi_s/k_BT\right) - K_0C_0\exp\left(-\alpha e\Delta\phi_s/k_BT\right) \tag{5.9}$$

where α is the transfer coefficient, K_- and K_0 are the kinetic rate constants when $\Delta\phi_s = 0$, and $\phi_s = V - \phi$ is the potential drop across the Stern compact layer. That is, $\Delta\phi_s$ is the potential difference between the electrode and the beginning of the continuum region (Bonnefont *et al.* (2001)). If $\Delta\phi_s > 0$, a positive current going from the electrode to the solution is favored.

An additional boundary condition is needed to close the mathematical problem (Bonnefont *et al.* (2001)). This condition can be seen as the continuity of the normal component of the electric displacement at the boundary between the Stern and diffuse layers,

$$\varepsilon_s\frac{\Delta\phi_s}{h} = -\varepsilon\frac{\partial\phi}{\partial z} \tag{5.10}$$

where h and ε_s are the thickness and effective permittivity of the Stern layer, respectively. Here, we have considered a constant capacitance, ε_s/h, for the Stern layer. In the present model, chemical adsorption effects are not considered.

5.2 Thin-double-layer and linear approximations

In the thin-double-layer approximation, electroneutrality is assumed in the bulk, the species concentrations are homogeneous through the bulk, and they vary mainly in a thin layer adjacent to the interface. There are two different length scales: a small scale that is the typical length of the double layer, and a large scale that corresponds to the characteristic dimension of the electrodes. This difference in scales allows us to use the matched asymptotic expansion method (Bender & Orszag (1987)). Electroneutrality in the bulk implies that the electric potential satisfies Laplace's equation,

$$\nabla^2 \phi_{bulk} = 0 \tag{5.11}$$

The boundary conditions for the potential are obtained by integrating the electrokinetic equations in the thin double layer.

We assume that in the equilibrium state the net Faradaic current is equal to zero. In the linear approximation, we consider that the equilibrium is slightly perturbed by applying to the electrodes an alternating potential of small amplitude with angular frequency ω, $V = \mathrm{Re}[V(x)\exp(i\omega t)]$. Here $V(x)$ is a piecewise-defined complex function that denotes the phasor voltage (amplitude and phase) applied to the electrode placed at x. We assume that the equilibrium state is such that there is no charge in the diffuse layer (or that this is very small, so that the intrinsic potential does not affect the AC potential (González *et al.* (2000))). In the thin layer, we have

$$C_+ = C_+^{eq} + n_+; \quad C_- = C_-^{eq} + n_- \tag{5.12}$$

$$C_0 = C_0^{eq} + n_0; \qquad \phi = 0 + \phi \tag{5.13}$$

$$\tag{5.14}$$

where C_i^{eq} are the bulk concentrations at equilibrium, and $n_i << C_i^{eq}$. Since we have assumed that the reference state is of zero charge, we have $C_+^{eq} = C_-^{eq} = C^{eq}$. The thin-double-layer approximation assumes that variations in the direction perpendicular to the interface are much greater than variations in the tangential direction. This assumption leads to 1D equations for the variables in the thin-layer region (González *et al.* (2000)). Using complex amplitudes, the linear equations for the perturbations n_+, n_-, n_0, ϕ in the thin layer are

$$\begin{aligned}
\frac{\partial^2\phi}{\partial z^2} &= -e\frac{n_+ - n_-}{\varepsilon} && (5.15)\\
i\omega n_+ &= D\frac{\partial^2 n_+}{\partial z^2} + \mu\frac{\partial}{\partial z}\left(C^{eq}\frac{\partial\phi}{\partial z}\right) \\
&= D\frac{\partial^2 n_+}{\partial z^2} - \mu C^{eq} e\frac{n_+ - n_-}{\varepsilon} && (5.16)\\
i\omega n_- &= D\frac{\partial^2 n_-}{\partial z^2} - \mu\frac{\partial}{\partial z}\left(C^{eq}\frac{\partial\phi}{\partial z}\right) \\
&= D\frac{\partial^2 n_-}{\partial z^2} + \mu C^{eq} e\frac{n_+ - n_-}{\varepsilon} && (5.17)\\
i\omega n_0 &= D\frac{\partial^2 n_0}{\partial z^2} && (5.18)
\end{aligned}$$

The boundary conditions 5.6-5.8 at $z = 0$ can be written, removing J_F, as

$$\begin{aligned}
0 &= -D\frac{\partial n_+}{\partial z} - \mu C^{eq}\frac{\partial\phi}{\partial z} && (5.19)\\
D\frac{\partial n_0}{\partial z} &= -D\frac{\partial n_-}{\partial z} + \mu C^{eq}\frac{\partial\phi}{\partial z} && (5.20)\\
-D\frac{\partial n_0}{\partial z} &= K_- n_- - K_0 n_0 + \frac{eK_- C^{eq}}{k_B T}\Delta\phi_s && (5.21)\\
0 &= \Delta\phi_s + \lambda_s\frac{\partial\phi}{\partial z} && (5.22)
\end{aligned}$$

where $\lambda_s = h\varepsilon/\varepsilon_s$. Because the reference state is of zero Faradaic current, we have $K_- C_-^{eq} = K_0 C_0^{eq}$. Note that the transfer coefficient α disappears in the linear analysis.

In order to solve these equations, we define $n = n_+ + n_-$ and $\rho = e(n_+ - n_-)$. Defining $\sigma = 2\mu e C^{eq}$ as the conductivity of the reference state, the equations for ϕ, ρ, and n are now written as

$$
\begin{aligned}
-\frac{\partial^2\phi}{\partial z^2} &= \frac{\rho}{\varepsilon} && (5.23)\\
D\frac{\partial^2\rho}{\partial z^2} &= i\omega\rho + \frac{2\mu e C^{eq}}{\varepsilon}\rho = i\omega\rho + \frac{\sigma}{\varepsilon}\rho && (5.24)\\
D\frac{\partial^2 n}{\partial z^2} &= i\omega n && (5.25)
\end{aligned}
$$

while the equation for n_0 is Eq. 5.18.

The general solutions for n, ρ, n_0, and ϕ inside the thin layer are

$$
\begin{aligned}
n &= A\exp(-zr);\; \rho = B\exp(-zs);\; n_0 = C\exp(-zr) && (5.26)\\
\phi &= -\frac{B}{\varepsilon s^2}\exp(-zs) + F + Gz && (5.27)
\end{aligned}
$$

where $r = \sqrt{i\omega/D}$, $s = \sqrt{i(\omega/D) + (\sigma/\varepsilon D)}$, $\mathrm{Re}[r] > 0$, $\mathrm{Re}[s] > 0$, and A, B, C, F, and G are constants of integration. We have assumed, according to the thin-layer approximation, that the typical system length l is much greater than $\max(\lambda_D, \sqrt{D/\omega})$, where the Debye length is given by $\lambda_D = \sqrt{\varepsilon D/\sigma}$. According to the matched asymptotic expansion method, the matching conditions between the thin-layer potential and the bulk potential impose that the constants F and G are, respectively, the potential $\phi_{bulk}|_{z=0}$ and its normal derivative $\partial\phi_{bulk}/\partial z|_{z=0}$ at the beginning of the bulk side (González *et al.* (2000)).

Application of the boundary conditions 5.19-5.22 leads to the equations

$$
\begin{aligned}
0 &= eDAr + DBs - \sigma\frac{B}{\varepsilon_s} - \sigma G && (5.28)\\
-2eDCr &= eDAr - DBs + \sigma\frac{B}{\varepsilon s} + \sigma G && (5.29)\\
-eDAr &= \frac{eK_-}{2}\left(A - \frac{B}{e}\right) - eK_0C + \frac{1}{R_{ct}}\left(V + \frac{B}{\varepsilon s^2} - F\right) && (5.30)\\
V + \frac{B}{\varepsilon s^2} - F &= -\lambda_s\left(\frac{B}{\varepsilon s} + G\right) && (5.31)
\end{aligned}
$$

where $R_{ct} = k_BT/e^2K_-C^{eq}$. From Eqns. 5.28, 5.29 above, $C = -A$ is obtained. The charge density amplitude B can be written as $B = \varepsilon s^2\beta G$, where

$$
\beta = \frac{\sigma - \lambda_s/R_{ct} + \sigma\xi}{\frac{1}{2}K_- + \lambda_s/\varepsilon s R_{ct} + i\omega/s + i\xi\omega/s}\left(\frac{1}{\varepsilon s^2}\right) \qquad (5.32)
$$

and $\xi = (\frac{1}{2}K_- + K_0)/\sqrt{i\omega D}$. The potential drop across the total double layer is

$$\Delta\phi_{DL} = V - F = -\frac{B}{\varepsilon s^2} - \lambda_s \frac{B}{\varepsilon s} - \lambda_s G = -(\beta + s\lambda_s\beta + \lambda_s)G \quad (5.33)$$

Because $F = \phi_{bulk}|_{z=0}$ and $G = \partial\phi_{bulk}/\partial z|_{z=0}$, we have obtained a mixed boundary condition for the bulk potential at $z = 0$, which is

$$\phi_{bulk} - \gamma\frac{\partial\phi_{bulk}}{\partial z} = V \quad (5.34)$$

with $\gamma = \beta + s\lambda_s\beta + \lambda_s$. Notice that $-B/\varepsilon s^2 = -\beta G$ is the potential drop across the diffuse layer, $\Delta\phi_{diff} = \phi_{diff}(0) - \phi_{bulk}(0)$.

5.2.1 Low frequencies

When the signal frequency is much lower than the Debye frequency, $\omega \ll \sigma/\varepsilon$, the expression for γ can be simplified. In this case, $s \approx 1/\lambda_D$, $\gamma \approx \beta(1 + \lambda_s/\lambda_D) + \lambda_s$, and, taking into account $\frac{1}{2}R_{ct}K_- = \lambda_D{}^2/\varepsilon$,

$$\beta = \frac{R_{ct}\sigma - \lambda_s + R_{ct}\sigma\xi}{1 + \lambda_s/\lambda_D + i\omega R_{ct}(1+\xi)\varepsilon/\lambda_D} \quad (5.35)$$

The parameter γ is now

$$\gamma = \frac{R_{ct}\sigma - \lambda_s + R_{ct}\sigma\xi}{1 + i\omega R_{ct}(1+\xi)C_{DL}} + \lambda_s \simeq \frac{R_{ct}\sigma(1+\xi)}{1 + i\omega R_{ct}(1+\xi)C_{DL}} \quad (5.36)$$

where $C_{DL} = \varepsilon/(\lambda_D + \lambda_s)$ is the total capacitance per unit area of the double layer (compact and diffuse capacitances in series). This expression for γ is obtained under the assumption that $\omega\lambda_s C_{DL} \ll \sigma$, which is reasonable in the limit $\omega\varepsilon/\sigma \ll 1$. In this range of low frequencies, the double layer in our model behaves as a Randles circuit (Bard & Faulkner (2001)). This is composed of two impedances in parallel; one is the capacitance of the double layer C_{DL} and the other is the series combination of the reaction resistance R_{ct} and the Warburg impedance Z_W (see Fig. 5.1), i.e.,

$$Z = \frac{R_{ct} + Z_W}{1 + i\omega R_{ct}C_{DL} + i\omega C_{DL}Z_W} \quad (5.37)$$

In our case, the double-layer specific impedance is $Z = \gamma/\sigma$, the reaction resistance is $R_{ct} = k_B T/K_- C^{eq}e^2$, the double-layer capacitance is $C_{DL} = \varepsilon/(\lambda_D + \lambda_s)$, and the Warburg impedance is

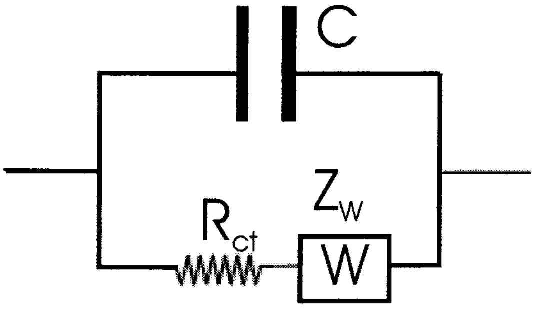

Figure 5.1: Randles circuit

$$Z_W = \frac{R_{ct}(\frac{1}{2}K_- + K_0)}{\sqrt{iD\omega}} = \frac{\lambda_D{}^2(1 + 2K_0/K_-)}{\varepsilon\sqrt{iD\omega}} \tag{5.38}$$

The Warburg impedance represents a kind of resistance to mass transfer (Bard & Faulkner (2001)). Because of the Faradaic reactions, the local concentrations at the electrode of the reacting species are different from the bulk concentrations: the produced species concentration increases while the consumed species concentration decreases. These changes in local concentrations contribute to slowing down the Faradaic reactions; which can be seen as an additional impedance in series with the reaction resistance.

Important limits of the double-layer impedance are obtained for the cases where the electrodes are perfectly blocking, and where the electrode kinetics is so fast that the species concentrations are in quasi-equilibrium. The case of perfectly blocking (polarizable) electrodes is obtained when $R_{ct} \to \infty$. The intrinsic double-layer impedance is then $Z = 1/i\omega C_{DL}$.

When the electrode kinetics is very facile, i.e., when the exchange current is much greater than the existing Faradaic current, the concentrations at the electrodes are in electrochemical equilibrium (Bard & Faulkner (2001)). The surface concentrations of reacting species follow the Nernst equation. Equation 5.7 is now written as

$$0 = K_- n_- - K_0 n_0 + K_- C^{eq} \frac{e\Delta\phi_s}{k_B T} \tag{5.39}$$

and the remaining equations are unchanged. The solution for B as a function of G is

$$B = \frac{-\lambda_s + R_{ct}\sigma\xi}{\lambda_D{}^2/\varepsilon + \lambda_D\lambda_s/\varepsilon + i\omega R_{ct}\xi\lambda_D}G \tag{5.40}$$

The double layer impedance is now given by the Randles impedance with $R_{ct} = 0$ but $R_{ct}K_- = 2\lambda_D^2/\varepsilon$:

$$Z = \frac{Z_W}{1 + i\omega C_{DL}Z_W} = \frac{R_{ct}(\frac{1}{2}K_- + K_0)/\sqrt{i\omega D}}{1 + C_{DL}R_{ct}(\frac{1}{2}K_- + K_0)\sqrt{i\omega/D}} \tag{5.41}$$

5.3 Slip velocity

The electroosmotic flow arises from the balance between the electrical and viscous tangential stresses in the thin double layer. For a general variation of potential in the bulk, there will be lateral forces and electroosmotic slip velocity. Under the thin-layer approximation, the equation that we must integrate to obtain the time-averaged slip velocity is (González *et al.* (2000))

$$\eta\frac{\partial^2 u}{\partial z^2} = \frac{\partial\langle p\rangle}{\partial x} + \left\langle\rho\frac{\partial\phi}{\partial x}\right\rangle = \frac{\varepsilon}{4}\frac{\partial}{\partial x}\left|\frac{\partial\phi}{\partial z}\right|^2 - \frac{\varepsilon}{4}\left(\frac{\partial^2\phi}{\partial z^2}\frac{\partial\phi^*}{\partial x} + \frac{\partial^2\phi^*}{\partial z^2}\frac{\partial\phi}{\partial x}\right) \tag{5.42}$$

where $\langle\cdots\rangle$ indicates the time average and ϕ^* the complex conjugate of ϕ. The potential in the diffuse layer is $\phi_{diff} = -(B/\varepsilon s^2)\exp(-zs) + F + Gz$. Integrating Eq. 6.5 twice and applying the boundary conditions of nonslip at the outer Helmholtz plane ($u(0) = 0$) and viscous stresses going to zero outside the thin layer ($\partial u/\partial z = 0$ for $z \longrightarrow \infty$) leads to

$$\begin{aligned} u_{slip} \equiv u(\infty) = -\frac{\varepsilon}{4\eta}\Bigg(&\frac{M_xG^* + 3MG_x^* + sMF_x^*}{s^3} \\ &-\frac{M_xM^*}{s^2(s+s^*)^2} + \frac{M_xM^*}{ss^*(s+s^*)^2} + c.c.\Bigg) \end{aligned} \tag{5.43}$$

where c.c means complex conjugate, subscript x denotes here partial derivative with respecto to x, and $M = B/\varepsilon$. We have taken into account that terms of the form $GG_x^*z^2$ are on the order of $(\lambda_D/L)^2$ and, therefore, are negligibly small. We recall here that $F = \phi_{bulk}|_{z=0}$ and $G = \partial\phi_{bulk}/\partial z|_{z=0}$. The terms M_xG^* and MG_x^* are much smaller than sMF_x^*. In effect, the exponential factor s is on the order of $1/\lambda_D$ and, therefore, $M_xG/sMF_x \sim (\lambda_D/L)(G/F_x) \ll 1$ (the ratio G/F_z between normal and tangential electric field components in the bulk is assumed to be of order one).

At low frequencies, $\omega\varepsilon/\sigma \ll 1$, the exponential factor $s \approx \lambda_D^{-1}(1 + i\omega\varepsilon/2\sigma)$ and

$$-\frac{M_x M^*}{s^2(s+s^*)^2} + \frac{M_x M^*}{ss^*(s+s^*)^2} \approx \frac{i(M_x M^* - M_x M^*)\lambda_D^4}{4}\frac{\varepsilon\omega}{\sigma} \qquad (5.44)$$

so these terms go to zero as $\varepsilon\omega/\sigma \to 0$. Therefore, we can write the slip velocity at low frequencies as

$$u_{slip} = -\frac{\varepsilon}{4\eta}\left(\frac{MF_x^*}{s^2} + c.c.\right) \qquad (5.45)$$

This is the expression that can be obtained applying the Smoluchowski formula, since we can identify $-M/s^2 = \Delta\phi_{diff} = \phi_{diff}(0) - \phi_{bulk}(0)$ and $-F_x = E_x$, the tangential electric field from the bulk side. The Smoluchowski expression can be applied when the double layer is in quasi-equilibrium, i.e., when the ionic concentrations follow the Boltzmann distribution in the double layer (Rubinstein & Zaltzman (2001)). We can write

$$u_{slip} = -\frac{\varepsilon}{2\eta}\mathrm{Re}[\Delta\phi_{diff}E_x^*] = -\frac{\varepsilon}{2\eta}\mathrm{Re}\left[\frac{\beta}{\gamma}\Delta\phi_{DL}E_x^*\right] \qquad (5.46)$$

At low frequencies, the ratio $\beta/\gamma \approx (1 + \lambda_s/\lambda_D)^{-1}$ and the slip velocity over an electrode can be written as (Green *et al.* (2002a))

$$u_{slip} = -\frac{\varepsilon}{4\eta(1+\lambda_s/\lambda_D)}\frac{\partial}{\partial x}|\Delta\phi_{DL}|^2 \qquad (5.47)$$

At higher frequencies, on the order of σ/ε, it is expected that the potential penetrates easily in the bulk. Therefore, the potential drop across the diffuse double layer $\Delta\phi_{diff} = -M/s^2$ should be much smaller (on the order of λ_D/L) than the potential drop in the bulk, F. Under this assumption, the slip velocity should again be given by Eq. 5.45 . For frequencies of the order of σ/ε, we use the complete expression for obtaining the slip velocity, although we have not found differences from the expression 5.45 for the range of parameters we have explored.

5.4 Single potential wave

Let us assume that the potential applied at the level of the electrodes can be approximated by a single potential wave of angular frequency ω and wave number $k = 2\pi/L$ of the form $V = V_0 \exp(i(\omega t - kx))$. The potential solution in the bulk that satisfies the Laplace equation and the boundary condition $V = \phi_{bulk} - \gamma\partial\phi_{bulk}/\partial z$ at $z = 0$ is

$$\phi_{bulk} = \frac{V_0 \exp\left(i(\omega t - kx) - kz\right)}{1 + k\gamma} \tag{5.48}$$

The potential drop across the diffuse double layer and the tangential electric field are respectively

$$\begin{aligned} \Delta\phi_{diff} &= \frac{\beta k V_0 \exp\left(i(\omega t - kx)\right)}{1 + k\gamma} \\ E_x &= \frac{ikV_0 \exp\left(i(\omega t - kx)\right)}{1 + k\gamma} \end{aligned} \tag{5.49}$$

The slip velocity as given by Eq. 5.45 is

$$u_{slip} = -\frac{\varepsilon k V_0^2}{2\eta}\frac{\mathrm{Im}[k\beta]}{|1 + k\gamma|^2} \tag{5.50}$$

The velocity is independent of the tangential coordinate x.

The term proportional to $M_x M^*$ gives a correction to the slip velocity,

$$-\frac{\varepsilon M_x M^*}{4\eta s^2 (s + s^*)^2} + c.c. = \frac{\varepsilon}{4\eta}\frac{k\omega' |\beta|^2}{1 + \sqrt{1 + \omega'^2}}\frac{k^2 V_0{}^2}{|1 + k\gamma|^2} \tag{5.51}$$

with $\omega' = \omega\varepsilon/\sigma$. The correction is on the order of $\omega' u_{slip}$ for $\omega' \ll 1$ and is on the order of $k|\beta| u_{slip}$ for $\omega' \sim 1$; in both cases the correction is usually negligible (for $\omega' \sim 1$, we expect that $k|\beta| \sim k\lambda_D$).

If the electrodes are perfectly polarizable, $K_- = K_0 = 0$, and we have $\beta = \sigma/i\omega\varepsilon s$ and

$$u_{slip} = \frac{\varepsilon k V_0^2}{2\eta}\frac{\mathrm{Re}[k\sigma]/\varepsilon\omega s}{|1 + k\lambda_s + (1 + s\lambda_s)k\sigma/i\omega\varepsilon s|^2} \tag{5.52}$$

In this case, the correction to the slip velocity given by the expression 5.51 can be seen to be $k\lambda_D$ times smaller than 5.52. The slip velocity expression 5.52 compares almost perfectly with the one given by Cahill *et al.* (2004),

$$u_{slip} = \frac{\varepsilon}{2\eta}\mathrm{Re}[1/s]\frac{\omega\tau V_0{}^2}{|i\omega\tau/k + 1/s + \lambda_s(1 + i\omega\tau)|^2} \tag{5.53}$$

with $\tau = \varepsilon/\sigma$. There is a small difference; here we have Re[1/s], where 1/Re[s] is written by Cahill *et al.* (2004) (probably a typographical error).

It is convenient to define nondimensional quantities in order to explore the influence of the different parameters on the electroosmotic slip velocity:

- slip velocity as $u'_{slip} = u_{slip}2\eta/\varepsilon k V_0^2$,
- frequency as $\Omega = \omega/\omega_c$ (where $\omega_c = \sigma k \lambda_D/\varepsilon$ is the typical frequency of AC electroosmosis),
- Debye length as $\lambda'_D = k\lambda_D$ (where k^{-1} is the typical length in the system),
- Stern layer factor δ as the ratio between diffuse layer and Stern layer capacitances $\delta = (\varepsilon/\lambda_D)/(\varepsilon_s/h_s) = \lambda_s/\lambda_D$,
- reaction resistance as $R' = \sigma k R_{ct}$ ($1/\sigma k$ is the bulk specific resistance),
- and Warburg impedance as $Z'_W = k\sigma Z_W = W/\sqrt{i\Omega}$, where the Warburg factor $W = \sqrt{k\lambda_D}(1 + 2K_0/K_-)$.

The nondimensional $\beta' = k\beta$ and $\gamma' = k\gamma$ are written, respectively, as

$$\beta' = \frac{R' - \lambda'_D\delta + W/\sqrt{i\Omega}}{1 + i\Omega\lambda'_D + (\delta + i\Omega R' + \sqrt{i\Omega}W)\sqrt{1 + i\Omega\lambda'_D}} \tag{5.54}$$

and $\gamma' = \beta' + \delta\beta'\sqrt{1 + i\Omega\lambda'_D} + \delta$. The nondimensional slip velocity for the single-mode travelling wave takes the form $u'_{slip} = -\mathrm{Im}[\beta']/|1 + \gamma'|^2$.

Fig. 5.2 shows the nondimensional velocity u'_{slip} as a function of frequency Ω for perfectly polarizable electrodes, i.e., $R_{ct} = \infty$. This was the problem studied by Cahill *et al.* (2004) and Ramos *et al.* (2005), and we include it here for completeness. We can see that as δ increases the maximum velocity decreases and the frequency of peak velocity increases. The parameter $\delta = \lambda_s/\lambda_D$ is a measure of the relative importance of the Stern layer, or of any insulating layer between the electrodes and the electrolyte, as in the case analyzed by Cahill *et al.* (2004). The parameter δ also increases with the conductivity of the electrolyte, since the Debye length $\lambda_D \propto 1/\sqrt{\sigma}$. Therefore, decreasing velocities are obtained for increasing conductivity, as observed experimentally (Green *et al.* (2000a); Cahill *et al.* (2004)). The frequency for maximum velocity is $\Omega = 1$ (dimensional $\omega = \sigma k\lambda_D/\varepsilon$) for $\delta = 0$ and increases for increasing δ until it saturates at $\Omega = 1/\lambda'_D$ (dimensional $\omega = \sigma/\varepsilon$), corresponding to the charge relaxation frequency. Therefore, if a thick dielectric coating exists between the electrodes and the electrolyte, the fluid motion is important at frequencies

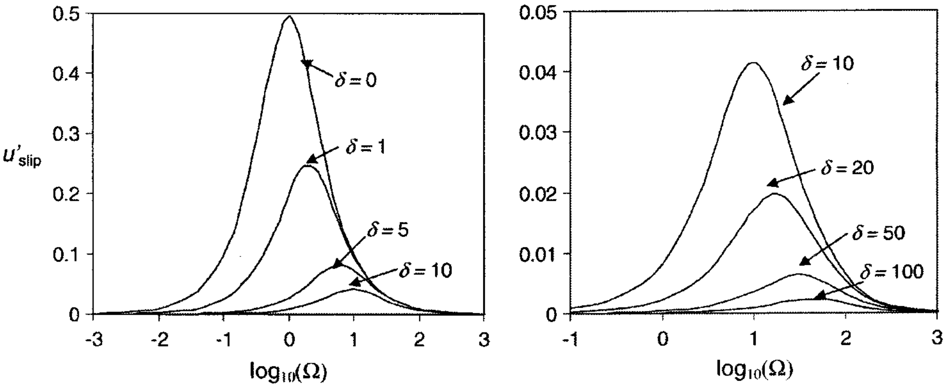

Figure 5.2: Nondimensional velocity u'_{slip} as a function of nondimensional frequency Ω for different values of δ and $R' = \infty$, $\lambda_D = 10^-2$. The graph on the right is an enlargement to show u'_{slip} for values of $\delta \geqslant 10$

around σ/ε (Ehrlich & Melcher (1982)). According to the linear theory, the maximum electroosmotic velocity that can be obtained in a typical experimental situation in a microarray with wavelength $L = 100\,\mu$m, applied voltage $V_0 = 0.1$ V, $\lambda'_D = 0.001$ ($\lambda_D = 15.9$ nm), and $\delta = 0.1$ is $u_{slip} = 100$ μm/s. Several factors tend to diminish this expectation, such as oxide layers on the metal electrodes that increase δ (Ramos *et al.* (2005)), nonlinearities of the diffuse-double-layer capacitance (González *et al.* (2008a)), and Faradaic currents (Olesen *et al.* (2006)).

The effect of varying the reaction resistance is shown in Fig. 5.3. The figure depicts the slip velocity u'_{slip} against the frequency Ω for different values of R' and $\lambda'_D = 10^{-3}$, $\delta = 1$, $W' = 0.1$. For the range of frequencies that is relevant in this case ($\Omega \ll 1/\lambda'_D$ or dimensional $\omega \ll \sigma/\varepsilon$), the electrical behaviour of the double layer is well described by the Randles circuit of Fig. 5.1. We can see that as the reaction resistance varies from a high value such as $R' = 10^3$ (close to the limit of perfectly blocking electrodes) to $R' = 0$ (limit of very facile kinetics), the maximum velocity decreases, and a new peak velocity appears at low frequencies. At frequencies $\Omega \sim 1$, the maximum velocity decreases as R_{ct} decreases. Because the Faradaic current depolarizes the interface (the charge leaks from the double layer), the electroosmotic velocity is smaller as the resistance to the reaction, R_{ct}, decreases. For frequencies $\Omega \ll 1$, there is a new maximum for the velocity, which is related to the Warburg impedance. When $R' = 0$, the Warburg impedance is the only resistance to the Faradaic current. At these low frequencies the Faradaic

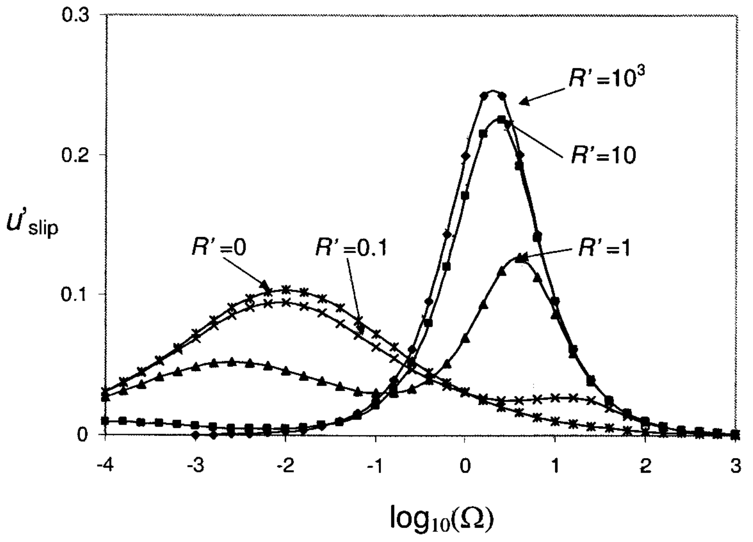

Figure 5.3: Nondimensional velocity u'_{slip} versus nondimensional frequency Ω for different values of R' and $\lambda'_D = 10^{-3}$, $\delta = 1$, $W = 0.1$.

current does not discharge the double layer because there is a significant Warburg impedance. For $R' = 0$, the maximum velocity is obtained for frequencies of the order of $\Omega \sim W^2$. It can be shown that for $\delta = 0$ and $\Omega \ll 1$, the analytical solution gives a maximum velocity $u'_{slip} = 0.2071$ for $\Omega = W^2$.

The effect of the Warburg impedance can be seen in Fig. 5.4. It shows the nondimensional velocity u_{slip} versus the nondimensional frequency Ω for different values of the Warburg factor W in the case $R' = 0$, $\lambda'_D = 10^{-3}$, $\delta = 1$. Here we analyze the effect of W when the reaction kinetics of the electrodes is very facile, i.e., the concentrations follow the Nernst equation. Mathematically, this implies that $R' = 0$ but $R_{ct}K_- \neq 0$. The Warburg factor is given by $W = \sqrt{k\lambda_D}(1 + 2K_0/K_-)$ and can take values from $\sqrt{k\lambda_D} = \sqrt{\lambda'_D}$ to infinity. The ratio between reaction constants is $K_0/K_- = C^{eq}/C_0^{eq}$; therefore, the ratio between equilibrium concentrations governs the Warburg factor. As in the previous case, the range of frequencies ($\Omega \sim 1$ or smaller) allows us to consider the double-layer electrical behaviour as a Randles circuit. We can see that as the Warburg factor increases, the peak velocity increases

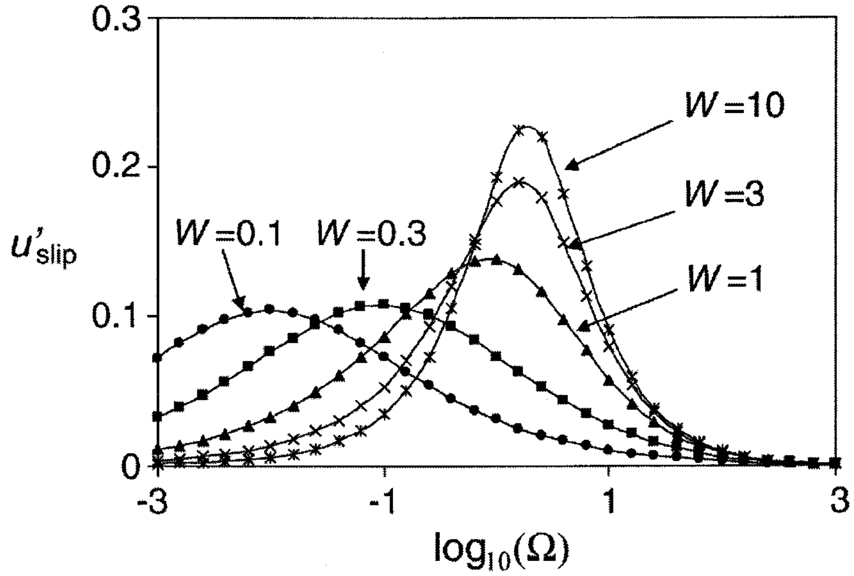

Figure 5.4: Nondimensional velocity u'_{slip} versus nondimensional frequency Ω for different values of W and $R' = 0$, $\delta = 1$ and $\lambda'_D = 10^{-3}$.

and also the nondimensional frequency. The high limit of the Warburg factor is equivalent to the case of perfectly blocking electrodes, even for a very facile kinetics. The mass transfer resistance is so large that the Faradaic current is negligible. The low limit of W is equivalent to the case analyzed in Fig. 5.3 for $R' = 0$. The velocity peaks at low frequencies around $\Omega \sim W^2$, corresponding to the polarization of the double layer because of the Warburg impedance.

It has to be noticed that for very low frequencies, the thin layer approximation used here is not applicable. This happens when the diffusion length $\sqrt{D/\omega}$ is of the order of k^{-1} or, in dimensionless form, when $\Omega \sim \lambda'_D$. At frequencies lower than this, the diffusion length becomes k^{-1} rather than $\sqrt{D/\omega}$. It can be shown that the solutions of n and n_0 for a single potential wave are $n = A\exp\left(i(\omega t - kx) - rz\right)$ and $n_0 = C\exp\left(i(\omega t - kx) - rz\right)$ with $r = \sqrt{k^2 + i\omega/D}$. This leads to saturation of the Warburg impedance to a value $Z_W = (1 + 2K_0/K_-)/\sigma k$ at

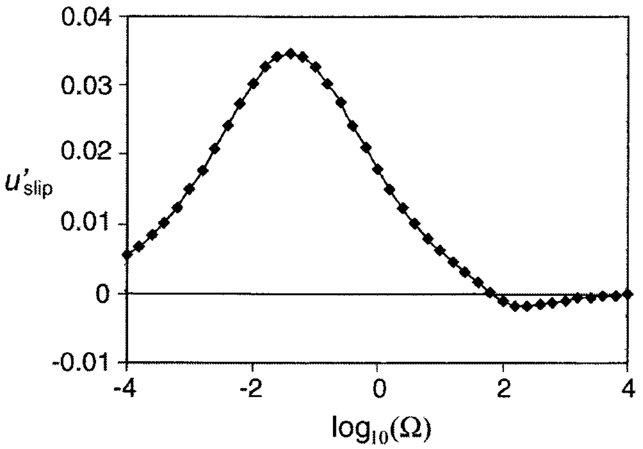

Figure 5.5: Nondimensional velocity u'_{slip} versus nondimensional frequency Ω for $R' = 0$, $W = 0.1$, $\delta = 5$ and $\lambda'_D = 10^{-2}$.

very low frequencies.

Faradaic currents have been proposed as a possible mechanism of flow reversal (Lastochkin *et al.* (2004)). In this work, we have not found reversal of fluid flow at the typical frequencies of AC electroosmosis $\Omega \sim 1$ for all the range of parameters that we have looked at. We have found some regions of flow reversal at high frequencies, on the order of $\Omega \sim 1/\lambda'_D$, for reactions with very facile kinetics, $R' \simeq 0$. This finding is not related to the current experimental observations of flow reversal. An example is shown in Fig. 5.5 for $R' = 0$, $W = 0.1$, $\delta = 5$ and $\lambda'_D = 10^{-2}$. The negative velocity peak is small and experimentally can be difficult to observe, since other factors could be important; for example, the kinetic reaction may not be very facile at these frequencies.

5.5 Array of electrodes subjected to a four-phase AC signal

In experiments, TW electric fields are generated by applying a four-phase AC signal to an array of electrodes. In this section, we analyze the velocity generated by a four-phase TW array when the electrode width and gap are both equal to d (the corresponding wavelength is $L = 8d$). We solve the electrical problem for this geometry using finite elements for

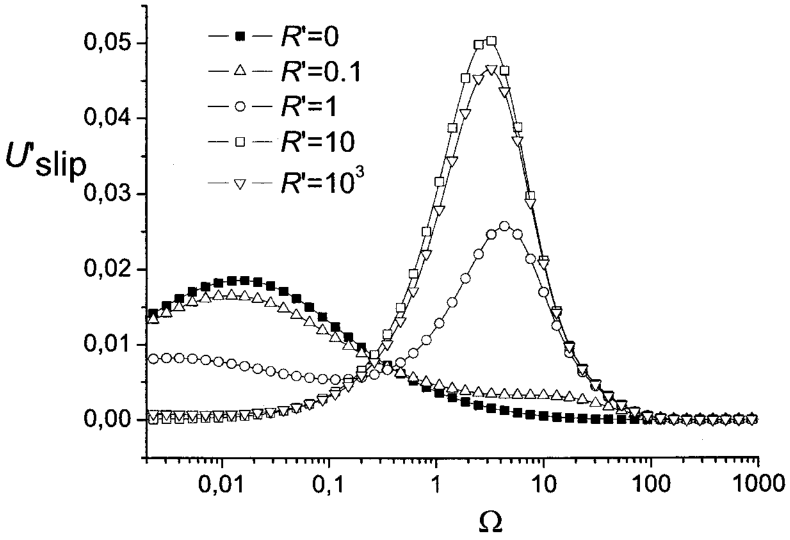

Figure 5.6: Nondimensional average velocity U'_{slip} versus nondimensional frequency Ω for $\lambda'_D = 10^{-3}$, $W = 0.1$, $\delta = 1$.

frequencies of the applied signal that are much smaller than the charge relaxation frequency $\omega \ll \sigma/\varepsilon$. Therefore, the surface impedance of the electrodes is the Randles impedance and the slip velocity is given by the Helmholtz-Smoluchowski formula.

The electric potential satisfies Laplace's equation in the domain. The boundary conditions for the potential are (a) the mixed boundary condition $\phi_{bulk} - \gamma\partial\phi_{bulk}/\partial z = V_i$ on the electrodes; (b) normal current equal to zero on the dielectric interface between electrodes $\partial\phi_{bulk}/\partial z = 0$; (c) normal current equal to zero at the top boundary $\partial\phi_{bulk}/\partial z = 0$ placed at a height much greater than d, $z_{top} = 40d/\pi$; (d) periodic conditions at right and left boundaries.

From the complex potential solution, we obtain the slip velocity on the electrodes using Eq. 6.5. The velocity on the dielectric between electrodes is zero (Ramos *et al.* (2005); Green *et al.* (2002a)). The average velocity in a wavelength is then obtained, taking into account that from symmetry the slip velocity on each electrode should be equal, i.e., $U_{slip} \equiv (1/L)\int_0^L u_{slip}(x)dx = (4/L)\int_0^d u_{slip}(x)dx$.

Fig. 5.6 shows the average nondimensional slip velocity $U_{slip} =$

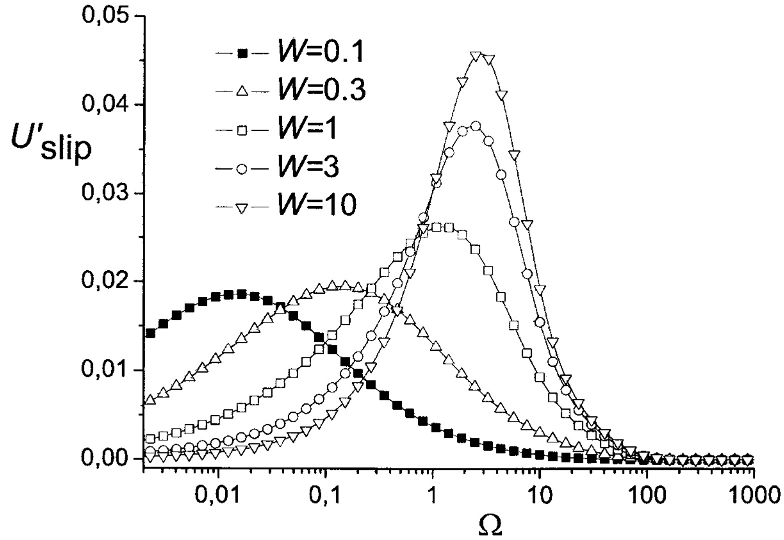

Figure 5.7: Nondimensional average velocity U'_{slip} versus nondimensional frequency Ω for $\lambda'_D = 10^{-3}$, $R' = 0$, $\delta = 1$.

$2\eta U_{slip}/\varepsilon k V_0^2$ as a function of nondimensional frequency $\Omega = \varepsilon\omega/\sigma k \lambda_D$ for different values of the nondimensional reaction resistance R' and $\delta = 1$, $W = 0.1$. Here the wavenumber is $k = \pi/4d$ and V_0 is the amplitude of the signal applied to each electrode. The frequency dependence of the average slip velocity generated by the four-phase TW array is similar to that shown in Fig. 5.3 for the case of a single-mode travelling-wave potential. Notice that in the case of the single mode $\mathrm{u_{slip}}$ is independent of x and, therefore, $U_{slip} = u_{slip}$. The maximum slip velocity in the four-phase microelectrode array is between 5 and 5.5 times smaller than the maximum velocity obtained by a single-mode traveling wave of the same amplitude V_0, in accordance with the results by Ramos *et al.* (2005). In addition, the frequencies for maximum velocity are shifted to higher values for the four-phase array. The maximum frequencies are between 1.3 and 1.5 times greater than for the single-mode traveling wave.

The nondimensional slip velocity versus the nondimensional frequency is plotted in Fig. 5.7 for different values of the Warburg factor W, in the case of $R' = 0$, $\delta = 1$, $\lambda'_D = 10^{-3}$. Again, the behaviour of the slip velocity is similar to the case of a pure travelling wave but with peak velocities between 5 and 5.5 times smaller and maximum frequencies between 1.3 and 1.5 times greater.

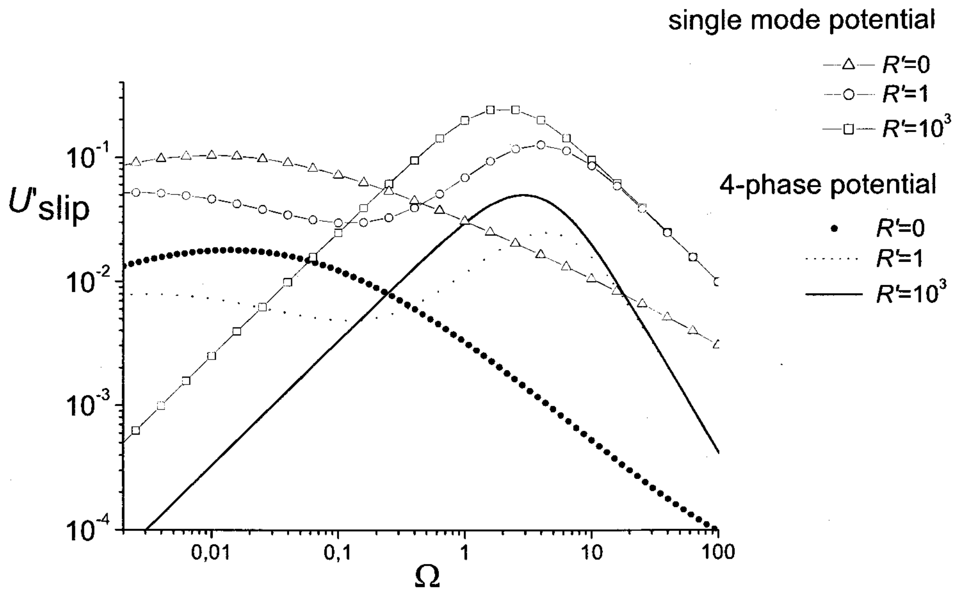

Figure 5.8: Nondimensional average velocity U'_{slip} versus nondimensional frequency Ω in a log-log plot for $W = 0.1$, $\lambda'_D = 10^{-3}$, $R' = 0$, $\delta = 1$.

Fig. 5.8 shows U'_{slip} versus Ω in a log-log scale in order to observe the asymptotic behaviour of the slip velocity with frequency. For $R' = \infty$ (no Faradaic reactions), the pumping velocity is proportional to Ω at low frequencies, $\Omega \ll 1$, as is predicted by the analytical solution for a single mode. This dependence on the frequency of the applied signal is different from that of the pumping velocity at $\Omega \ll 1$ in the case of the asymmetric array, where $U'_{slip} \propto \Omega^2$ (Olesen *et al.* (2006)). At frequencies $\Omega \gg 1$, the analytical solution for a single mode predicts $U'_{slip} \propto \Omega^{-1}$; however, the numerical solution for a four-phase microelectrode array predicts a faster decay of U'_{slip} with Ω. This can be attributed to the finite number of phases (four in our case) used to construct the TW potential, while the single mode has a continuum phase. At high frequencies, the slip velocity distribution over an electrode is concentrated in a narrow region close to the electrode edges. This is very different from the case of a single-mode TW potential, where the velocity is independent on x. For very facile kinetics $R' = 0$ and at high frequencies, the analytical solution of a single mode shows U'_{slip} proportional to $1/\sqrt{\Omega}$, as given by the Warburg impedance. However, when the Warburg impedance is greater than the capacitance impedance, the dependence is as $1/\Omega$ (much higher frequencies not shown here).

5.6 Conclusions

A linear analysis of the effect of Faradaic currents on the TW electroosmotic pumping of electrolytes has been carried out for the case of a binary electrolyte with equal ionic diffusivities. At signal frequencies much smaller than σ/ε, the predicted flow is always driven in the direction of the travelling-wave potential, as is obtained by linear and weakly nonlinear theoretical studies for blocking electrodes. Only for very facile reaction kinetics, $R' = 0$, and specific values of the other parameters, flow reversal was found at high frequencies, $\omega \sim \sigma/\varepsilon$, and this flow was of very small velocity amplitude. The effect of Faradaic currents is basically to decrease the slip velocity amplitude at frequencies on the order of $\omega \sim \sigma k \lambda_D/\varepsilon$ $(\Omega \sim 1, \omega \ll \sigma/\varepsilon)$. At these frequencies, the surface impedance can be described by a Randles type impedance and the slip velocity is given by the Helmholtz-Smoluchowski formula. The resistance to mass transfer, as given by the Warburg impedance, is the cause of the appearance of a new maximum for the electroosmotic slip velocity at low-frequencies $\omega \ll \sigma k \lambda_D/\varepsilon$ $(\Omega \sim W^2)$. The four-phase TW array was also analyzed and it showed velocities around five times smaller than the ones obtained for a single mode travelling-wave potential.

Chapter 6

Net flow generated by induced charge in the bulk

In this chapter we discuss the origin of electrical body forces and how these generate fluid motion over the travelling-wave microelectrode arrays. The goal is to describe situations where electrical charge is induced in the electrolyte bulk, creating a net fluid flow due to the action of the electric field on this charge. With electrolyte bulk we mean the region beyond the diffuse layer, that is, where electroneutrality or quasi-electroneutrality holds. At low frequencies and low ionic concentrations, electrothermal effects can be discounted as the origin of any appreciable motion (García-Sánchez *et al.* (2008)). Therefore we analyze only the case where conductivity gradients arise from electrochemical processes. Fluid velocity calculations are performed to evaluate the relative importance of the different terms in the body force, and to obtain order of magnitude estimates for the velocity.

An electrical body force occurs when there is a net electrical charge in the bulk of the liquid. Electrolytes are usually quasi-electroneutral ($\rho/e \ll \sum_i c_i$) at the micrometer scale. For instance, in the case of a 1:1 electrolyte, the relative difference in ion number densities corresponds to $(c_+ - c_-)/(c_+ + c_-) = \nabla \cdot (\varepsilon \mathbf{E})/e(c_+ + c_-)$ and is very small for saline solutions $\sim \varepsilon E/le2c_0 << 1$ (Saville (1997); Castellanos *et al.* (2003)). An applied electric field can induce electrical charge when gradients in the concentration of ionic species are present, as shown below. The induced charge satisfies $\rho/e \ll \sum_i c_i$ although $\rho\mathbf{E}$ can be sufficient to generate observable fluid flow. By neglecting the convection current compared with the ohmic current ($v\varepsilon/\sigma l \ll 1$. Castellanos *et al.* (2003)), the conduction current in an electrolyte is written as

$$\mathbf{J}_{\mathbf{cond}} = -\sum_i [e|z_i|c_i\mu_i(\nabla\phi) + ez_iD_i\nabla c_i] \tag{6.1}$$

where ϕ is the electric potential, e the proton charge and z_i, D_i, μ_i and c_i are the ionic valence, diffusion coefficient, ionic mobility and concentration of species i, respectively. From the continuity of the total electrical current ($\nabla \cdot \mathbf{J}_{\mathbf{tot}} = \nabla \cdot (\mathbf{J}_{\mathbf{cond}} - \varepsilon\partial_t\nabla\phi) = 0$) and the quasi-electroneutrality assumption, the charge density ρ in the bulk is given by (Newman & Thomas-Alyea (2004)):

$$\rho + \frac{\varepsilon}{\sigma}\frac{\partial\rho}{\partial t} = \frac{\varepsilon}{\sigma}\left(\nabla\sigma \cdot \nabla\phi + \sum_i ez_iD_i\nabla^2 c_i\right) \tag{6.2}$$

where $\sigma \equiv \sum_i e|z_i|\mu_i c_i$ is the electrolyte conductivity.

We consider situations where the induced charge and the electric field are oscillating functions with the same frequency as the applied potential in order to have $\langle \rho \mathbf{E} \rangle \neq 0$. If the driving field oscillates with frequency ω, the induced charge density oscillates with ω for two cases: (a) if the conductivity gradient has a non-zero time average $\langle \nabla\sigma \rangle \neq 0$ and/or (b) the Laplacian of the concentration $\nabla^2 c$ has a time-varying component with the same frequency as the electric field. The experimental observations in chapter 4 support these two possibilities: quasi steady-state gradients in conductivity due to non-symmetric Faradaic reactions in AC signals, and oscillations of the ionic concentration with the same frequency as the applied AC signal. In general, harmonics of higher order can appear in both the induced charge and electric field when the applied voltage can not be considered low. These harmonics can also contribute to a non-zero time-averaged force. Our study is just a first approximation to the problem.

6.1 Forces due to gradients in conductivity

In this section we compute fluid velocities for a conductivity gradient with a quasi-steady component, i.e. $\langle \nabla\sigma \rangle \neq 0$. The following equations are solved:

(I) The electric potential is given by electrical current conservation equation $\nabla\cdot((\sigma+i\omega\varepsilon)\mathbf{E} = 0)$. The polarization of the *electrode/electrolyte* interface is modeled by means of a Randles type surface impedance in the absent of a Warburg impedance $Z = R_{ct}/(1 + i\omega C R_{ct})$ (corresponding to a resistor and a capacitor in parallel), C is the capacitance (per unit area) of the interface and R_{ct} is the specific charge transfer resistance, i.e. the area specific resistance to Faradaic currents (Newman & Thomas-Alyea (2004); Olesen *et al.* (2006)). For simplicity, the Warburg impedance is not considered here, it could have an important role for low R_{ct} and low frequencies (chapter 5, Ramos *et al.* (2007)). The double layer capacitance C is estimated from the Debye-Huckel theory as $C = \varepsilon/\lambda_D$ (Hunter (1993)) (λ_D is the debye length and it is related to the diffusion coefficient by $\lambda_D = \sqrt{D\varepsilon/\sigma}$). The boundary condition on the electrodes is then:

$$-\mathbf{n}\cdot\nabla\Phi = \frac{V-\Phi}{\sigma Z} \qquad (6.3)$$

where V is the applied potential and Φ is the electric potential phasor ($\phi = \mathrm{Re}[\Phi \exp(i\omega t)]$). On the gap between electrodes, the boundary condition corresponds to zero normal current, i.e. $\mathbf{n} \cdot \nabla\Phi = 0$.

(II) The conductivity in steady state is obtained by solving the diffusion equation:

$$\nabla^2 \sigma = 0 \tag{6.4}$$

At the top of the channel, a constant conductivity $\sigma = \sigma_0$ is imposed. At the level of the electrodes, two different situations are considered: (1) In section 6.1.1 a vertical conductivity gradient is fixed on the electrodes, and (2) in section 6.1.2 the conductivity changes periodically along the electrode array.

(III) The fluid velocity is then obtained from the Stokes equations with electrical body forces:

$$\begin{aligned} \nabla \cdot \mathbf{u} &= 0 & (6.5) \\ -\nabla p + \eta \nabla^2 \mathbf{u} &= -\langle \rho \mathbf{E} \rangle & (6.6) \end{aligned}$$

where $\mathbf{u} = u\mathbf{e}_x + v\mathbf{e}_y$ is the velocity field and p the pressure. In this case $\tilde{\rho} = \varepsilon(\nabla\tilde{\sigma}/\tilde{\sigma}) \cdot \nabla\Phi$ with $\tilde{\sigma} = \sigma + i\omega\varepsilon$. The time-averaged force is then written as $\langle \rho \mathbf{E} \rangle = (1/2)\mathrm{Re}[\tilde{\rho}\mathbf{E}^*]$

No slip is imposed at the electrodes and at the interelectrode gaps. Note that, despite the polarization of the electrodes is accounted for the computation of the electric potential, no electroosmotic flow is considered here. We just want to analyze the contribution of the induced charge in the electrolyte bulk. At the top of the channel the stress tensor equals zero (neutral boundary condition). The velocity is homogeneous there ($\vec{u} = u\mathbf{e}_x$ with $\partial u/\partial y = 0$) and corresponds to the net pumping velocity generated by the array.

6.1.1 Vertical gradients in conductivity

If Faradaic currents generate a vertical gradient in conductivity, the situation is similar to that of AC electrothermal flows described by Melcher & Firebaugh (1967) and Fuhr *et al.* (1992b) - a wave of charge is induced in the electrolyte bulk. The characteristic frequency for this motion is

Inward flux Γ	$2 \cdot 10^{-2} \cdot \sigma_0\,\mathrm{mS/s}$
σ_0	$1.5\,\mathrm{mS/m}$
L	$160\,\mu\mathrm{m}$
D	$2 \cdot 10^{-9}\,\mathrm{m^2/s}$
V_0	$2\,\mathrm{volts}$
η	$10^{-3}\,\mathrm{Pa \cdot s}$

Table 6.1: Parameters for the fluid velocity computations.

the relaxation frequency of the liquid ($f = \sigma/2\pi\varepsilon$). If the liquid conductivity is higher near the electrodes, a vertical gradient would lead to fluid flow in the direction of the *reverse pumping mode.*

At high voltages and frequencies the electrochemical generation of conductivity gradients could be responsible of some fluid flow observations, but at the frequencies used in this work ($f \ll \sigma/2\pi\varepsilon$), the influence of this mechanism is not clear. According to this mechanism, and for $f \ll \sigma/2\pi\varepsilon$, the fluid velocity increases with frequency, contrary to observation, although electrochemical reaction rates decrease with increasing frequency. In fact, the dependence of the conductivity gradients on the applied signal can be rather complicated. To evaluate the influence of this term, we assume that the non-symmetrical electrochemical reactions generate a constant flux of conductivity. At the interelectrode gap the condition is that of zero flux ($\mathbf{n} \cdot \nabla\sigma = 0$).

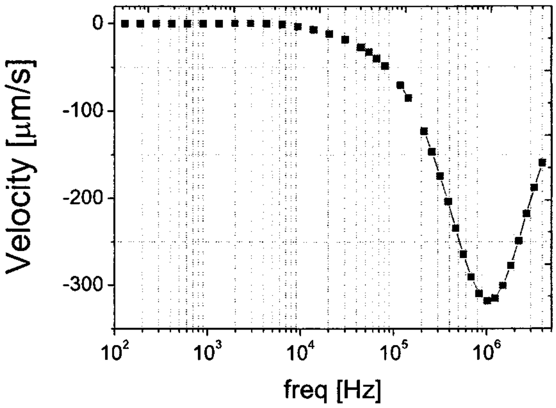

Figure 6.1: Net fluid velocity versus ω for a given constant flux on the electrodes ($-D(\mathbf{n} \cdot \nabla\sigma) = 2 \cdot 10^{-5}\sigma_0$). $V_0 = 2\,\mathrm{volts}$.

Fig. 6.1 shows the calculated net fluid velocity versus frequency, with parameter values shown in table 6.1. The value of the conductivity gradient at the level of the electrodes is given by the imposed flux $-D(\mathbf{n}\cdot\nabla\sigma) = \Gamma = 2\cdot 10^{-5}\sigma_0$ (S.I. units). This flux is of the order (or even higher) than that expected from experimental measurements. For this flux, the average conductivity in a 200 μm height channel would be 10 times higher after 100 s (as suggested by the observations in chapter 4). As shown by the figure, the vertical gradient in conductivity can only generate noticeable fluid flow for frequencies above 10^4 Hz, larger than the typical frequencies reported for pumping. The resistance value (charge transfer resistance R_{ct}) was parametrically changed within a wide range, but this had little influence on the results in Fig. 6.1. This is because, at the frequencies where this mechanism is important, the capacitive element of the impedance is so low that R_{ct} has little influence. At frequencies around the charge relaxation frequency (f$\sim$ 320 kHz for σ_0=1.5 mS/m), there is a phase lag between the field and the induced charge, so that the charge experiences a force and the liquid moves along the electrode array. At low frequencies the induced charge has sufficient time to follow the field vector without time delay and the time-averaged horizontal force is zero. The observation of flow reversal at 10 V_{pp} and 10 kHz for shallow channels may be related to this mechanism.

6.1.2 Longitudinal conductivity gradients

The typical frequencies required to generate net flow in the presence of a vertical conductivity gradient are high because a phase lag between the field and the induced charge is required. Nevertheless, the case of a spatial phase difference between an oscillating induced charge $\rho(\omega)$ and the electric field $\mathbf{E}(\omega)$ has not been discussed. Consider the situation shown in Fig. 6.2, where the conductivity changes periodically along the electrode array but is shifted a certain distance ($L\varphi/8\pi$) with respect to the "unit cell" of an electrode. The physical origin of such gradients in conductivity could be twofold: first, the electrical current through the electrodes may be strongly non-homogenous (contrary to the hypothesis in the previous section where flux was assumed constant along the electrode). Secondly, if fluid velocities are important, the convection of σ could generate spatial variations in conductivity. Therefore, for the sake of completeness, it is interesting to evaluate the influence of longitudinal gradients of conductivity on fluid flow. Both the conductivity and the spatial phase difference can depend on the applied signal in a complicated fashion. To analyze this mechanism, we assume that σ at the level of the electrodes is given by the expression in Fig. 6.2, and satisfies the diffusion equation in the bulk. This corresponds to a conductivity that varies smoothly along the electrode array, with a minimum value equal to σ_0. $\Delta\sigma$ is chosen to be small enough ($\Delta\sigma \ll \sigma_0$) so that the conductivity gradients are moderate. Note that the spatial period is chosen to be $T = L/4$; each electrode is equivalent and therefore we expect changes in conductivity to have the same spatial period. The term $(\varepsilon/\sigma)\partial\rho/\partial t$ in expression 6.2 is negligible for the typical frequencies used in the experiments and, therefore can be neglected. In this way, the effect of a spatial phase difference can be analyzed separately from that of a phase lag.

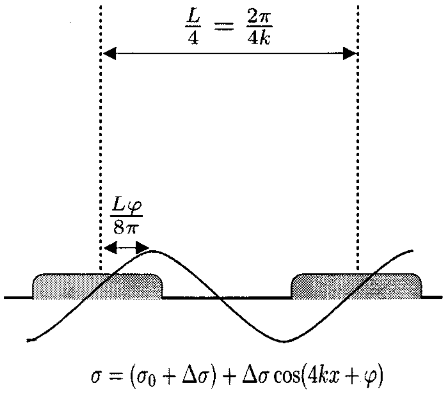

Figure 6.2: The conductivity at the level of the electrodes is supposed to change periodically along the array in order to evaluate the effect of longitudinal conductivity gradients. The picture corresponds to the case $\phi < 0$.

Fig. 6.3 shows the calculated net velocity versus the spatial phase difference φ for $\Delta\sigma/\sigma_0 = 0.1$, $V_0 = 2\,\text{volts}$, the typical frequency for ACEO, $\omega = k\sigma\lambda_D/\varepsilon = 2510\,\text{rad/s}$ and for two different values of $R' = \sigma_0 k R_{ct}$. Depending on the sign of the spatial phase difference, a net fluid velocity is obtained in one direction or the other. The case of $\varphi < 0$ corresponds to that depicted in Fig. 6.2. This conductivity profile would generate fluid motion in the same direction as the potential wave moves. On the other hand, if $\varphi > 0$ net fluid motion is generated in the opposite direction (flow reversal). Maximum velocities are found for a phase difference of $\pm\pi/2$. The fluid on an electrode flows towards the side with higher conductivity.

Longitudinal gradients of conductivity could be generated by non-uniform Faradaic reactions on the electrodes and/or by ionic concentration convection, although these mechanisms are not clear at present.

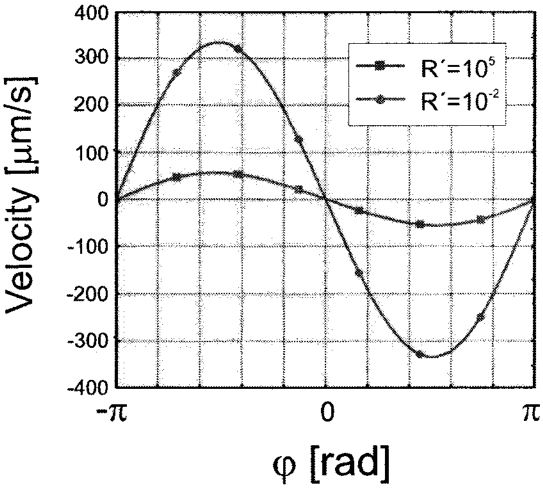

Figure 6.3: Net fluid velocity versus spatial phase difference φ for $\omega = k\sigma\lambda_D/\varepsilon$, $\Delta\sigma/\sigma_0 = 0.1$ and $V_0 = 2\,\text{volts}$.

6.2 Induced charge due to different ionic mobilities

The term $\sum_i ez_iD_i\nabla^2c_i$ in eq. 6.2 could yield net free charge $\rho = (\varepsilon/\sigma)\sum_i ez_iD_i\nabla^2c_i$ oscillating at ω. For a symmetric binary electrolyte, under the quasi-electroneutrality approximation $c_+ = c_- = c$, c satisfies the diffusion equation $\partial_t c = D_a\nabla^2 c$, where D_a is the ambipolar diffusion coefficient $D_a = 2(D_+D_-)/(D_+ + D_-)$ Newman & Thomas-Alyea (2004). Electrical charge is induced in a layer of typical thickness $\delta = \sqrt{D_a/\omega}$, i.e. the diffusion layer. For low voltages c can be written as $c = \text{Re}[\tilde{c}\exp i\omega t]$ with $\tilde{c}$ solution of:

$$D_a\nabla^2\tilde{c} = i\omega\tilde{c} \tag{6.7}$$

the typical length for c is δ and, for typical values of $D_a \sim 10^{-9}\,\text{m}^2/\text{s}$ and $\omega \sim 10^3\,\text{rad/s}$, the thickness of this layer is of the order of microns $\delta \sim 1\,\mu\text{m}$. Note that for a binary symmetrical electrolyte with equal diffusivities $D_+ = D_-$ (e.g. KCl), the induced charge is identically zero.

This force has been considered when describing the motion of a spherical particle on top of AC polarized electrodes (Sides (2001); Fagan *et al.* (2004)). A Faradaic current was supposed to flow through the electrodes. Our experiments with fluorescein show water reactions leading to a decrement in pH, i.e. an increase in H^+ concentration (chapter 4). Cl^- is the negative ion that provides electroneutrality when the concentration of H^+ increases. Since the mobility difference between the two is large $\mu_{H^+}/\mu_{Cl^-} = D_{H^+}/D_{Cl^-} = 4.6$, a considerable induced charge is to be expected. For simplicity, the calculations assume a binary electrolyte with this mobility ratio[1].

We calculate the fluid velocity generated by this mechanism for low applied voltages. It is assumed that the concentration of ions c does not change much $(|c - c_0|/c_0) << 1$ (c_0 is the bulk concentration) and consequently, the induced charge is expected to oscillate at ω, that is, $\nabla^2 \tilde{c}(\omega)/\tilde{c}(\omega) \simeq \nabla^2 \tilde{c}(\omega)/c_0$. Therefore, the time-averaged electrical body force is written as:

$$\langle \mathbf{f}(t) \rangle = -\frac{1}{2}\frac{\varepsilon k_B T}{e}\gamma \mathrm{Re}\left[\frac{\nabla^2 \tilde{c}(\omega)}{c_0} \cdot (\nabla \Phi)^*\right] \tag{6.8}$$

with $\gamma = (D_+ - D_-)/(D_+ + D_-)$

and the fluid velocity scales with the square of the applied voltage amplitude V_0. We have considered two ionic species (H^+ and Cl^-). The ionic concentration $\tilde{c}$ is solution of eq. 6.7 with boundary conditions on the electrodes (Sides (2003); Newman & Thomas-Alyea (2004))

$$\mathbf{n} \cdot \nabla \tilde{c} = \frac{J_F}{2eD_{H^+}} \tag{6.9}$$

where the Faradaic current J_F is due to electrochemical reactions of H^+. This boundary condition is correct if the displacement current is negligible compared with the Faradaic current, i.e. the flux of species in the diffusion layer is driven mainly by the Faradaic current (see section 6.2.1 below). This is a justified simplification for the present case because it is to be expected that Faradaic currents despolarize the interface. The Faradaic current is written as $J_F = \Delta\Phi/R_{ct}$, where $\Delta\Phi$ is the voltage

---

[1] For $[H^+] \gg [OH^-]$ the recombination in the bulk of these two ions can be neglected within distances of a few microns ($D_+ \nabla^2 c_+ \gg k_r c_+ c_-$, where k_r is the constant for recombination of ions in water)

drop through the EDL and R_{ct} is the resistance of the resistor in the Randles impedance. The electric potential is a solution of Poisson's equation written as:

$$\nabla^2\Phi = -\frac{k_BT}{e}\gamma\frac{\nabla^2\tilde{c}(\omega)}{c_0} \tag{6.10}$$

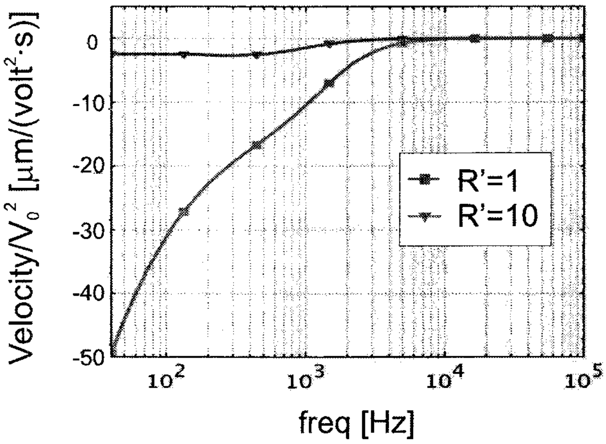

Figure 6.4: Net fluid velocity over the square of the voltage amplitude is plotted versus frequency for the case of induced charge due to two different ionic mobilities. It is considered $D_+/D_- = 4.6$, that is, $\gamma = 0.64$

Solving the Stokes equation with expression 6.8 as body force gives the velocity generated by this mechanism. Fig. 6.4 shows the net fluid velocity (scaled by the signal amplitude squared V_0^2) versus the frequency of the applied signal for two values of $R' = R_{ct}\sigma_0 k$. The other parameters in calculations are listed in table 6.1 (i.e. the parameters of the experiments described in chapter 4). The net velocity corresponds to flow reversal (a direction opposite to that of the TW). The calculations show that, when the more mobile ion undergoes chemical reactions, flow reversal is expected at typical frequencies of experiments.

In these calculations, $D_+/D_- = 4.6$, i.e. $\gamma = 0.64$. If $\gamma < 0$, this mechanism generates flow in the same direction as the travelling-wave. Since the H^+ ion is more mobile than Cl^-, this mechanism provides a good explanation for the flow reversal. In González *et al.* (2008b) preliminary analytical results were reported for the solution of the full linear electrokinetic equations considering a single mode travelling-wave and the effect of Faradaic charging and asymmetric mobilities. These analytical results are in agreement with the calculations presented here.

It is interesting to note that the frequency dependence of the net fluid velocity for the flow reversal in experiments is in good agreement with the calculations for $R' = 1$ in Fig. 6.4. The impedance measurements showed a strong decrement at low frequencies after application of signals that lead to flow reversal. The surface impedance became the same as the bulk resistance, that is, $R_{ct} \sim 1/\sigma k$. Therefore, we consider $R' = 1$ a reasonable value. Setting the signal amplitude V_0 to that typical for flow reversal (3.5-8 $\mathrm{V_{pp}}$), the experimental velocity values are smaller than the computed velocity values for $R' = 1$. This is satisfactory since we are not accounting for travelling-wave electroósmosis where net motion is generated in the other direction.

This mechanism is probably responsible for the flow reversal observed with electrode arrays driven by TW potentials. However, it is important to be aware that for the typical signal amplitudes of the experiments, the approximation of low voltages is not true and unrealistic values for $|c - c_0|$ would be obtained with the linear equations (electrical current would become greater than the diffusion limited current)[2]. Although the current is effectively limited, the term $\nabla^2 c/c$ is not bounded since c can approach zero. As the voltage increases, oscillations of c are greater and, consequently, the induced charge and the force due to the difference in ionic mobilities can be very high. Finally, it is worth considering the work by Gregersen *et al.* (2007) where flow reversal was observed in platinum asymmetric arrays at low voltage and frequency for higher concentrations (400 μM) than we normally use. That "unexpected" reversal could be related to the mechanism discussed here, since the electroosmotic motion decreases as concentration increases.

6.2.1 Boundary condition for the ionic concentration

In this section we demonstrate that boundary condition 6.9 is correct in the limit when the displacement current is negligible in front of the

---

[2] Note that this is a common feature with the linear and weakly nonlinear theories of ACEO (even in the case of perfectly polarizable electrodes). At typical voltages of the experiments the computed currents become so high that the perturbation analysis results to be inconsistent

Faradaic current. The ionic species fluxes are:

$$F_+ = -D_+ \frac{\partial c_+}{\partial z} - \mu_+ c_+ \frac{\partial \phi}{\partial z} \tag{6.11}$$

$$F_- = -D_- \frac{\partial c_-}{\partial z} + \mu_- c_- \frac{\partial \phi}{\partial z} \tag{6.12}$$

and the 1-D conservation equations of the species are written:

$$\frac{\partial c_+}{\partial t} = -\frac{\partial F_+}{\partial z} \tag{6.13}$$

$$\frac{\partial c_-}{\partial t} = -\frac{\partial F_-}{\partial z} \tag{6.14}$$

dividing eq. 6.13 by D_+ and eq. 6.14 by D_-, adding both results and integrating from the electrode ($z = 0$) to the end of the diffuse layer ($l \gg \lambda_D$), we obtain:

$$\int_0^l \left(\frac{1}{D_+} \frac{\partial c_+}{\partial t} + \frac{1}{D_-} \frac{\partial c_-}{\partial t} \right) \mathrm{d}z = \left(\frac{F_+}{D_+} + \frac{F_-}{D_-} \right)_{z=0} - \left(\frac{F_+}{D_+} + \frac{F_-}{D_-} \right)_{z=l} \tag{6.15}$$

If the cation is the reactive ion, at the electrodes $F_+ = J_F/e$, $F_- = 0$ and

$$\left(\frac{F_+}{D_+} + \frac{F_-}{D_-} \right)_{z=0} = \frac{J_F}{eD_+} \tag{6.16}$$

and outside the Debye layer $l > \lambda_D$, $c_+ = c_- = c$ and

$$\left(\frac{F_+}{D_+} + \frac{F_-}{D_-} \right)_{z=l} = -2\frac{\partial c}{\partial z} \tag{6.17}$$

Introducing $\rho/e = c_+ - c_-$ and $c = (c_+ + c_-)/2$, the left hand side of eq. 6.15 is

$$\int_0^l \left(\frac{1}{D_+} - \frac{1}{D_-} \right) \left(\frac{\partial \rho/e}{\partial t} + 2\frac{\partial c}{\partial t} \right) \mathrm{d}z \tag{6.18}$$

the second term is always smaller than $\partial c/\partial z$ because it is of the order of $\omega c \lambda_D / D_a$ and $\partial c/\partial z$ is of order of c/δ. The first term is of the order of $q\omega/eD_+$, where q is the surface charge in the diffuse layer. In the case that $q\omega/eD_+ \ll \partial c/\partial z$, the boundary condition 6.9 is correct, (6.16)=(6.17). That is, when the displacement current $\omega q \ll eD_+ \partial c/\partial z = J_F/2$.

6.3 Conclusions

The experimental results in the previous chapters led us to explore possible pumping mechanisms where the electrical forces are located beyond the Debye length. Induced charge due to Faradaic currents could appear in the electrolyte bulk and generate net flow. We have modelled this effect for the TW array and calculated fluid velocities for example cases in order to discuss the possible influence of different mechanisms. When a vertical conductivity gradient is present, the generated velocity for typical signals is negligible at frequencies much smaller than the relaxation frequency of the electrolyte (corresponding with the typical frequencies of the reported motion) but could be important above 10 kHz. Observations of flow reversal in shallow channels may be related to this. Longitudinal conductivity gradients could give rise to large net velocities. These longitudinal gradients of conductivity could be generated by non-uniform Faradaic reactions on the electrodes as well as ionic concentration convection, although these mechanisms are not clear at present. Finally, the induced charge due to the difference in mobilities between ionic species seems to be important and qualitatively explains the flow reversal previously reported. Further theoretical studies are required in order to analyze this mechanism for different voltage amplitudes and concentrations, i.e. an analysis beyond the linear approximation.

Chapter 7

Electrode height effect on TWEO micropumps

The optimal design of the microelectrode structure is still a matter of current research (Olesen (2006)). Although experiments reported with planar electrode structures showed that achieving higher velocities can be obtained by increasing the voltage, undesired effects can appear as the voltage is increased (electrolysis, electrode degradation, hydrodynamic instabilities). We consider that keeping the applied voltage as low as possible is a goal that must be pursued.

It has recently been found, theoretically by Bazant & Ben (2006) and experimentally by Urbanski *et al.* (2006), that the pumping effect of the asymmetric array can be improved by fabricating 3-D electrode structures. Urbanski *et al.* (2007) reported an experimental study of the dependence of the velocity of the array of asymmetric pairs on step height, they also performed further simulations for comparison but not all experimental observations are captured by the theoretical modelling. Nevertheless, they concluded that interesting predictions may still be carried out in order to obtain higher pumping velocities.

In chapter 3 we demonstrated that the TWEO array is more efficient than the asymmetric pairs array in the sense that higher velocities can be achieved with lower voltages. In this chapter, an enhancement of the TWEO array performance is theoretically demonstrated: the net pumping velocity can be increased up to 2.7 times if the electrodes are raised above the channel bottom. In a travelling-wave array, all electrodes are pumping the liquid in the same direction (they are all equivalent). Therefore, the increase in the net fluid velocity is interpreted as a strong reduction of the viscous friction at the walls. Since electrical stresses are applied at the electrode-electrolyte interface, the non-slip boundary condition at the interelectrode gaps is remarkably affecting the flow velocity in planar structures. As the electrodes are raised, the viscous friction is drastically reduced and there is an optimum for the electrodes height.

We check this result with the standard theory of ACEO for blocking electrodes (Ramos *et al.* (1999a); González *et al.* (2000)), the maximum velocity is achieved for a *non-dimensional electrode height of 0.40.* We have also used the more general theory in chapter 5 accounting for Faradaic currents in the linear regime. In this case, the optimum dimensional height is dependent on the parameters of the model although it is slightly greater than in the case of blocking electrodes and the velocity is, generally, around 2.7 times larger than for planar structures.

Finally, we perform a comparison with previous results for the asymmetric step electrode array and the maximum velocity for the 3D travelling-wave array is found to be roughly twice that for the asymmetric step array.

7.1 Mathematical analysis

Translational symmetry transverse to the flow direction is assumed and, therefore, only two-dimensional simulations are performed. We make use of a rectangular domain, electrodes are placed at the bottom and the height of them is changed as a parameter. The corners of the electrodes are rounded, representing a better approximation to real boundaries and avoiding numerical difficulties (Urbanski *et al.* (2006)). We first compute the electric potential in the whole domain and then derive the electroosmotic velocity at the electrodes from the *Helmholtz-Smoluchowski* formula. Finally, the Stokes flow problem is solved including the electroosmotic velocity as boundary condition on the electrodes.

7.1.1 Electrostatic Problem

The electric potential is given by $\phi = \mathrm{Re}[\Phi \exp(i\omega t)]$, where Φ is a phasor satisfying the Laplace equation $\nabla^2\Phi = 0$. We follow Ramos *et al.* (2005) and compute Φ as $\Phi_1 + \Phi_2$, where Φ_1 and Φ_2 are the solutions to the problems in Figs. 7.1a) and 7.1b), respectively. In this way, we solve the Laplace equation twice but the computational domain reduces eight times. The polarization of the electrode-electrolyte interface is modelled by means of a surface impedance Z. The general boundary condition on the electrodes is then

$$\Phi - \sigma Z(\mathbf{n} \cdot \nabla\Phi) = V \tag{7.1}$$

where σ is the liquid conductivity and V the applied voltage. On the gap between electrodes, the boundary condition corresponds to zero normal current $\mathbf{n} \cdot \nabla\Phi = 0$.

We make use of two different models for Z. One is the capacitor model for perfectly blocking electrodes in which the impedance is $Z = 1/i\omega C$. For a negligible Stern layer (Hunter (1993)), C is estimated from the *Debye-Huckel* theory as $C = \varepsilon/\lambda_D$ (λ_D is the debye length and it is related to the diffusion coefficient by $\lambda_D = \sqrt{D\varepsilon/\sigma}$). The other is a more complex model accounting for Faradaic currents under the

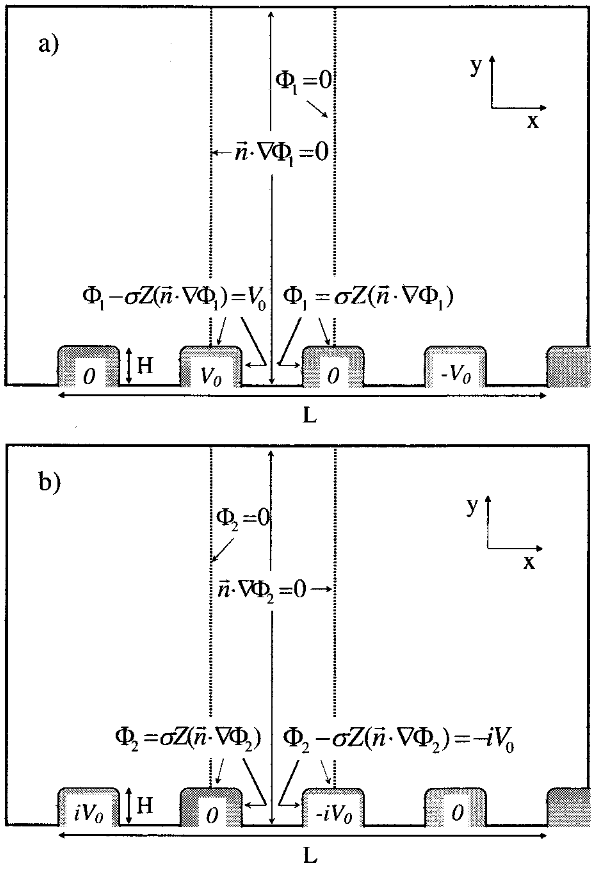

Figure 7.1: Problem domain

linear approximation (chapter 5, Ramos *et al.* (2007)). In this case the impedance corresponds to that of the *Randles* circuit, Fig.7.2:

$$Z = \frac{R_{ct} + W/\sqrt{i\omega}}{1 + i\omega R_{ct}C + CW\sqrt{i\omega}} \tag{7.2}$$

$W/\sqrt{i\omega}$ is known as the *Warburg* impedance and R_{ct} is the charge transfer resistance (Bard & Faulkner (2001)). Note that for either $R_{ct} \to \infty$ or $W \to \infty$, Faradaic currents go to zero and we recover the expression for blocking electrodes.

7.1.2 Dynamic Problem

The fluid velocity is governed by the Stokes equations in the absence of volume forces

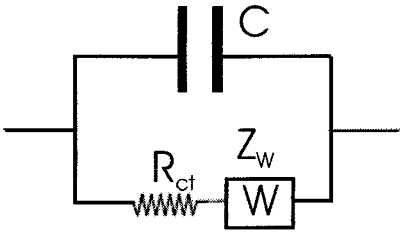

Figure 7.2: Randles impedance

$$
\begin{aligned}
\nabla \cdot \mathbf{u} &= 0 && (7.3)\\
-\nabla p + \eta \nabla^2 \mathbf{u} &= 0 && (7.4)
\end{aligned}
$$

where $\mathbf{u} = u\mathbf{e}_x + v\mathbf{e}_y$ is the velocity field and p the pressure.

We solve these equations with the following boundary conditions:

On the electrodes we consider a slip velocity given by the time average of the Helmholtz-Smoluchowski electrosmotic velocity Hunter (1993) $u_{eo} = \epsilon/\eta\langle\zeta E_t\rangle$. Here ζ is the zeta potential, i.e. the voltage drop through the diffuse layer at the electrode-electrolyte interface, and E_t is the component of the electric field tangential to the electrode.

In terms of the phasor of the electric potential Φ, the time-averaged electroosmotic velocity can be written as

$$u_{eo} = -\frac{\varepsilon}{2\eta}\mathrm{Re}[(\Phi - V)\nabla\Phi^* \cdot \mathbf{t}\,] \qquad (7.5)$$

where $\mathbf{t}$ is a unit vector tangential to the electrode surface. The normal velocity v on the electrodes is zero.

On the gap between electrodes the fluid has zero velocity (non-slip condition). Periodic boundary conditions are required at the left and right boundaries. Finally at the top of the channel we impose neutral boundary conditions (the stress tensor equals zero). The top of the channel is a free surface of the liquid at a distance much larger than the electrode and flow vortex sizes. The velocity is homogeneous there ($\mathbf{u} = u\mathbf{e}_x$ with $\partial u/\partial y = 0$) and represents the net effect of the array as a micropump. In this way, the results can easily be compared to previous ones.

7.2 Results

Theoretical fluid velocities are computed with *Comsol*, a commercial software implementing the finite element method. It is convenient to define nondimensional quantities in order to explore the influence of the different parameters. The characteristic angular frequency for AC electroosmosis is given by $\sigma\lambda_D/\varepsilon l$, where l is a characteristic dimension of the system (Ramos *et al.* (1999a); Cahill *et al.* (2004); Ramos *et al.* (2005)). In the present problem, the inverse of the wavelength $k^{-1} = L/2\pi$ is chosen as a scale for distances and, therefore, $\sigma k\lambda_D/\varepsilon$ is used for scaling angular frequencies, $\Omega = \omega\epsilon/\sigma k\lambda_D$. Velocities are scaled with $\varepsilon k V_0^2/2\eta$. We define a nondimensional impedance as $Z' = \sigma k Z$ ($1/\sigma k$ is the bulk specific resistance). For perfectly blocking electrodes, the nondimensional impedance is $Z' = 1/i\Omega$. For the *Randles impedance* we define $R' = \sigma k R_{ct}$ and $W' = W\sqrt{\sigma k\varepsilon/\lambda_D}$ and then $Z' = (R' + W'/\sqrt{i\Omega})/(1 + i\Omega R' + W'\sqrt{i\Omega})$.

In Fig. 7.3 we show the non-dimensional velocity at the top of the channel versus the electrode height in the case of perfectly blocking electrodes. We name it *pumping velocity U* since it corresponds to the average velocity generated by the electrode array and can be compared with the net velocity achieved with planar structures.

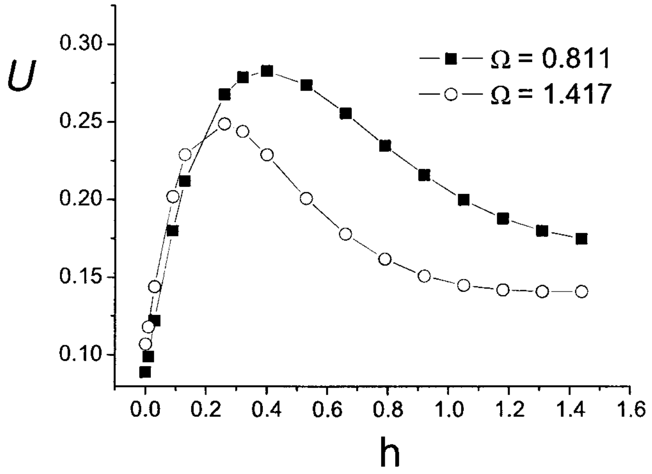

Figure 7.3: $U = u2\eta/\varepsilon k V_0^2$ versus $h = kH$. Blocking electrode case.

It is observed that the average velocity is very sensitive to the electrode height. Maximum velocity is obtained for $\Omega = 0.81$ and $h = 0.4$, that is, for a height corresponding to approximately half the electrode width, $h \simeq kL/16 = 0.393$. The non-slip boundary condition at the gap between electrodes imposes an obstacle to the fluid pumped by the electrodes. Figure 7.4 shows the streamlines at $\Omega = 1.417$ for a planar array and an array with $h = 0.4$. As the electrodes are raised, the hindrance effect of the non-slip condition is drastically reduced.

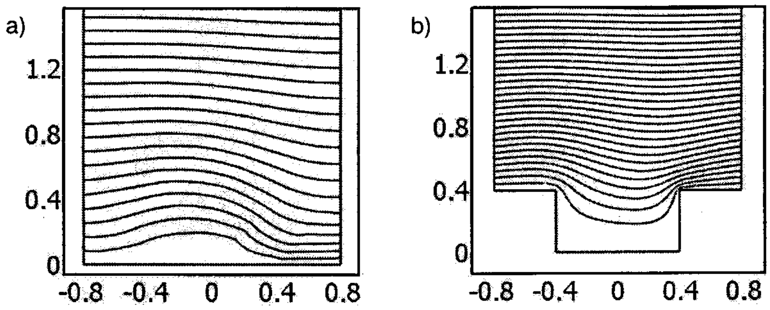

Figure 7.4: a) Streamlines for a planar array. b) Streamlines for $h = 0.4$. ($\Omega = 1.417$)

Fig. 7.5 shows the *pumping velocity* versus angular frequency Ω at several electrode heights. For $h = 0.03$ it is very clear the enhancement in the pumping velocity (and it is only half a micron height for a typical array of $L = 100\,\mu\text{m}$). The pumping velocity is maximum for $h = 0.4$ and it is 2.65 times greater than for the planar structure ($h = 0$). As the electrode height h increases, the frequency for maximum velocity decreases. The characteristic charging time of the RC equivalent circuit is changed since the capacitance of the system increases as the vertical walls of the electrode rise. This explanation has been confirmed by computations where the vertical walls were considered insulators (like the gap between electrodes). In that case, the velocity was maximum at $\Omega = 1.417$ for all electrode heights. Furthermore, in the case of insulating vertical walls, we do not find a maximum at $h = 0.4$ but a constant pumping velocity for $h \geq 0.4$.

Fig. 7.6 shows the *pumping velocity* versus Ω for a Randles impedance with $R' = 0$ and $W' = 0.3$. Typical frequencies are lower than in the blocking electrode case and velocities decrease, that is what we expect from previous results with planar arrays where the Randles impedance was used (Ramos *et al.* (2007)). The absolute maximum velocity is obtained for $h = 0.50$ at $\Omega = 0.029$, and it is 2.60 times greater than for $h = 0$. Finally, in figure 7.7 we show the *pumping velocity* versus Ω for a Randles impedance with $R' = 0.1$ and $W' = 0.1$. Maximum velocity is found for $h = 0.65$ and it is 2.73 times larger than for $h = 0$.

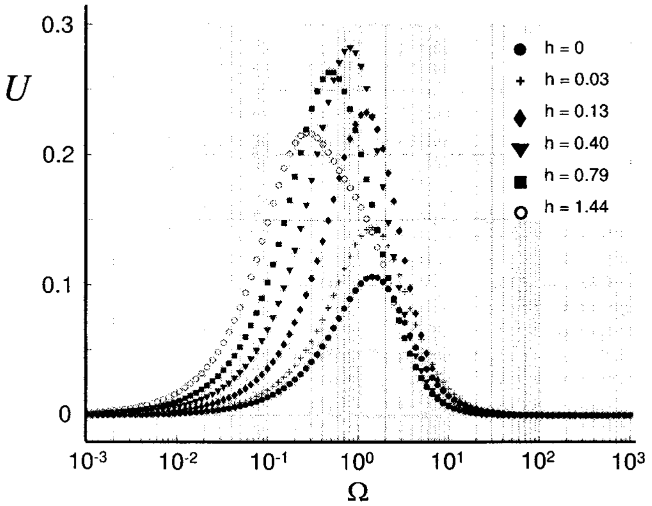

Figure 7.5: $U = u2\eta/\varepsilon k V_0^2$ versus $\Omega = \omega\varepsilon/\sigma k \lambda_D$ at several electrode heights $h = kH$. Blocking electrode case.

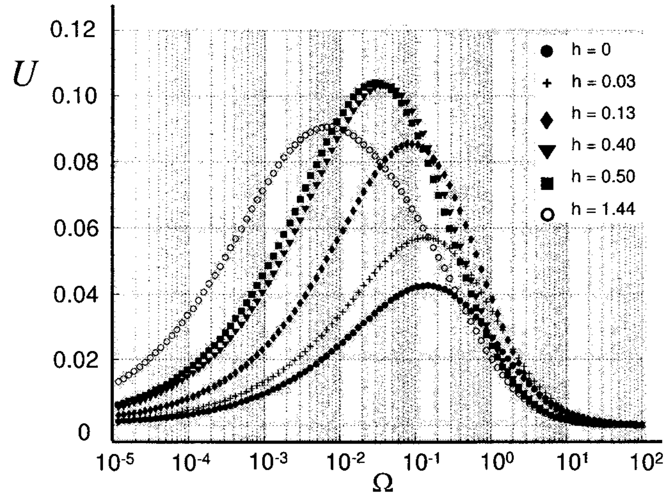

Figure 7.6: U versus Ω at several electrode heights $h = kH$. Randles impedance with $R' = 0$ and $W' = 0.3$.

7.3 Conclusions

It has been carried out a numerical study of the effect of electrode height in the pumping of electrolytes with a travelling-wave potential of four phases. Two linear models for the polarization of the electrode-electrolyte interface has been used: a simple capacitor model and a more general *Randles Impedance*. The net pumping effect of the array is improved

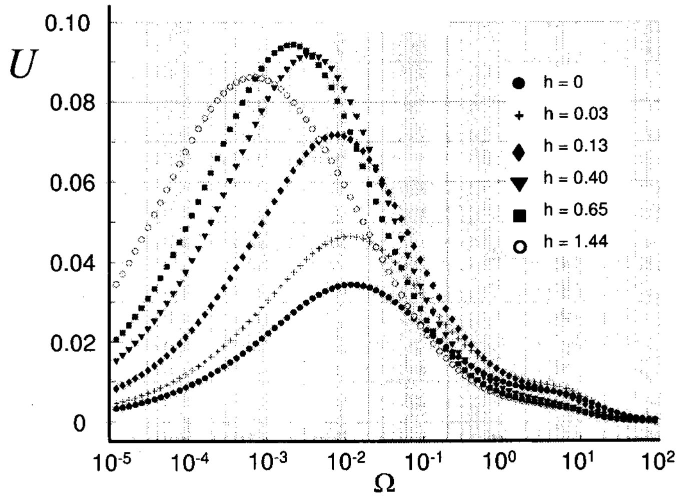

Figure 7.7: U versus Ω at several electrode heights $h = kH$. Randles impedance with $R' = 0.1$ and $W' = 0.1$.

as the electrodes are raised since the friction at the electrode gap is reduced. Streamlines clearly show how the fluid motion is less distorted if we lower the walls where the non-slip condition for the fluid velocity applies. We conclude that the reduction in viscous friction must be a general aim when performing optimizations of 3D electrode structures. For the present case of a four-phase travelling-wave, computations show that the 3D array can generate velocities up to 2.7 times larger than the planar structures. The electrode height must be equal or slightly larger to half the electrode width $h \gtrsim 0.4$.

We have also compared with velocities generated by 3D asymmetric arrays. For the comparison, we make use of the results in chapter 5 of ref. Olesen (2006). In section 5.3 of this work, an optimization of the step geometry is performed for the case of perfectly blocking electrodes. This step electrode design was first suggested by Bazant & Ben (2006). We have repeated the velocity computation for the optimum geometry, see Fig. 7.8. We have reproduced the velocity value $u = 0.0566\varepsilon V_0^2/\eta l$, where l is the minimum feature size of the electrode structure (the gap width in this case). According to Bazant & Ben (2006), for a fair comparison between different designs we should fix the minimum feature size and the total applied voltage to each electrode. For the 3D TW array, in the case of perfectly blocking electrodes, we have found a maximum dimensional velocity $u = 0.282\varepsilon k V_0^2/2\eta = 0.111\varepsilon V_0^2/\eta l$, where l is the gap width. Therefore, the maximum velocity obtained with the 3D TW array is 1.96 times that of the optimum design of the asymmetric steps. Note

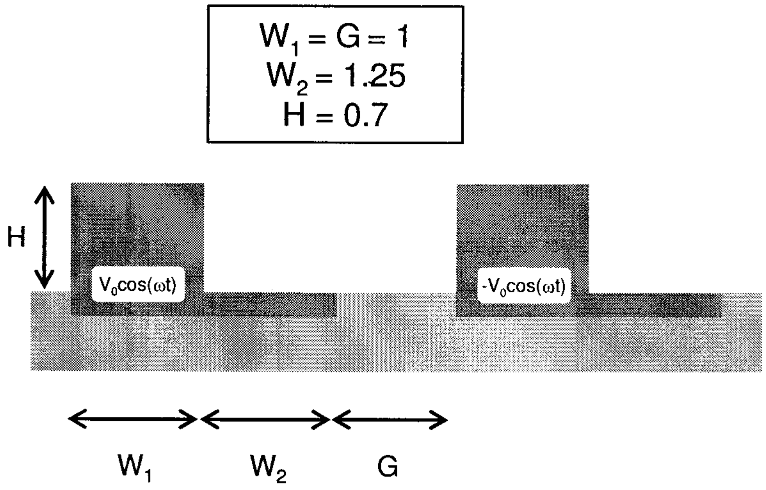

Figure 7.8: Step geometry optimized in Olesen (2006).

that the gap and electrode sizes of the TW array were not optimized. For the planar TW array the maximum velocity is 2.8 times lower than for the 3D TW array, this means that the 3D asymmetric step array is not much more efficient than the planar TW array, which is simpler to fabricate (the maximum velocity for the planar TW array is ~0.7 that of the 3D asymmetric array). On the other hand, the asymmetric arrays can be powered by just a simple function generator providing one single AC signal, while the TW array requires four AC signals with different phases.

Conclusions and outlook

Fluid flow in microsystems induced by travelling-wave potentials has been studied. The flow behaviour has been described with a 2-D map where the velocity is plotted versus voltage and frequency. At low voltages, the fluid flows in the direction predicted by the AC electroosmosis theory (*normal pumping*). For a certain voltage, that depends on frequency, the fluid flow reversed (*reverse pumping* or *flow reversal*). This result was found with microelectrode arrays made from two different metals (platinum and titanium) and arrays with two different electrode sizes ($20\,\mu$m and $10\,\mu$m). Non-uniform motion was observed with the platinum arrays for low frequencies and high voltages. Electrolytic bubble generation was observed for sufficiently high voltage and low frequency. We related these observations of nonuniform motion to flow instabilities that are likely to be induced by the generation of gradients in ionic concentration. With titanium arrays only electrolysis of water was observed at low frequencies and high voltages.

Flow reversal has always been found regardless of channel height, array shape and size and electrolyte conductivity. However, the threshold voltage depends on the channel height and electrolyte conductivity. For shallow channels, it was found that higher voltages and frequencies were required for observing the flow reversal. When the electrolyte conductivity was increased, higher voltages were also required. Both observations are compatible with the hypothesis that the flow reversal is generated by forces beyond the Debye layer.

The electrical impedance of the electrode-electrolyte system was measured before and after the experiments and it was found a strong decrease in the system impedance. Measurements of the electrical current during pumping showed transient behaviour. At specific voltages, around the threshold voltage, simultaneous measurements of fluid velocity and electrical current showed a strong correlation. Faradaic currents are responsible for this transient behaviour and for the generation of gradients in conductivity. When DI water was used, the results were similar, indicating that electrochemical reactions of water could be responsible for the observations. These results were supported by the observations with fluorescent dyes which indicated that electrochemical reactions occur at the electrodes, leading to a pH decrement as well as concentration polarisation oscillating with the frequency of the applied signal.

From these observations we conclude that the theoretical models should not ignore these changes in liquid properties. Faradaic currents occur and the measurements showed them to be correlated to the fluid flow observations. Conductivity gradients are generated and they can induce electrical forces in the electrolyte bulk.

The effect of Faradaic currents in the charging of the double layer was modelled in the linear regime for the case of equal ionic mobilities. The results represented a generalisation of the AC electroosmosis theory. It was found that the fluid velocity can be written as a function of the total voltage drop across the EDL. The results do not account for the flow reversal but provide a more general theory for explaining the measurements at low voltages. It was found that, when Faradaic currents are included, the electroosmotic velocity is reduced because the double layer depolarizes.

Forces in the bulk due to gradients in ionic concentration have also been analysed. We discuss some situations where these forces lead to net electrolyte pumping. When a vertical gradient is present, the generated velocity for typical signals is negligible at frequencies much smaller than the relaxation frequency of the electrolyte but could be important above 10 kHz. We have found that longitudinal ionic concentration gradients could give rise to large net velocities. These gradients could be generated by non-uniform Faradaic gradients on the electrodes and/or by ionic concentration convection, although these mechanisms are not clear at present. The induced charge due to the difference in ionic mobilities was also studied. The observed strong decrease in pH means a net production of H^+. Since the mobility difference between H^+ and Cl^- is large (μ_{H^+}/μ_{Cl^-}=4.6), a considerable induced charge is to be expected. We have made numerical computations assuming a binary electrolyte with that mobility ratio. Low applied voltages were supposed and the results qualitatively explain the *flow reversal*. However, it is important to be aware that, for the typical signal amplitudes of the experiments, the approximation of low voltages is not true and unrealistic values of the ionic concentration would be obtained with the linear equations.

The travelling-wave array and the asymmetric pairs array were compared. Both experiments and theory showed that, for equal sized electrodes and same voltage amplitude applied to each electrode, the net velocity generated by the travelling-wave array is higher. This is also true for the 3-D structures studied in chapter 7.

Future work is focused on a rigorous mathematical modelling of the flow induced by the ionic concentration gradients generated by Faradaic currents. From the experimental point of view we plan to work with other geometries/systems in order to evaluate the validity of the theoretical models. In this way, the importance of forces beyond the double layer will also be tested in other systems of interest for the Lab-on-a-Chip.

Electrohydrodynamic instabilities were beyond the scope of the thesis. However, observations for TW signals of high amplitude and low frequency showed non-uniform motion. Induced charge in the bulk can also be origin of electrohydrodynamic instabilities in microsystems. Further experimental and theoretical work is planned in order to explain these observations.

Despite the flow at low voltage can be understood with the current theory for AC electroosmosis, we are still far from making quantitative predictions for the fluid velocity. Experimental velocities are smaller than those predicted from the theory. Theoretical models that include the effect of the finite size of the ions (steric effects) could explain this velocity reduction. Another effect to be accounted for is that the position of the shear plane could be beyond the Outer Helmholtz Plane due to the existence of a hydrodynamic stagnant layer, which reduces the "effective" zeta potential. Future work is also focused on a better description of the electrode/electrolyte interface.

Appendices

Appendix A

Control of two-phase flows by AC electric fields[1]

---

[1] This appendix has been published in its present form in: *Applied Physics Letters* **91**, 254107 (2007)

Dynamic control of fluids is important in Lab on Chip (LoC) technology, and MEMS devices are often used for this (Koch *et al.* (2000)). However, such devices are complicated to construct and cannot be easily integrated into the LoC. Solid-state control of liquids using DC electric fields has also been widely used to manipulate fluids, particularly with capillary electroosmosis. However, the high voltages required produce electrolysis and the electrodes must be placed outside the device to reduce the effects of Joule heating and gas bubbles. Electroosmosis has been used in the LoC to enhance mixing of fluids (Oddy *et al.* (2001); Glasgow *et al.* (2004)); reduce diffusion (sample stacking) (Jacobson & Ramsey (1995)); switch fluid streams (Fu *et al.* (1999)); and focus flows (Jacobson & Ramsey (1997)).

AC electric field-induced fluid flow can also be used to move fluids and analytes (Ramos *et al.* (1998); Bazant *et al.* (2004); Sasaki *et al.* (2006); Zhao & Bau (2007)), and produce mixing by stirring (Sasaki *et al.* (2006)). AC-based systems have many advantages, including lower power requirements, simple integration and little or no electrolysis issues. Fluid is driven and controlled using microelectrodes that are fabricated within microchannels. The electrohydrodynamic forces produced by the AC fields act either on the bulk fluid, (e.g. electrothermal flow (Ramos *et al.* (1998)), or the double layer at the solid-electrolyte interface, AC electroosmosis (Ramos *et al.* (1998)). In this letter we describe a new way of controlling the behaviour of two co-flowing streams of electrolytes in a microfluidic system using AC electric fields generated by a microelectrode array.

The experimental arrangement consists of a micro-device with microelectrodes fabricated on a planar glass substrate, fig. A.1. The electrodes are made from Pt, and are 200 nm thick, manufactured using ion beam milling of the metal. They have a width and gap of 20 m. The microfluidic channel width is 1 mm and has a height of 100 m and is fabricated from a photosensitive laminate resist. The channel is closed with an upper glass layer and the finished device clamped to seal the system. The electrodes have a chevron pattern (figure A.1). An AC potential difference is applied to each alternate electrode, producing an electric field at the boundary of the two fluids along the length channel. AC signals (< 20 V) were applied using signal generators with frequencies high enough to avoid electrode polarization and electrolysis.

Two different electrolytes are pumped across the electrodes as shown in figure A.1. Solutions of KCl with different conductivities were used,

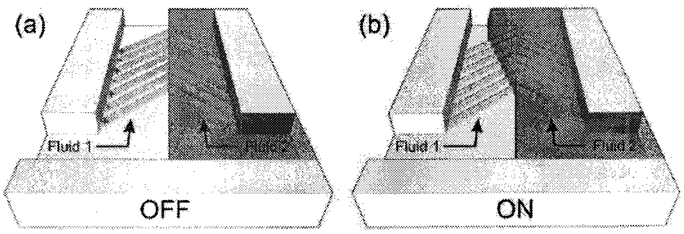

Figure A.1: Diagram of the experimental chip showing the two coflowing fluid streams before and after application of the electric field. The electrode array is on the bottom of the channel and each alternate electrode is connected to a single phase voltage supply.

one ten times higher than the other. The KCl with the higher conductivity also contained a dilute solution of carboxy-fluorescein, which enabled discrimination of the two separate flows and the boundary between them. When a single phase AC potential was applied to the electrodes it was observed that the boundary between the two fluids moved, as shown schematically in figure A.1. Two images from the device showing this effect are reproduced in figure A.2 [2]. These data were obtained with an applied signal of 20 V (peak to peak) at a frequency of 1 MHz, with electrolyte conductivity of $\sigma_1 = 15\,\mathrm{mS/m}$ and $\sigma_2 = 1.5\,\mathrm{mS/m}$.

When the voltage was applied, the boundary between the two fluids moved to the region of lower conductivity, within a few tens of msec after applying the potential. This boundary then remained fixed along the entire length of the channel downstream, even after the electrode array had ended (figure A.1). When the voltage was switched off, the fluid returned to the steady-state position. This effect was observed for frequencies around 1 MHz, but when the frequency of the applied signal was increased to 10 MHz, the effect was no longer seen. Changing the electrolyte conductivities to $\sigma_1 = 15\,\mathrm{mS/m}$ and $\sigma_2 = 1.5\,\mathrm{mS/m}$ greatly reduced this effect, but a small deviation in the boundary was still seen. Changing the voltage altered the position of the boundary. At voltages less than 5 V, little effect was observed. As shown in figure A.2, with 20 V applied the high conductivity liquid almost occupied the entire width of the channel. This data was obtained with a volume flow rate of 0.3 l/s,

---

[2] See EPAPS Document No. E-APPLAB-91-020452 for a video showing the movement of fluid when the field is applied. This document can be reached through a direct link in the online article's HTML reference section or via the EPAPS homepage (http://www.aip.org/pubservs/epaps.html)

equivalent to an average fluid velocity of 2 mm/s.

The electrical body forces on a liquid are described by the following equation (Stratton (1941))

$$\mathbf{f}_e = \rho_q \mathbf{E} - \frac{1}{2}\mathbf{E}^2 \nabla \varepsilon + \frac{1}{2}\nabla \left[\rho_m \left(\frac{\partial \varepsilon}{\partial \rho_m} \right) \mathbf{E}^2 \right] \tag{A.1}$$

where ρ_q is the charge density, ρ_m the mass density, ε the permittivity, T the temperature and $\mathbf{E}$ the magnitude of the electric field. The first and second terms are the Coulomb and dielectric forces, respectively, and the last term is the electrostriction force, which can be ignored for incompressible fluids (Stratton (1941)). For the system described here, the dielectric term is zero because both liquids have the same permittivity. Electrolytes are overall neutral (no excess free charge); and the Coulomb force acts on the free charge at the interface between the liquids. Therefore, the electric field at the boundary creates a force which displaces one liquid with respect to the other. The free charge is induced by the electric field, which also is responsible for the force. Therefore, the time average force is non-zero and scales with $\mathbf{E}^2$.

The behaviour of the liquid is in many ways analogous to the behaviour of a polarisable particle in a non-uniform electric field - a phenomena known as Dielectrophoresis (DEP) (Pohl (1978); Morgan & Green

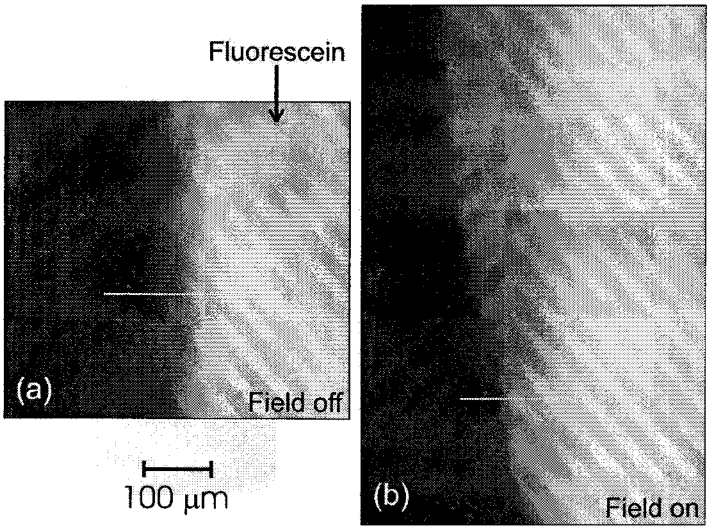

Figure A.2: Experimental images of the two electrolyte streams: (a) before and (b) after application of 20 V peak to peak at 1 MHz. Note that the deflection continues downstream after the electrode array finishes.

(2003)). At low frequencies, the free charge dominates, but as the frequency increases the permittivity dominates because there is no time for charge to accumulate at the interface. Therefore, as in DEP, permittivity effects are predominant at high frequencies and for two fluids of identical permittivity the force is zero. At low frequencies free charge dominates and the liquid with higher polarisability (the higher conductivity) tries to maximize the electrical energy of the system (at constant potential) and occupies the region of high electric field, as observed in these experiments.

For the two fluids used in this work, the relaxation frequency of the interfacial free charge is Pohl (1978):

$$f_2 = \frac{1}{2\pi}\frac{d_1\sigma_2 + d_2\sigma_1}{d_1\epsilon_2 + d_2\epsilon_1} \tag{A.2}$$

where d is the thickness of the dielectric. In this case $d_1 = d_2$ and $\sigma_1 = \sigma_2$ so that $f_2 = 1.85\,\text{MHz}$. Therefore, for frequencies much greater than f_2, the force is negligible, but for frequencies much lower than f_2, the force is constant. Our experiments concur with this simple estimation. The magnitude of this force scales with the difference in conductivity of the two liquids, according to $(\sigma_2 - \sigma_1)/(\sigma_2 + \sigma_1)$. For the two conductivities shown in fig. A.2, the factor is 0.82, but for the two samples of nearly equal conductivity the factor is only 0.14, i.e. the force is much reduced. The two fluids were driven by gravity. Changing the height of the fluid reservoirs by the order of 1 mm corresponds to a hydrostatic pressure of the order of 10 Pa. This pressure change was enough to produce an observable change in the position of the interface. For a voltage of 20 V_{pp}, the time-average electrical pressure in the system can be estimated to be approximately 40 Pa, which is more than enough to cause the deflection observed.

Interestingly, fig. A.2 also shows that when the field is applied, the boundary between the two fluids is compressed and better defined. Upstream of the electrodes, the boundary is broad due to diffusion of the fluorescent dye into the liquid, but over the electrodes the boundary becomes narrower. Fig. A.3(a) shows a profile of the light intensity (proportional to concentration of fluorescein) across the interface before and after application of the voltage, determined along the lines (200 μm long) shown in fig. A.2. Fig. A.3(b) shows that the intensity profile (with the voltage off) is well matched by the theoretical (normalized) concentration (of fluorescein) calculated from the diffusion equation. The observation point was 3.1 mm from the junction of the two fluids (diffusion time of 1.5 s), and the curve was calculated using a diffusion constant for fluorescein of $4 \cdot 10^{-10}\,\text{m}^2/\text{s}$ (Culbertson *et al.* (2002)). When the voltage is

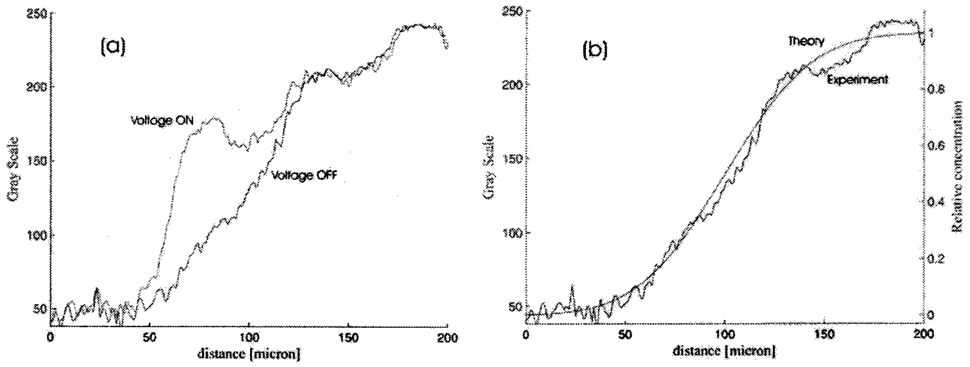

Figure A.3: Profiles of the light intensity across the interface: (a) with and without electric field; (b) comparison of the experimental concentration profile and the theoretical profile (without field).

applied the profile across the boundary changes markedly, as shown in fig. A.3(a), appearing to reduce the effect of diffusion.

Although DC fields have been used to limit the diffusion of charged species (Jacobson & Ramsey (1995)), this has not been previously observed with AC fields. The origin of this effect is not clear at present, but may be related to the polarization of the interface.

In conclusion, we have demonstrated that applying an AC electric field across the boundary of two electrolytes with different conductivities in a microchannel, generates a force at the interface that alters the position of the boundary. We have shown qualitative agreement between experiment and theory in terms of frequency and voltage dependence. Further work is required to quantitatively characterize these phenomena. The ability to actively deflect fluids within a micro-system has many technological applications, for example active solid-state deflection of streams into different outlets for sorting or analysing of particle and analytes. The phenomenon could also be used to rapidly switch different fluid stream to different sensing points, allowing multiple analysis steps to be performed in a single microfluidic channel. Dynamic control of flow focusing of fluids should be possible, in a manner analogous to DEP-focusing of particles along the centre of a channel (Morgan *et al.* (2003)). With a high voltage ($\sim 40\,\mathrm{V_{pp}}$), electro-hydrodynamic instabilities were produced at the boundary which could be exploited to drive chaotic mixing, as demonstrated for DC fields (Oddy *et al.* (2001)).

Appendix B

Flow of electrolytes induced by AC voltages in a point-plane electrode microsystem[1]

---

[1] This appendix has been published in its present form in: ICDL 2008. IEEE International Conference on Dielectric Liquids, 2008.

B.1 Introduction

Electrohydrodynamics (EHD) in microsystems is receiving a growing interest because of the extensive research in microelectromechanical systems (MEMS) and the Lab-on-a-Chip technologies (Stone *et al.* (2004); Ramos (2007)). Electric fields are a key tool for the manipulations of liquids at the micrometer scale. For example, electroosmosis requires relatively low voltages for dragging fluids at solid-liquid interfaces. Nevertheless, as the dimensions are reduced and the voltage is increased, new phenomenology appears. The standard electrokinetic theory is not sufficient to describe the full behaviour of aqueous solutions subjected to electric fields at the microscale. Several experimental observations are lacking of a theoretical explanation. In particular, the fluid flow generated by AC electrokinetic micropumps (Studer *et al.* (2004); Cahill *et al.* (2004)) is correctly described by the theory of AC electroosmosis (Ramos *et al.* (1999a, 2007)) when the applied voltages are sufficiently low (<2 V_{pp}) and the electrodes behave as a perfectly polarisable surface. These micropumps are based on arrays of microelectrodes subjected to ac potentials. The theory predicts pumping in a certain direction but in the experiments this direction reverses under certain conditions (Studer *et al.* (2004); García-Sánchez *et al.* (2006); Gregersen *et al.* (2007)).

Despite the low applied voltage to the microelectrodes (usually less than 10 volts), high electric fields can appear. Even with ac signals, Faradaic currents are probably occurring and they could give rise to

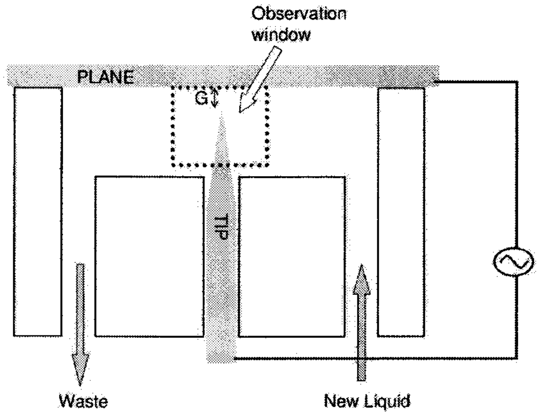

Figure B.1: Scheme of point-plane experimental device.

forces in the bulk of the fluid (García-Sánchez *et al.* (2008); Sides (2001)). Although electrolytes are quite different of dielectric liquids, the description of the fluid flow in microsystems might have some analogies with the EHD of insulating liquids (Castellanos (1998)).

In this work we study a model system: A metal tip in front of a planar electrode. This geometry was extensively used for low conductivity liquids (Atten *et al.* (1997)) and it has been commonly applied in the design of the injection (or ion-drag) pumps. The electric field is maximum at the tip apex, therefore electrochemical reactions are expected to happen there. In this way, we expect that fluid flow originated by these reactions is occurring near the tip. The plate is just working as the reference counter-electrode. It is worth noting the importance of the nature of the electrochemical reactions at the electrodes and their effect on the fluid flow. In dielectric liquids, the generation of ions at the metal tip leads to flows from the point to the plate, i.e. the typical charge injection. If instead, ions are discharged at the tip, the fluid flows from the plate to the metal point (Atten & Seyed-Yagoobi (2003)). For electrolytes, we argue that electrochemical reactions at the metal tip that generate ionic species (increasing the conductivity) lead to flows in the opposite direction to those reactions that consume ions (decreasing the conductivity)

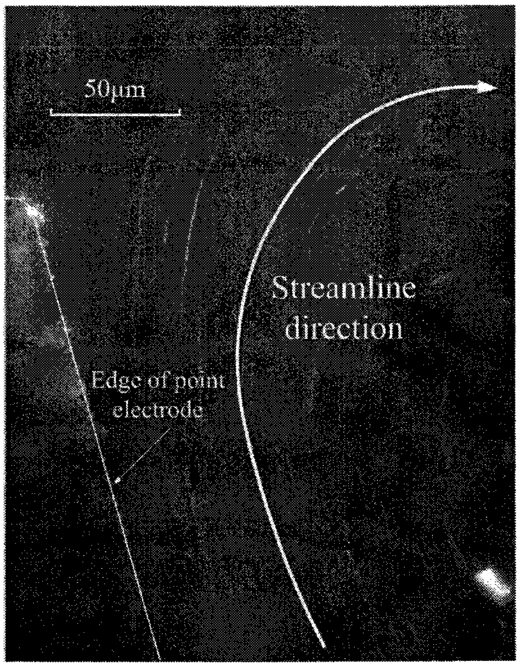

Figure B.2: Flow tracers path for an AC signal with 10 V_{pp} and 100 Hz. Electrolyte A.

(García-Sánchez *et al.* (2008)). The fabrication of this device does not require high technology. The only difficulty is found in the production of sharp metal tips. Here, we make use of a tungsten tip placed in front of a platinum plate.

When the point-plane system was subjected to ac signals, fluid flow was observed. The gap between the tip and the plane was around 100 μm. Voltage amplitudes larger than 5 V_{pp} were necessary in order to have an appreciable motion.

Electrolytes with three different conductivities were employed. Fluid flow occurred over a wide range of frequencies for all conductivities - from 100 Hz up to a frequency well above the charge relaxation frequency of each liquid. This result shows that a single mechanism based on perfectly polarisable electrodes -as occurs in electrokinetic phenomena- can not explain the flow generation. The observation of fluid flow around the relaxation frequency indicates that forces in the bulk should be present. Electrochemical reactions at the tip were probably generating changes in the liquid properties. In the results section, we discuss how gradients in liquid conductivity can give rise to induced charges in the bulk of the liquid.

B.2 Experimental Details

Fig. B.1 shows a scheme of the experimental device. A sharp tip is obtained from a tungsten bar (1 mm dia.) by electrochemical etching. The radius of the tip apex is around 5-10 μm. A glass chamber is fabricated with a platinum plate on one side. The tungsten tip is attached to a micrometer and placed in front of the plate. The gap (G) between the tip and the plane can be then adjusted.

The glass chamber has inlet and outlet ports. PTFE tubes with microfluidic valves are connected to these ports. The electrolyte is injected into the chamber through the tubes by means of a syringe. KCl aqueous solutions are used as working fluids. Three different salt concentrations are studied. The corresponding conductivities are: electrolyte A 1.5 mS/m, electrolyte B 7.7 mS/m and electrolyte C 15 mS/m. Fluorescent latex beads (500 nm diameter) are suspended in the electrolyte and used as flow tracers. A signal generator is used to apply ac potentials between the tip and the plane. Flow tracers within the “observation region” are viewed with an epifluorescence microscope (Nikon Optiphot-100). A digital camera attached to the microscope is used to capture videos of the observations.

B.3 Results and Discussion

Fig. B.2 shows the streamlines of the generated flow with electrolyte A for an applied signal of 10 V_{pp} and 100 kHz. This figure is the result of superimposing 80 consecutive frames of a video recording. The distance between the tip and the plane (G) is set to 100 μm. The flow direction is from the tip to the plane. The observed flows were always in this direction when working with electrolytes B and C. In some experiments with electrolyte A (1.5 mS/m) the direction of the flow was from the plane to the tip but this observation was not reproducible. Moreover, in some observations with electrolyte A, the flow changed from one direction to the other i.e. the fluorescent beads started to move from the plane to the tip and, after tens of seconds, the motion was reversed. This transient behavior was only observed in this sense.

Fluid velocities were measured at the middle position between the tip and the plane for the three different conductivities. Fig. (B.3) shows the measured fluid velocity versus frequency for a constant signal amplitude of 6 V_{pp}. These measurements, as well as the flow direction for electrolyte A, were hardly reproducible. However, an interesting feature of the experimental observations was always reproduced: the fluid velocity

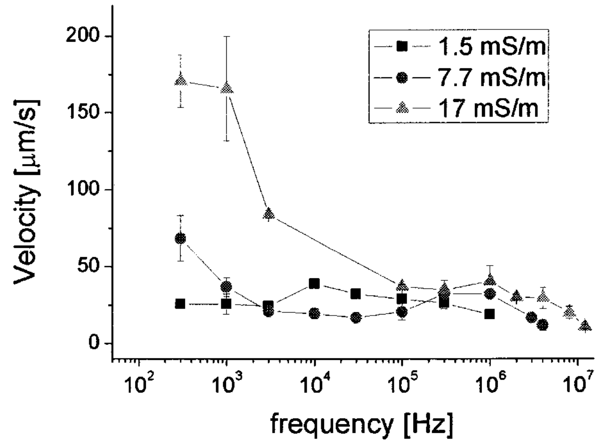

Figure B.3: Velocity vs frequency for a voltage amplitude of 6 V_{pp}.

vanishes above the charge relaxation frequency of the liquid. In table I are shown for each conductivity the frequencies at which the flow is not noticeable - velocities smaller than 5 μm/s. The corresponding relaxation frequencies are also shown.

Electrolyte	A	B	C
Conductivity	1.5 mS/m	7.7 mS/m	17 mS/m
Relaxation frequency	339 kHz	1.74 MHz	3.84 MHz
Maximum frequency	1.8 MHz	6.5 MHz	16 MHz

Table B.1: Relaxation frequencies and maximum frequencies at which fluid flow was observed for each of the three electrolytes

The theoretical typical frequencies for electroosmotic flow in this geometry (typical distance is $G = 100\,\mu$m) are around 100 Hz for electrolyte A and 340 Hz for electrolyte C. The presence of an oxide layer on the electrodes increases the typical frequency (González *et al.* (2000)), this could mean that frequencies for electroosmosis could be then around 1 kHz for electrolyte C. The observed fluid motion in these experiments occurred over a broad frequency range. The electrokinetic theory can not explain the fluid flow at 1 MHz.

Thermal effects or electrochemical processes can give rise to gradients in the electrolyte conductivity. EHD instabilities in microsystems due to these gradients have been recently studied (Baygents & Baldessari (1998); Chen *et al.* (2005)). Other instabilities such as those studied by Rubinstein and co-workers (Rubinstein & Zaltzman (2000)) may appear at high current densities. They are associated to depletion of electrolyte near the interfaces.

Beyond EHD instabilities, gradients in conductivity can give rise to fluid motion in, at least, the following situations:

(a) Gradients in temperature can generate fluid flow by the so called electrothermal effect (Green *et al.* (2001)). Computations show that, for the present conductivities and applied voltages, the effect should be negligible - velocities no higher than a few microns per second.

(b) Induced electrical charge can appear because of electrochemical processes at the electrodes. From the continuity equation for the electrical current and the assumption of quasielectroneutrality, the induced charge in the bulk is (Newman & Thomas-Alyea (2004)):

$$\frac{\rho}{\varepsilon} = \frac{\nabla\sigma \cdot \nabla\phi}{\sigma} + \frac{\sum_i z_i e D_i \nabla^2 c_i}{\sigma} \tag{B.1}$$

where σ is the liquid conductivity, ϕ the electric potential, e the proton charge and z_i, D_i and c_i are the ionic valence, diffusion coefficient and concentration of specie i, respectively. The first term in equation B.1 could give rise to a non-zero time-averaged force if the time-averaged conductivity gradient is non-zero $\langle \nabla\phi \neq 0 \rangle$. On the other hand, if has a time-varying component with the same frequency of the electric field, the second term in B.1 could also give rise to a non-zero time averaged force. This term can produced a net free charge in a layer of thickness $\sqrt{D/\omega}$, with ω the angular frequency of the applied field. For typical values of $\omega = 10^3\,\mathrm{rad/s}$ and $D = 10^{-9}\,\mathrm{m^2/s}$, this distance is of the order of microns $\delta \sim 1\,\mu\mathrm{m}$. The force due to this term has been considered by Sides (2001) and Fagan *et al.* (2004) for particle motion on top of AC polarized electrodes. This second term in B.1 is zero for a binary symmetrical electrolyte. Because of the relation of diffusion layer thickness with frequency, we expect that this term is negligible for frequencies beyond 100 kHz. Therefore, we suggest that the fluid flow observations are originated by the Coulomb force on the charge induced by electric fields on gradients of conductivity. These gradients of conductivity would be created by electrochemical reactions. Generation or consumption of ionic species at the metal point can lead to gradients of different sign and, consequently, the induced charge sign will depend on this as well as the fluid flow direction.

B.4 Conclusions

The present point-plane system is useful for studying EHD of electrolytes at the microscale. Different flow regimes were observed. The electrokinetic theory can not account for the fluid flow observations. Several mechanisms are proposed and, probably, a competition between them is generating the net flow observations.

Future work should be focused in an extension of the experiments to electrodes of different materials as well as to other electrode geometries. The measurement of the electrical current could provide some information about the physical origin of the fluid flow.

Appendix C

Particle tracking in Matlab

C.1 Introduction

The experiments with microelectrodes carried out during this thesis have usually required the use of fluorescent particles. Fluorescent latex beads of 500 nm diameter were used both for determining the fluid flow patterns and for measuring the fluid velocity. Several techniques can be found in the literature (Adrian (1991)) for performing particle-based flow visualisation. PIV (Particle Image Velocimetry) and PTV (Particle Tracking Velocimetry) are the most used methods for flow visualisation in micrometric systems, recent reviews can be found in Sinton (2004) and Adrian (2005). Any of these techniques relies upon the suspended beads behave as flow tracers, i.e. they follow the fluid flow and the velocity of the fluid at a certain time and position can be obtained from the motion of the particles.

The velocity measurements reported in this work were performed by means of the program PTS (Particle Tracking Software)[1]. This is a Matlab program for tracking the fluorescent particles in the video recordings of the experiments. Short frame sequences (between $\sim$ 50 and 100 frames) are exported from the video files and imported in Matlab. The fluorescent beads are found and labelled in every frame. Subsequently, trajectories are built by identifying a given particle in several consecutive frames. The next section provides the details of the tracking procedure implemented. An example of velocity measurement is also included.

C.2 Tracking Procedure

For realizing the velocity measurements, the PTS program requires a *Tiff image sequence* of the frames to be analysed. Typically, we start with a sequence of images in grayscale of 720×576 pixels, where regions of light gray pixels correspond to the images of the beads on a dark background[2]. The aim is to select a certain zone of the frames and convert it into black and white images. In this way, regions of white pixels can be identified as the images of the beads on a black background.

Once the region is selected, it is desirable to remove some objects

---

[1] This software is available upon request to pablogarcia@us.es

[2] In some experiments, white light was used instead of FITC illumination. In this case the 500 nm beads appear as black dots in a light gray background. These images are inverted in order to have light gray particles and, in this way, proceed as in the usual case.

that may appear in every frame. For example, when the electrodes are focused some beads may be stuck on them and appear during the entire sequence. In order to remove these objects, the average intensity of all frames is subtracted from every single frame and, in this way, only "moving beads" remain. Before the conversion to B&W, the intensity contrast is adjusted in every frame so the difference between light and dark pixels is enhanced. A threshold intensity value is chosen and all pixels below that value are switched to zero (black), pixels above the threshold are switched to one (white).

After the conversion to B&W, it is convenient to remove some isolated white pixels that might appear and have no correspondence to any particle. The next step is finding the particles in every frame. The program searches for isles of white pixels, every isle is considered a particle and labelled. The coordinates of the centre point of the particle are found and stored. At this point, we can start to search for the trajectories:

The distances between all particles in the first frame and all particles in the second frame are computed. The minimum of these distances is found. The two particles separated this distance are chosen and the particle in the second frame receives the same label that the corresponding particle in the first. This label assignation is carried out as far as this distance is less than a cutoff value introduced by the user. Fig. C.1 shows

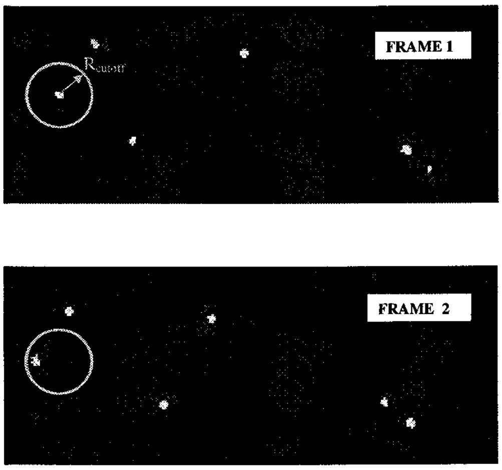

Figure C.1: Cutoff radius for finding trajectories.

an example, a circle of radius equal to the cutoff value R_{cutoff} is centered at the position of one particle in frame 1. The nearest particle of frame 2 to the particle of frame 1 is inside the circle. The criterion is then fulfilled and the label of the particle in frame 1 is assigned to the particle in frame 2. In this way we start to build the first of the trajectories.

The two particles involved in this trajectory are eliminated and, consequently, not taken into account for finding the next one. The minimum distance between all remaining particles is now found and, again, the particle in the second frame receives the same label that the corresponding particle in the first as far as this distance is less than the cutoff value. The second of the trajectories is now started and we keep this procedure until the remaining distances are larger than the cutoff value or all distances between the two first frames have been assigned to a trajectory. Note that the number of trajectories does not necessary match the number of beads in any of the two frames. Some labels might be lost in the first frame and the corresponding particles are not further accounted.

Once it is finished with the two first frames, we follow with the second and third frames. Some beads in the second frame will have the same label that beads in the first (trajectories started in the previous step), the others beads are candidate for starting new trajectories. The same matching procedure is now repeated, some trajectories will include a new point, others might be lost and new trajectories might also be created. In this way we can scan all frames and build several trajectories.

The particle velocity of every trajectory is computed from the final and initial position and the number of frames between them. The average value of the velocity in all trajectories is computed as:

$$\overline{v} = \frac{\sum_i n_i v_i}{\sum_i n_i} \tag{C.1}$$

where v_i is the velocity corresponding to trajectory i and n_i is the number of points of that trajectory. In this way, we make that trajectories with a larger number of points have more weight in the statistics. The error of the measurement is estimated as the standard deviation of the velocities distribution:

$$\Delta v = \sqrt{\frac{\sum_i n_i (v_i - \overline{v})^2}{\sum_i n_i}} \tag{C.2}$$

The velocity and error values are expressed in pixels/frame units. They are transformed to physical dimensions with the following parameters: frames per second (fps) at which the video was recorded and the micron to pixel ratio. The correspondence of pixels to microns can be calibrated by the user after opening the image sequence. It is needed a reference (known distance) in the images. The capture rate is usually 25 fps, but this can be changed by the user if required.

C.3 An Example of velocity measurement

This section includes an example of how to use the PTS program for measuring the velocity in one of the videos of the experiments. Fig. C.2 shows the *graphical user interface* that appears when the program is started (the program is started from the Matlab command window).

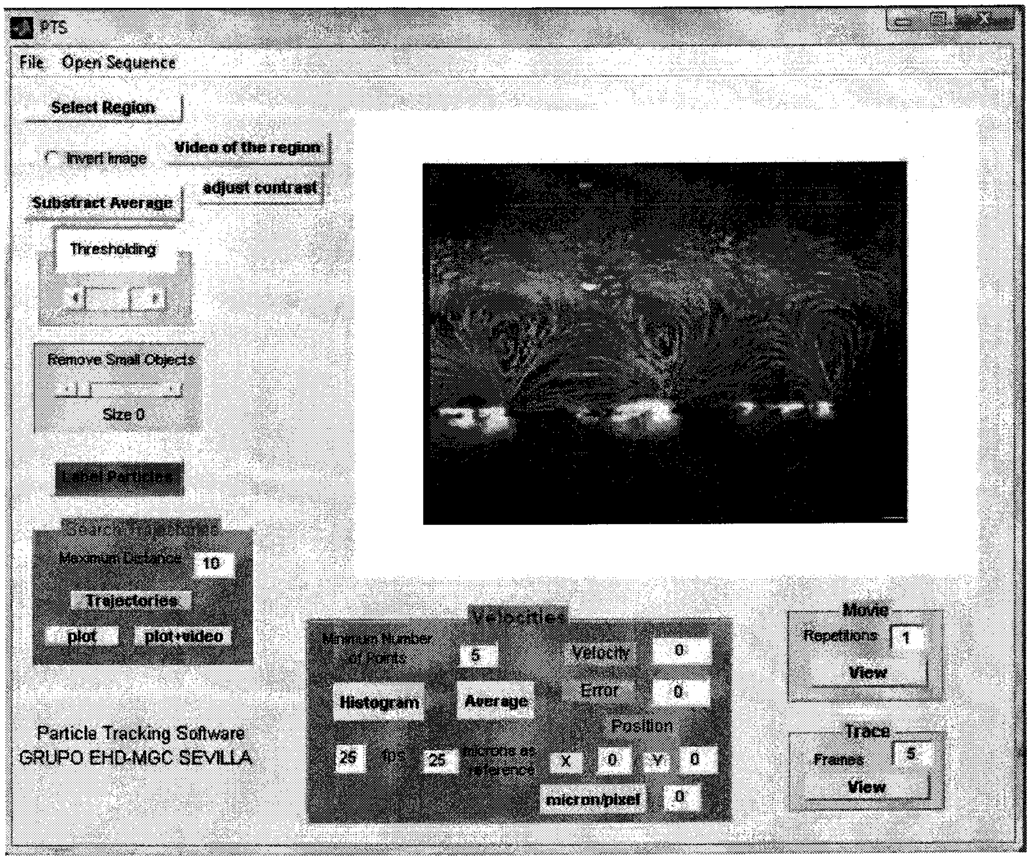

○ Invert image

Size 0

Maximum Distance 10

Minimum Number of Points 5

Velocity 0

Error 0

25 fps

25 microns as reference

X 0 Y 0

micron/pixel 0

Repetitions 1

Frames 5

Figure C.2: Graphical user interface of PTS

A tiff image sequence can be opened from the toolbar command "*Open Sequence*". Double click on the file name opens the frames corresponding to the selection of "*First frame to open*", "*Number of frames*" and "*Step*", see Fig. C.3. It is possible that we have long sequences but we only want to analyse a part of them or, for instance, we want to use different parts of the same sequence for different measurements. The "*First frame to open*" field selects at which frame of the entire sequence the import is starting. If the "*Step*" field is set to 1, all frames after the first are open until the "*Number of frames*" is reached. It is possible to skip frames during the opening if "*Step*" is set to a different value.

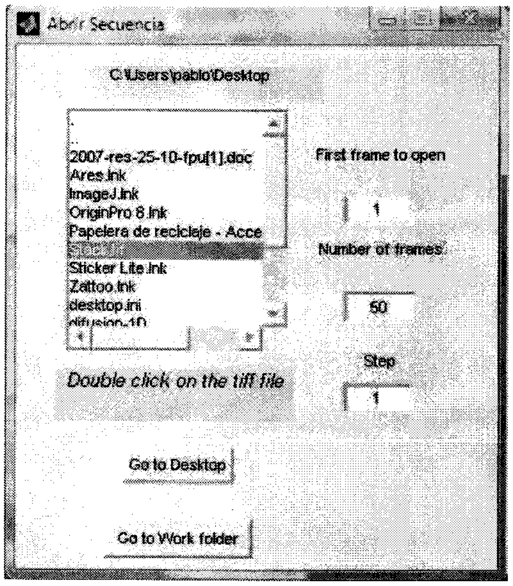

First frame to open: 1

Number of frames: 50

Step: 1

Figure C.3: Import a tiff sequence

The first frame of the selection is shown in the graph area of the PTS program window. The region of interest (ROI) can then be chosen clicking on "*Select Region*". A video of the ROI is shown if "*Video of the region*" is clicked.

The next task is the processing of the images. With the command "*Subtract Average*", the average intensity of all frames is subtracted from every single frame. In this way, objects that appear in every frame are removed. The images are now ready to be converted to B&W, it is although convenient to enhance the contrast before. The "*adjust contrast*" button is for performing this enhancement.

The conversion to B&W is carried out after selecting a threshold value [0,1] with the slide bar. A suitable value for the recordings of our experiments is 0.9. Since images are in a 256 grayscale, this means that all pixels above 230 are converted to white and all below will be black. Small objects should now be removed. The minimum radius accepted is selected with another slide bar. If the minimum radius is for example 2, all objects (white areas) whose typical distance is less than 4 pixels are removed (converted to black pixels).

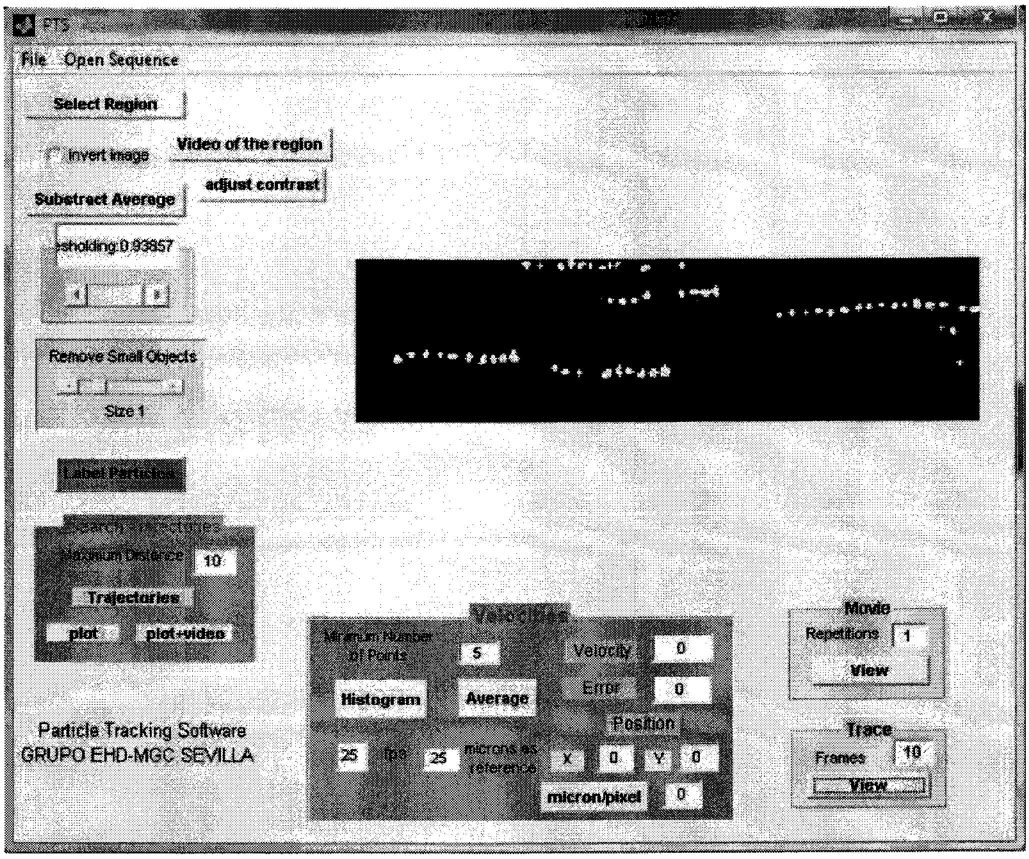

esholding:0.93857

Size 1

Maximum Distance 10

Minimum Number of Points 5

Velocity 0

Error 0

25 fps

25 microns as reference

X 0 Y 0

micron/pixel 0

Repetitions 1

Frames 10

Figure C.4: The graph shows the traces of the beads after 10 frames

At this point, we can see a video of the result of the image processing by clicking in the "*View*" button of the "*Movie*" area. In the "*Repetitions*" edit field, the user can introduce how many times the video is going to be shown. It can also be seen the result of superimposing a given number of frames. This is done in the "*Trace*" area where the total number of frames to be superimposed can be selected. Fig. C.4 shows the result of superimposing 10 frames of a video corresponding to an experiment with a travelling-wave array of titanium.

Clicking on "*Label particles*" the PTS program finds single connected areas of white pixels and assigns a label to every area. Trajectories can now be searched. The user must introduce a cutoff value in the "*Maximum Distance*" edit field and when the "*Trajectories*" button is clicked, the trajectories are built. If the "*plot*" button is used, the program plots the trajectories on the images of the ROI. If the "*plot+video*" button is clicked, the trajectories are plotted and a video of the ROI is shown simultaneously. In this way, the user can visually check how good the trajectories found by the program match the trajectories that one could predict by eye.

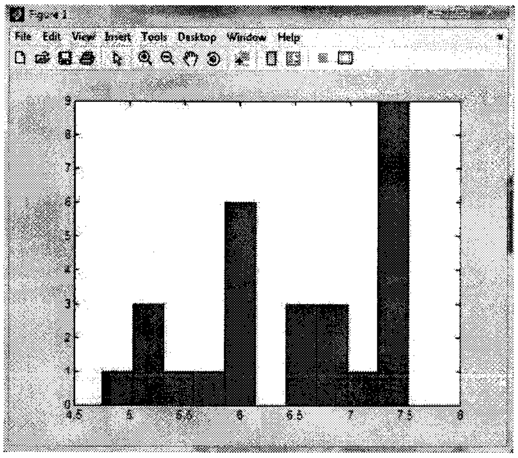

Figure C.5: The histogram shows the number of trajectories with a certain velocity

Once the trajectories are found, we can measure the average velocity within the ROI. Clicking on the "*Histogram*" button of the "*Velocities*" area shows a histogram like that in fig. C.5. The horizontal axis corresponds to the length in pixels of a trajectory over the number of frames in which was found, that is, velocity in pixels over frames units. The vertical axis corresponds to the number of trajectories found with that length. Only the trajectories with a total number of points equal or larger than the value introduced in the "*Minimum Number of Points*" edit field are considered. In this way, we neglect short trajectories that could not be significant.

We would finally like to have the average value and an estimate of the error of these measurements but expressed in physical units. Therefore, we must introduce the frame rate at which the image sequence was captured (25 fps by default). Note that if you are not importing all frames but skipping some, the PTS program is already accounting for this. The value to be to introduced in the *fps* field is that corresponding to the original sequence independently of how you use the frames to measure velocities. We also have to introduce the pixels to microns conversion factor. We need some reference in the images for this, i.e. a known distance. If we know, for instance, that the size of the electrodes and gaps in a TW device is 20 micron, we can introduce the number 100 in "*microns as reference*" edit field and then click in the "*micron/pixel*" button. A new window is open where the first frame of the original sequence is shown, see fig. C.6. Clicking on "*Select Width*" allows us to draw a rectangle whose width corresponds to the distance indicated in the microns as reference (in this case, 100 micron is equal to five times the electrode width). This is usually easy to do since one can identify the position of the electrodes in the video recordings and, then, draw the rectangle on them. The lower right corner of the rectangle is used as the origin for the coordinate system, that is, the position of the ROI is referenced to that point of the square we are using for calibrating distances. This reference is usually convenient as in the current example of the TW video since the Y-coordinate of the ROI corresponds to the height over the electrode array where the measurement is performed. After clicking on "*finish*" the window is close and the calibration step finished. The edit field near the "*micron/pixels*" button is updated to the conversion factor. By clicking

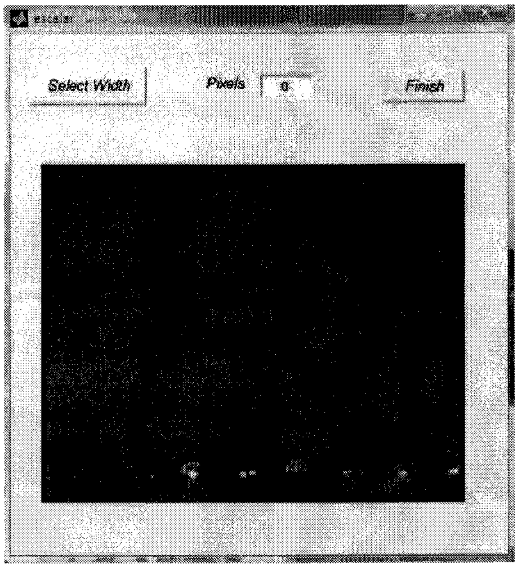

Pixels 0

Figure C.6: Window for calibrating distances on the "*Average*" button the average value and standard deviation of the histogram in fig. C.5 is calculated and then transformed to physical units. The result is shown in the "*Velocity*" and "*Error*" edit fields.

Appendix D

List of Publications during the PhD studies

Publications related to the thesis:

P. García-Sánchez, A. Ramos, A. González, N.G. Green, H. Morgan. **Flow reversal in traveling-wave electrokinetics: an analysis of forces due to ionic concentration gradients**. (submitted to Langmuir).

The results in this article have been included in chapters 4 and 6.

H. Yang, H. Jiang, D. Shang, A. Ramos, P. García-Sánchez. **Experiments on Traveling-Wave Electroosmosis: Effect of Electrolyte Conductivity**. (submitted to IEEE Transactions on Dielectrics and Electrical Insulation).

The results in this article have been included in chapter 4.

P. García-Sánchez, A. Ramos, N.G. Green, H. Morgan. **Traveling-wave electrokinetic micropumps: velocity, electrical current and impedance measurements**. *Langmuir* **2008**, 24, 9361-9369.

The results in this article have been included in chapter 4.

A. Ramos, A. González, P. García-Sánchez, A. Castellanos. **A linear analysis of the effect of Faradaic currents on traveling-wave electroosmosis.** *Journal of Colloid and Interface Science* **2007**, 309, 323-331.

The results in this article have been included in chapter 5.

H. Morgan, A. Ramos, N.G. Green, P. García-Sánchez. **Control of two-phase flow in a microfluidic system using ac electric fields.** *Applied Physics Letters* **2007**, 91, 254107.

This article has been included as Appendix A.

P. García-Sánchez, A. Ramos. **The effect of electrode height on the performance of travelling-wave electroosmotic micropumps.** *Microfluidics-Nanofluidics* **2008**, 5, 307-312.

The results in this article have been included in chapter 7.

P. García-Sánchez, A. Ramos, N.G. Green, H. Morgan. **Experiments on AC Electrokinetic Pumping of Liquids Using Arrays of Microelectrodes**. *IEEE Transactions on Dielectrics and Electrical Insulation* **2006**, 13, 670-677.

The results in this article have been included in chapter 3.

Other publications:

A. Ramos, P. García-Sánchez, A. Robles, M. J. Freire. **Pumping of water by microwave electric fields in microsystems.** (submitted to Journal of Electrostatics).

Y. Ren, H. Jiang, H. Yang, A. Ramos, P. García-Sánchez. **Electrical manipulation of electrolytes with conductivity gradients in microsystems.** (submitted to Journal of Electrostatics).

H. Yang, H. Jiang, A. Ramos, P. García-Sánchez. **AC and Travelling-Wave Electrokinetic Pumping on Symmetric Electrode Arrays.** (submitted to Microfluidics-Nanofluidics).

F. Carrique , P. García-Sánchez, E. Ruiz-Reina. **Electroviscous effect of moderately concentrated colloidal suspensions: Stern-layer influence.** *Journal of Physical Chemistry B* **2005**, 109(51), 24369.

E. Ruiz-Reina, P. García-Sánchez, F. Carrique. **Electroviscous effect of moderately concentrated colloidal suspensions under overlapping conditions.** *Journal of Physical Chemistry B* **2005**, 109(11), 5289.

E. Ruiz-Reina, A. I. Gómez-Merino, F.J. Rubio-Hernández, P. García-Sánchez. **ζ-Potential and Stern-layer parameters of γ-alumina suspensions.** *Journal of Colloids and Interface Science* **2003**, 268, 400-407.

E. Ruiz-Reina, F. Carrique, F.J. Rubio-Hernández, A.I. Gómez-Merino, P. García-Sánchez. **Primary electroviscous effect in moderately concentrated colloidal suspensions 2003.** *Journal of Physical Chemistry B* **2003**, 107, 9528-9534.

F.J. Rubio-Hernández, A.I. Gómez-Merino, E. Ruiz-Reina, P. García-Sánchez. **An experimental test of Booth's primary electroviscous effect theory.** *Journal of Colloid and Interface Science* **2002**, 255, 208-213.

Bibliography

R. J. ADRIAN, 1991. Particle-imaging techniques for experimental fluid mechanics. *Annual Review of Fluid Mechanics*, **23**, 261–304.

R. J. ADRIAN, 2005. Twenty years of particle image velocimetry. *Experiments in Fluids*, **39**, 159–169.

A. AJDARI, 2000. Pumping liquids using asymmetric electrode arrays. *Physical Review E*, **61**, R45–R48.

P. ATTEN & J. SEYED-YAGOOBI, 2003. Electrohydrodynamically induced dielectric liquid flow through pure conduction in point/plane geometry. *IEEE Transactions on Dielectrics and Electrical Insulation*, **10**, 27–36.

P. ATTEN, B. MALRAISON & M. ZAHN, 1997. Electrohydrodynamic plumes in point-plane geometry. *IEEE Trans. Dielectr. Electr. Insul.*, **4**, 710–718.

A. BARD & L. FAULKNER, 2001. *Electrochemical Methods: Fundamentals and Applications.* Wiley, New York.

J. C. BAYGENTS & F. BALDESSARI, 1998. Electrohydrodynamic instability in a thin fluid layer with an electrical conductivity gradient. *Physics of Fluids*, **10**, 301–311.

M. Z. BAZANT & Y. BEN, 2006. Theoretical prediction of fast 3d ac electro-osmotic pumps. *Lab On A Chip*, **6**, 1455–1461.

M. Z. BAZANT, K. THORNTON & A. AJDARI, 2004. Diffuse-charge dynamics in electrochemical systems. *Physical Review E*, **70**, 021506.

M. Z. BAZANT, M. S. KILIC, B. D. STOREY & A. AJDARI, 2008. Nonlinear electrokinetics at large applied voltages. *arXiv:cond-mat/0703035.*

C. BENDER & S. ORSZAG, 1987. *Advanced Mathematical Methods for Scientists and Engineers.* McGraw-Hill, New York.

A. Bonnefont, F. Argoul & M. Bazant, 2001. Analysis of diffuse-layer effects on time-dependent interfacial kinetics. *Journal of Electroanalytical Chemistry*, **500**, 5261.

D. A. Boy & B. D. Storey, 2007. Electrohydrodynamic instabilities in microchannels with time periodic forcing. *Physical Review E*, **76**, 026304.

A. B. D. Brown, C. G. Smith & A. R. Rennie, 2000. Pumping of water with ac electric fields applied to asymmetric pairs of microelectrodes. *Physical Review E*, **63**, 016305.

B. P. Cahill, L. J. Heyderman, J. Gobrecht & A. Stemmer, 2004. Electro-osmotic streaming on application of traveling-wave electric fields. *Physical review E*, **70**, 036305.

A. Castellanos, 1998. *Electrohydrodynamics.* Springer, New York.

A. Castellanos, A. Ramos, A. González, N. G. Green & H. Morgan, 2003. Electrohydrodynamics and dielectrophoresis in microsystems: scaling laws. *Journal of Physics D: Applied Physics*, **36**, 2584–2597.

C. H. Chen, H. Lin, S. K. Lele & J. G. Santiago, 2005. Convective and absolute electrokinetic instability with conductivity gradients. *Journal of Fluid Mechanics*, **524**, 263–303.

C. T. Culbertson, S. C. Jacobson & J. M. Ramsey, 2002. Diffusion coefficient measurements in microfluidic devices. *Talanta*, **56**, 365.

S. Debesset, C. Hayden, C. Dalton, J. Eijkel & A. Manz, 2004. An ac electroosmotic micropump for circular chromatographic applications. *Lab on a Chip*, **4**, 396–400.

A. V. Delgado, F. Gonzalez-Caballero, R. Hunter, L. Koopal & J. Lyklema, 2005. Measurement and interpretation of electrokinetic phenomena (iupac technical report). *Pure and Applied Chemistry*, **77**, 1753–1802.

P. Dittrich, K. Tachikawa & A. Manz, 2006. Micro total analysis systems. latest advancements and trends. *Analytical Chemistry*, **2**, 3887–3908.

R. M. Ehrlich & J. R. Melcher, 1982. Bipolar model for travelling-wave induced nonequilibrium double-layer streaming in insulating liquids. *Physics of Fluids*, **25**, 1785–1793.

J. A. FAGAN, P. J. SIDES & D. C. PRIEVE, 2004. Vertical motion of a charged colloidal particle near an ac polarized electrode with a nonuniform potential distribution: Theory and experimental evidence. *Langmuir*, **20**, 4823–4834.

M. FELTEN, P. GEGGIER, M. JÄGER & C. DUSCHL, 2006. Controlling electrohydrodynamic pumping in microchannels through defined temperature fields. *Physics of Fluids*, **18**, 051707.

S. FIEDLER, R. HAGEDORN, T. SCHNELLE, E. RICHTER, B. WAGNER & G. FUHR, 1995. Diffusional electrotitration - generation of ph-gradients over arrays of ultramicroelectrodes detected by fluorescence. *Analytical Chemistry*, **67**, 820–828.

A. Y. FU, C. SPENCE, A. SCHERER, F. H. ARNOLD & S. R. QUAKE, 1999. A microfabricated fluorescence-activated cell sorter. *Nature Biotechnology*, **17**, 1109.

G. FUHR, R. HAGEDORN, T. MULLER, W. BENECKE & B. WAGNER, 1992a. Microfabricated electrohydrodynamic (ehd) pumps for liquids of higher conductivity. *J. Microelectro-mech. Systems*, **1**, 141–146.

G. FUHR, R. HAGEDORN, T. MÜLLER, W. BENECKE & B. WAGNER, 1992b. Microfabricated electrohydrodynamic (ehd) pumps for liquids of higher conductivity. *Journal of Electromechanical Systems*, **1**, 141–146.

P. GARCÍA-SÁNCHEZ, A. RAMOS, N. G. GREEN & H. MORGAN, 2006. Experiments on ac electrokinetic pumping of liquids using arrays of microelectrodes. *IEEE Trans. Dielectr. Electr. Insulat.*, **13**, 670–677.

P. GARCÍA-SÁNCHEZ, A. RAMOS, N. G. GREEN & H. MORGAN, 2008. Travelling-wave electrokinetic micropumps: velocity, electrical current and impedance measurements. *Langmuir*, **24**.

L. A. GEDDES, K. S. FOSTER, J. REILLY, W. D. VOORHEES, J. D. BOURLAND, T. RAGHEB & N. E. FEARNOT, 1984. The rectification properties of an electrode-electrolyte interface operated at high sinusoidal current density. *IEEE Transactions on Biomedical Engineering*, **9**, 669–672.

I. GLASGOW, J. BATTON & N. AUBURY, 2004. Electroosmotic mixing in microchannels. *Lab on a Chip*, **4**, 558.

A. GONZÁLEZ, A. RAMOS, N. GREEN, A. CASTELLANOS & H. MORGAN, 2000. Fluid flow induced by nonuniform ac electric fields in electrolytes on microelectrodes. ii. a linear double-layer analysis. *Physical Review E*, **61**, 4019–4028.

A. GONZÁLEZ, A. RAMOS, H. MORGAN, N. G. GREEN & A. CASTELLANOS, 2006. Electrothermal flows generated by alternating and rotating electric fields in microsystems. *Journal of Fluids Mechanics*, **564**, 415–433.

A. GONZÁLEZ, A. RAMOS & A. CASTELLANOS, 2008a. Pumping of electrolytes using travelling-wave electro-osmosis: a weakly nonlinear analysis. *Microfluidics Nanofluidics.*

A. GONZÁLEZ, A. RAMOS, P. GARCÍA-SÁNCHEZ & A. CASTELLANOS, 2008b. Effect of the difference in ion mobilities on traveling-wave electro-osmosis. *arXiv/0803.1055.*

N. GREEN, A. RAMOS, A. GONZÁLEZ, H. MORGAN & A. CASTELLANOS, 2000a. Fluid flow induced by non-uniform ac electric fields in electrolytes on microelectrodes i: Experimental measurements. *Phys. Rev. E*, **61**, 4011–4018.

N. G. GREEN, A. RAMOS, A. GONZÁLEZ, A. CASTELLANOS & H. MORGAN, 2000b. Electric field induced fluid flow on microelectrodes: the effect of illumination. *Journal of Physics D: Applied Physics*, **33**, L13–17.

N. G. GREEN, A. RAMOS & H. MORGAN, 2000c. Ac electrokinetics: a survey of sub-micrometre particle dynamics. *Journal of Physics D: Applied Physics*, **33**, 632–641.

N. G. GREEN, A. RAMOS, A. GONZÁLEZ, A. CASTELLANOS & H. MORGAN, 2001. Electrothermally induced fluid flow on microelectrodes. *Journal of Electrostatics*, **53**, 71–87.

N. G. GREEN, A. RAMOS, A. GONZÁLEZ, H. MORGAN & A. CASTELLANOS, 2002a. Fluid flow induced by nonuniform ac electric fields in electrolytes on microelectrodes. iii. observation of streamlines and numerical simulation. *Physical Review E*, **66**, 026305–2002.

N. G. GREEN, A. RAMOS & H. MORGAN, 2002b. Numerical solution of the dielectrophoretic and travelling wave forces for interdigitated electrode arrays using the finite element method. *Journal of Electrostatics*, **56**, 235–254.

M. M. Gregersen, L. H. Olesen, A. Brask, M. F. Hansen & H. Bruus, 2007. Flow reversal at low voltage and low frequency in a microfabricated ac electrokinetic pump. *Physical Review E*, **76**, 056305.

S. Hardt & F. Schönfeld, eds., 2008. *Microfluidics technologies for miniaturized analysis systems.* Springer.

Y. Huang, X. Wang, J. Tame & R. Pethig, 1993. Electrokinetic behaviour of colloidal particles in travelling electric fields. studies using yeast cells. *Journal of Physics D: Applied Physics*, **26**, 1528–1535.

R. Hunter, 1993. *Introduction to Modern Colloid Science.* Oxford University Press.

C. Jacobson & J. M. Ramsey, 1995. Microchip electrophoresis with sample stacking. *Electrophoresis*, **16**, 481–486.

C. Jacobson & J. M. Ramsey, 1997. Electrokinetic focusing on microfabricated channel structures. *Analytical Chemistry*, **69**, 3212.

J. Jang & S. Lee, 2000. Theoretical and experimental study of mhd (magnetohydrodynamic) micropumps. *Sensors and Actuators*, **80**, 84–89.

M. S. Kilic, M. Z. Bazant & A. Ajdari, 2007a. Steric effects in the dynamics of electrolytes at large applied voltages: I. double-layer charging. *Phys. Rev. E*, **75**, 021502.

M. S. Kilic, M. Z. Bazant & A. Ajdari, 2007b. Steric effects in the dynamics of electrolytes at large applied voltages: Ii. modified nernst-planck equations. *Phys. Rev. E*, **75**, 021503.

M. Koch, A. Evans & A. Brunnschewiler, 2000. *Microfluidic Technology and Applications.* Research Studies Ltd., Baldock, Herts, England.

D. J. Laser & J. G. Santiago, 2004. A review of micropumps. *J. Micromech. Microeng.*, **14**, R35–R64.

D. Lastochkin, R. Zhou, P. Wang, Y. Ben & H.-C. Chang, 2004. Electrokinetic micropump and micromixer design based on ac faradaic polarization. *Journal of Applied Physics*, **96**, 1730–1733.

F. C. Leinweber & U. Tallarek, 2004. Nonequilibrium electrokinetic effects in beds of ion-permselective particles. *Langmuir*, **20**, 11637–11648.

F. C. Leinweber & U. Tallarek, 2005. Concentration polarization-based nonlinear electrokinetics in porous media: Induced-charge electroosmosis. *Journal of Physical Chemistry B*, **109**, 21481–21485.

F. C. Leinweber, J. C. T. Eijkel, J. G. Bomer & A. van den Berg, 2006. Continuous flow microfluidic demixing of electrolytes by induced charge electrokinetics in structured electrode arrays. *Analytical Chemistry*, **78**, 1425–1434.

A. Lemoff & A. Lee, 2000. An ac magnetohydrodynamic micropump. *Sensors and Actuators B*, **63**, 178–185.

V. Levich, ed., 1962. *Physicochemical Hydrodynamics.* Prentice-Hall, Englewood Cliffs, N.J.

H. Lin, B. D. Storey, M. H. Oddy, C.-H. Chen & J. G. Santiago, 2004. Instability of electrokinetic microchannel flows with conductivity gradients. *Physics of Fluids*, **16**, 1922–1935.

N. Malouf, 2004. *An Introduction to Microelectromechanical Systems Engineering.* Artech House, Inc.

J. R. Melcher, 1966. Traveling-wave induced electroconvection. *Physics of Fluids*, **9**, 1548–1555.

J. R. Melcher & M. S. Firebaugh, 1967. Traveling-wave bulk electroconvection induced across a temperature gradient. *Physics of Fluids*, **10** (6), 1178–1185.

H. Morgan & N. G. Green, 2003. *AC Electrokinetics: colloids and nanoparticles.* Research Studies Press Ltd.

H. Morgan, A. G. Izquierdo, D. Bakewell, N. G. Green & A. Ramos, 2001. The dielectrophoretic and travelling wave forces generated by interdigitated electrode arrays: analytical solution using fourier series. *Journal of Physics D: Applied Physics*, **34**, 1533–1561.

H. Morgan, D. Holmes & N. G. Green, 2003. 3d focusing of nanoparticles in microfluidic channels. *IEE Proc.: Nanobiotechnol.*, **150**, 76.

M. Mpholo, C. G. Smith & A. B. D. Brown, 2003. Low voltage plug flow pumping using anisotropic electrode arrays. *Sensors and Actuators B*, **92**, 262–268.

J. S. Newman & K. E. Thomas-Alyea, 2004. *Electrochemical systems.* Wiley-IEEE.

N.-T. NGUYEN & Z. WU, 2005. Micromixers?a review. *Journal of Micromechanics and Microengineering*, **15**, R1–R16.

M. H. ODDY, J. G. SANTIAGO & J. C. MIKKELSEN, 2001. Electrokinetic instability micromixing. *Analytical Chemistry*, **73**, 5822–5832.

J. J. O'DEA, R. A. OSTERYOUNG & J. G. OSTERYOUNG, 1994. Radio frequency detectors based on microelectrodes. *Analytical Chemistry*, **66**, 798–801.

L. OLESEN, 2006. *AC electrokinetic micropumps*. Tesis Doctoral, Technical University of Denmark.

L. OLESEN, H. BRUUS & A. AJDARI, 2006. Ac electrokinetic micropumps: The effect of geometrical confinement, faradaic current injection, and nonlinear surface capacitance. *Physical Review E*, **73**, 056313.

H. A. POHL, 1978. *Dielectrophoresis*. Cambridge University Press.

V. PRETORIUS, B. HOPKINS & J. SCHIEKE, 1974. Electro-osmosis: A new concept for high-speed liquid chromatography. *Journal of Chromatography*, **99**, 23–30.

A. RAMOS, 2007. *Microfluidics technologies for miniaturized analysis systems*, cap. Electrohydrodynamics and Magnetohydrodynamics Micropumps. Springer.

A. RAMOS, H. MORGAN, N. GREEN & A. CASTELLANOS, 1998. Ac electrokinetics: a review of forces in microelectrode structures. *Journal of Physics D: Applied Physics*, **31**, 2338–2353.

A. RAMOS, H. MORGAN, N. GREEN & A. CASTELLANOS, 1999a. Ac electric-field-induced fluid flow in microelectrodes. *J. Colloid and Interface Science*, **217**, 420–422.

A. RAMOS, H. MORGAN, N. GREEN & A. CASTELLANOS, 1999b. The role of electrohydrodynamic forces in the dielectrophoretic manipulation and separation of particles. *Journal of Electrostatics*, **47**, 71–81.

A. RAMOS, A. GONZÁLEZ, A. CASTELLANOS, N. G. GREEN & H. MORGAN, 2003. Pumping of liquids with ac voltages applied to asymmetric pairs of microelectrodes. *Physical Review E*, **67**, 056302.

A. RAMOS, H. MORGAN, N. G. GREEN, A. GONZÁLEZ & A. CASTELLANOS, 2005. Pumping of liquids with traveling-wave electroosmosis. *J. of Applied Physics*, **97**, 084906.

A. Ramos, A. González, P. García-Sánchez & A. Castellanos, 2007. A linear analysis of the effect of faradaic currents on traveling-wave electroosmosis. *J. Colloid Interface Sci.*, **309**, 323–331.

A. Richter & H. Sandmaier, 1990. An electrohydrodynamic micropump. *An Investigation of Micro Structures, Sensors, Actuators, Machines and Robots, in Proceedings of Micro Electro Mechanical Systems, IEEE*, págs. 99–104.

I. Rubinstein & B. Zaltzman, 2000. Electro-osmotically induced convection at a permselective membrane. *Physical Review E*, **62**, 2238–2251.

I. Rubinstein & B. Zaltzman, 2001. Electroosmotic slip of the second kind and instability in concentration polarization at electrodialysis membranes. *Mathematical Models and Methods in Applied Sciences*, **11**, 263–300.

I. Rubinstein & B. Zaltzman, 2007. Electro-convective versus electroosmotic instability in concentration polarization. *Advances in Colloid and Interface Science*, **134-135**, 190–200.

N. Sasaki, T. Kitamori & H. B. Kim, 2006. Ac electroosmotic micromixer for chemical processing in a microchannel. *Lab on a Chip*, **6**, 550.

D. A. Saville, 1997. Electrohydrodynamics: The taylor-melcher leaky dielectric model. *Annual Review of Fluids Mechanics*, **29**, 27–64.

H. P. Schwan, 1992. Linear and nonlinear electrode polarization and biological materials. *Annals of Biomedical Engineering*, **20**, 269–288.

P. J. Sides, 2001. Electrohydrodynamic particle aggregation on an electrode driven by an alternating electric field normal to it. *Langmuir*, **17**, 5791–5800.

P. J. Sides, 2003. Calculation of electrohydrodynamic flow around a single particle on an electrode. *Langmuir*, **19**, 2745–2751.

D. Sinton, 2004. Microscale flow visualization. *Microfluidics Nanofluidics*, **1**, 2–21.

T. M. Squires & M. Z. Bazant, 2004. Induced-charge electro-osmosis. *Journal of Fluid Mechanics*, **509**, 217–252.

T. M. Squires & S. R. Quake, 2005. Microfluidics: Fluid physics at the nanoliter scale. *Review of Modern Physics*, **77**, 977–1026.

H. Stone, A. Stroock & A. Ajdari, 2004. Engineering flows in small devices: Microfluidics toward a lab-on-a-chip. *Annu. Rev. Fluid Mech.*, **36**, 381411.

J. A. Stratton, 1941. *Electromagnetic Theory.* McGraw-Hill.

V. Studer, A. Pépin, Y. Chen & A. Ajdari, 2004. Fast and tunable integrated ac electrokinetic pumping in a microfluidic loop. *The Analyst*, **29**, 944–949.

Y. K. Suh & S. Kang, 2008. Asymptotic analysis of ion transport in a nonlinear regime around polarized electrodes under ac. *Physical Review E*, **77**, 031504.

M. Trau, D. A. Saville & I. A. Aksay, 1997. Assembly of colloidal crystals at electrode interfaces. *Langmuir*, **13**, 6375–6381.

J. Urbanski, T. Thorsen, J. Levitan & M. Bazant, 2006. Fast ac electro-osmotic micropumps with nonplanar electrodes. *Appl. Phys. Lett.*, **89**, 143508.

J. P. Urbanski, J. A. Levitan, D. N. Burch, T. Thorsen & M. Z. Bazant, 2007. The effect of step height on the performance of three-dimensional ac electro-osmotic microfluidic pumps. *J. Colloid and Interface Science*, **309**, 332–341.

X. Wang, Y. Huang, F. Becker & P. Gascoyne, 1994. A unified theory of dielectrophoresis and traveling-wave dielectrophoresis. *Journal of Physics D: Applied Physics*, **27**, 1571–1574.

G. Whitesides, D. Janasek, J. Franzke & A. M. et al., 2006. Insight: Lab on a chip. *Nature*, **442**, 367–418.

J. Wu, 2006. Biased ac electro-osmosis for on-chip bioparticle processing. *IEEE Transactions on Nanotechnology*, **5**, 84–89.

S.-R. Yeh, M. Seul & B. I. Shraiman, 1997. Assembly of ordered colloidal aggregates by electric-field-induced fluid flow. *Nature*, **386**, 57–59.

H. Zhao & H. H. Bau, 2007. Microfluidic chaotic stirrer utilizing induced-charge electro-osmosis. *Phys. Rev. E*, **75**, 066217.

UNIVERSIDAD DE SEVILLA

Reunido el tribunal en el día de la fecha, integrado por los abajo firmantes, para evaluar la tesis doctoral
de D. PABLO GARCÍA SÁNCHEZ
tiulada FLUJOS DE ELECTROLITOS GENERADOS POR MICROELECTRODOS SOMETIDOS A UNA ONDA DE POTENCIAL VIAJERA
acordó otorgarle la calificación de SOBRESALIENTE CUM LAUDE

Sevilla, a 09 de ENERO de 2009

Vocal,

Vocal,

Vocal,

Presidente,

Secretario,

Doctorando,